

Andreas Spiegler

**Dynamics of biologically informed neural mass
models of the brain**

Dynamics of biologically informed neural mass models of the brain

Andreas Spiegler



Universitätsverlag Ilmenau
2012

Impressum

Bibliografische Information der Deutschen Nationalbibliothek

Die Deutsche Nationalbibliothek verzeichnet diese Publikation in der Deutschen Nationalbibliografie; detaillierte bibliografische Angaben sind im Internet über <http://dnb.d-nb.de> abrufbar.

Diese Arbeit hat der Fakultät für Informatik und Automatisierung der Technischen Universität Ilmenau als Dissertation vorgelegen.

Tag der Einreichung: 21. April 2011

1. Gutachter: Univ.-Prof. Dr.-Ing. habil. Jens Haueisen
(Technische Universität Ilmenau)

2. Gutachter: Dr.-Ing. habil. Thomas R. Knösche
(Max-Planck-Institut für Kognitions- und Neurowissenschaften,
Leipzig)

3. Gutachter: Dr. rer. nat. Viktor Jirsa
(Aix-Marseille Université, Marseille)

Tag der Verteidigung: 06. Juni 2011

Technische Universität Ilmenau/Universitätsbibliothek

Universitätsverlag Ilmenau

Postfach 10 05 65

98684 Ilmenau

www.tu-ilmenau.de/universitaetsverlag

Herstellung und Auslieferung

Verlagshaus Monsenstein und Vannerdat OHG

Am Hawerkamp 31

48155 Münster

www.mv-verlag.de

ISBN 978-3-86360-024-2 (Druckausgabe)

URN [urn:nbn:de:gbv:ilm1-2011000503](http://nbn-resolving.org/urn:nbn:de:gbv:ilm1-2011000503)

Titelfoto: photocase.com

To my grandmother Justine

Preface

The research conducted at the Max Planck Institute for Human Cognitive and Brain Sciences, Leipzig in the Research Group Cortical Networks and Cognitive Functions and at the Institute of Biomedical Engineering and Informatics, Ilmenau University of Technology, Ilmenau, under the supervision of Professor Jens Haueisen and Dr. Thomas R. Knösche. This work refers to two subjects: the analysis of the model and the application to experimental data. The first subject was examined in collaboration with Dr. Fatihcan M. Atay (Max Planck Institute for Mathematics in the Sciences, Leipzig) and Dr. Stefan J. Kiebel (Max Planck Institute for Human Cognitive and Brain Sciences, Leipzig). The second subject was studied in collaboration with Dr. Fatihcan M. Atay and Dr. Karin Schwab (Bernstein Group for Computational Neuroscience Jena, Institute of Medical Statistics, Computer Sciences and Documentation, Jena University Hospital, Friedrich Schiller University, Jena).

I would like to express my gratitude to everyone who has contributed to making this research possible. First of all my mentors: Dr. Thomas R. Knösche, my main supervisor, for his supervision, advice, and guidance from the very early stage of this research as well as for giving me outstanding experience throughout. Above all and the most needed, he provided me with support of various kinds and, above all and most needed with unflinching encouragement; Professor Jens Haueisen for his detailed and constructive comments, and for his vital support. His

intuition, that of a true scientist, has made him a constant oasis of ideas and passions in science, nurturing my growth as a student, a researcher and a would-be scientist. I am indebted to him more than he knows, and especially for leading me to teach, so that I could discuss my work in students' courses and at several symposia.

I wish to express my warm and sincere thanks to Dr. Fatihcan M. Atay who gave backbone to the research and so to this work with his mathematical advice. Our discussions clear my thinking and hold me to high standards. Fatihcan, I am grateful in every possible way and hope to keep up our collaboration in the future. Special thanks go to Dr. Stefan J. Kiebel for his ideas and advice, which have had a marked influence on my research. I am grateful to him for encouraging me at every points requiring analysis to think about the conceptual frameworks behind computational modeling. His involvement and his originality have nourished the growth of my intellect and will continue to do so until I can claim intellectual maturity. In the realm of the experiments, I wish to thank Dr. Karin Schwab for her collaboration and her analyses. To Henning Schwanbeck go my thanks for his kind and timely computational support.

I am obliged to many of my colleagues who supported me at the Max Planck Institute: with moral support (Maren Grigutsch), and computer technology (Dr. Alfred Anwander); with Bayesian inference schemes (Peng Wang). On the neural field model front I had great help from Christopher Koch and Manh Nguyen Trong. Manh, I will always remember our hiking trip through the American desert.

Many friends have helped me stay sane through these years. Their support and care helped me overcome setbacks and stay focused on my graduate study. I greatly value their friendship and I deeply appreciate their belief in me. A special thank-you goes to Henriette, Jenny and Jan, such a support in the last half year of writing.

Most of all, gratitude goes to my family for their unflagging love and support throughout my life; this research would simply have been

impossible without them. Thank you for having absolute confidence in me.

Finally, thank you for the money: Ilmenau University of Technology paid me while I prepared a successful grant application, and the Max Planck Society and Deutsche Forschungsgemeinschaft funded parts of the research discussed in this work.

A.S., Marseille, March 27, 2012

Contents

Preface	7
1 Introduction	15
2 Neuronal Modeling	25
2.1 Computational Neuroscience	26
2.1.1 Extending the Scientific Method	26
2.1.2 Complexity of Models	27
2.1.3 Classification of Models	27
2.1.4 Classification of the Zetterberg-Jansen Model . .	28
2.2 Forward Model	29
2.3 Neuronal States	30
2.3.1 Neurons – The Dynamic Computational Units .	31
2.3.2 Ensembles – The Unit of Brain Functions	32
2.4 Mean-Field Approximation	33
2.4.1 Ensemble Density Models	33
2.4.2 Neural Mass Models	35
3 Mathematics and Methods	43
3.1 Mean-Field Framework	43
3.1.1 Definition	44
3.1.2 Activity-Based and Voltage-Based Models	48
3.1.3 Model Equivalence	52

3.1.4	Normalization	56
3.2	Point-Like Voltage-Based Model	56
3.2.1	Potential-to-Rate Transfer Function	57
3.2.2	Temporal Differential Operator	59
3.2.3	Linear System of a Lumped Neural Mass	61
3.2.4	Equivalence – Jansen’s Configuration	62
3.3	Methods	63
3.3.1	Bifurcation Diagrams	64
3.3.2	Time Series	65
3.3.3	Characteristic Lyapunov Spectra	66
3.3.4	Kaplan-Yorke Dimension	68
3.3.5	Poincaré Map	68
3.4	Experimental Data	69
4	Zetterberg-Jansen Model	71
4.1	System	74
4.2	Extrinsic Input	76
5	Modes of a Cortical Area	79
5.1	Constantly Forced Model	79
5.1.1	Parameter Space	81
5.1.2	System Analysis Using Bifurcation Theory	84
5.1.3	Results	93
5.2	Periodically Forced Model	111
5.2.1	Parameter Space	112
5.2.2	Stimulus Dependent State Space Analysis	117
5.2.3	Results	120
6	Resonance Phenomena	123
6.1	Experimental Data	124
6.2	Periodically Forced Model	126
6.3	Comparison	126
6.4	Results	127

7	Discussion and Conclusion	129
7.1	Zetterberg-Jansen Model	130
7.2	Constantly Forced Model	131
7.2.1	States and the Underlying Mechanisms	131
7.2.2	Classification of LC-Branches	132
7.2.3	Ordered Sequences	134
7.2.4	Transitions Between Regimes	136
7.2.5	Modeling	136
7.2.6	Links to Neuroscience	137
7.3	Periodically Forced Model	139
7.3.1	Complex Behavior	139
7.3.2	Chaos in the Brain?	140
7.3.3	Ordered Sequences	141
7.4	Brain Resonance Phenomena	142
7.4.1	Periodically Forced Oscillator	142
7.4.2	Comparison	143
7.4.3	Predictions	143
7.5	Future Directions	144
7.6	Conclusion	146
A	Appendix	149
A.1	Characteristics of the Sigmoid	149
A.2	Temporal Differential Operator	151
A.3	Effective Extrinsic Input on all Masses	154
A.4	Modes of a Single Neural Mass	156
A.5	Characteristic Mean Frequency	159
A.6	Symbols and Abbreviations	161

1 Introduction

*Objectivity is a subject's delusion
that observing can be done without him.*

Heinz von Foerster, 1911–2002

Neuroscience aims to understand the enormously complex functioning of the normal and diseased brain. This in turn is the key to explaining human behavior and to developing novel diagnostic and therapeutic procedures. In the present work, models of mean activity in a single brain area have been developed and used which provide a balance between tractability and biophysical plausibility.

Single neurons, at the microscopic level, are considered the primary computational units of the brain's architecture [1,2]. However, it is also widely accepted that ensembles of interacting neurons at the mesoscopic level can carry out the relevant information processing underlying brain functions such as action, perception, and cognition in both healthy and diseased states [3–11]. Measurements such as *magnetoencephalography* and *electroencephalography* (M/EEG) provide a satisfactory spatial scale for the achievement of insight into the implementation of brain functions as far as they are reflected by the spatiotemporal evolution of *neural ensembles* [12–14]. There are other (noninvasive) measurements such as functional *magnetic resonance imaging* (functional MRI) which access this mesoscopic level. Functional MRI records changes

in metabolism and blood flow indicating energy consumption. These changes are indirectly related to changes in the activity of neural ensembles, and provide much better spatial information than does M/EEG, though rather poor temporal information [15–22].

M/EEG supplies noninvasive electrophysiological measurements usually acquired under defined conditions (e.g., stimulation patterns and behavior, sleep stage, general vigilance, pathologies) [23–26]. Generally, such noninvasive approaches gather from a position on or near to the scalp the physical quantity of interest: that is, for EEG and MEG the electrical potential and magnetic field, at a distance from their generators (e.g., membrane potential and currents of neurons and neural ensembles).

Consequently, the recording captured by one sensor may have been caused by several intracranial generators simultaneously. This superposition effect is complicated even more by the complex geometry and the electromagnetic properties of the head tissues. The unmixing of M/EEG data in order to study the implementation of brain functions (on the basis of the underlying generator configurations) turns out to be an ill-posed inverse problem. This means that without any a-priori knowledge or assumptions it is impossible to reconstruct a unique intracranial generator configuration for given (M/EEG) data [25]. The problem can be split in two: (i) the forward problem that deals with the prediction of data from known sources based on anatomically and biophysically plausible assumptions as to their generation (e.g., properties of generators, head tissues and the measuring instrument), and (ii) the inverse problem that deals with the reconstruction of the generators from a given data set [26]. The parameters of the inverse problem, such as the number of involved neural ensembles (i.e., generators) and their locations and sizes, can be constrained using a-priori knowledge on morphology and physiology both from invasive methods [27] (e.g., tracer injection studies [28]), and from noninvasive methods such as MRI, particularly functional MRI [29] and diffusion-weighted-MRI [30,31] or

optical methods [32].

In this way, the spatiotemporal evolution of M/EEG can be projected or mapped, for example, into sets of equivalent current dipoles [33] or spatial and/or temporal atoms (e.g., [34, 35]) but the spatiotemporal evolution still requires explanation. Data-driven models, meaning models with minimal assumptions (e.g., linearity), can help with the explanation of the evolution in time and/or in space of given data or, after inversion, data in the source space, as also can multivariate autoregressive models (e.g., [36–39]) or general linear models (e.g., [34]). Such models also provide indications of the network structure in terms of interaction between nodes without the application of any biophysiological or anatomical knowledge [36, 38, 40–47].

All the same, it is particularly useful if generator models are biologically plausible, in the sense that the state variables and parameters are anatomically and physiologically meaningful. Indeed, in order to gain deeper insight into the mechanisms underlying the origin and dynamics of electrophysiological measurements like M/EEG and their relevance to brain function and pathology, such plausibility is essential [4, 48, 49]. It facilitates mapping of the measurements to physically meaningful quantities by inverting (i.e., fitting) the computational model and allowing testing of mechanistic hypotheses about the implementation of brain functions [50]. In order to ensure that this inversion is mathematically tractable and at the same time physically meaningful, the computational mean-field model must strike a balance between mathematical simplicity and biological plausibility [50, 51].

One class of models designed to meet these criteria is referred to as *neural mass models* (NMMs) [52–58]. They describe brain functions on a mesoscopic scale [4, 49], in contrast to single neuron models such as simple integrate-and-fire models [59] and the more elaborated Hodgkin and Huxley model type [60] and its derivatives [61–63]. NMMs quantify the mean firing rates and mean membrane potentials of large neural ensembles, so-called *neural masses* (NMs), using differen-

tial equations [49]. This approach provides an economical yet biophysically meaningful description of phenomena in such electrophysiological measurements as M/EEG. NMMs thus describe brain activity on a mesoscopic scale [49] that is highly relevant for brain function [12–14].

This work deals with a specific but widely used choice of NMM first described by Zetterberg and colleagues [58], also employed by Jansen and colleagues [53, 54], and based on previous modeling work by Lopes da Silva and colleagues [55, 56]. The *Zetterberg-Jansen model* comprises an elementary circuit of three interconnected NMs: *pyramidal cells* (PCs), *excitatory interneurons* (EINs) and *inhibitory interneurons* (IINs), which could be said to describe a localized cortical area (or column), and it has been used to explain both epilepsy-like brain activity [64, 65] and various narrow band oscillations ranging from the delta to the gamma frequency bands [48]. Several such Zetterberg-Jansen models can be combined to describe networks of coupled cortical areas and account for more complex transient and oscillatory behaviors [48, 54, 64, 66–69]. The Bayesian inversion of these dynamic generative models derived from M/EEG data [50, 68] has been developed for the analysis of event-related [68, 70, 71] and steady-state responses [72]. The Zetterberg-Jansen model have been used experimentally to test novel hypotheses about brain function at a systems level [73–75].

For the present work, the author has modified and analyzed the Zetterberg-Jansen NMM for a cortical area, which includes the original Jansen and Rit configuration [54] as a special case: in the Zetterberg-Jansen model as modified, extrinsic input may also target the two ensembles of interneurons, excitatory and inhibitory [66]. The main three emphases of the research are (i) which states this type of NMM of a single cortical area can experience under constant extrinsic input, (ii) under periodic extrinsic input and (iii) how the NMM can be applied to a clinically relevant photic driving experiment.

The first focus is on relatively constant and stable states of probands or patients: for instance, during vigilance, sleep, resting or epileptic

seizure. In order to investigate such states, the system is allowed to settle in a stable regime (e. g., fixed point or limit cycle). For this purpose, the dynamic properties of the modified Zetterberg-Jansen model are described as a function of its key parameters (i. e., extrinsic input levels on all NMs and dendritic time constants). There are rich dynamics expressed by bifurcations (i. e., sudden transitions in dynamic behavior) and *limit cycle* (LC) branches. *Bifurcation* diagrams are used which are compact and intuitively accessible representations of the modes of dynamic systems plotted against changing parameters. LC-branches are systematically classified and there is a detailed discussion of the associated dynamics, including the conditions for changing as a function of key parameters. Knowledge of this dynamic behavior is an important tool, because it tells the modeler how the system will behave. The analysis and the classification yield a comprehensive catalogue of all possible regimes.

The author found that the modified Zetterberg-Jansen model of a single cortical area is intrinsically capable of producing a variety of relevant behavior, especially rhythms, and that it may be more useful for modeling purposes than previously thought. A potential use of the catalogue is that the modeler can decide whether the single-area modified Zetterberg-Jansen NMM is sufficient to model any specific phenomenon (e. g., M/EEG) or whether a more complex model, such as a network of areas, should be chosen. Moreover, the modeler can use the catalogue to select a specific parameter set that best reproduces the electrophysiological data such as Bayesian model inversion schemes [50].

In addition, the bifurcation diagrams provide the modeler with information as to which slow-moving trajectories through parameter space will cross bifurcation points. Apparently complex M/EEG phenomena can thus be explicitly modeled as an *ordered sequence* of switches between different oscillatory regimes. In principle, this enables one to model such phenomena as the progression of pathology, epileptic events (see, for example, [76–78], for thalamocortical models), pharmacologi-

cal intervention, sleep stages [79], or general changes in the oscillatory regime due to contextual state changes. The approach is here illustrated by some synthetic examples. The analysis made enables the selection of highly constrained parameterization. Bayesian inversion should, in principle, be able to identify the free parameters of ordered sequence models: for example, the slowly changing function needed to induce the switching behavior.

The principal types of system topology within the single-area modified Zetterberg-Jansen model are classified in this work. In particular, it is shown that the parameterization chosen by Jansen and Rit [54] gives rise to quite specific system behavior and that this is an exception rather than the rule among the different dynamic regimes. More generally, the predominantly asymptotic behaviors over the entire effective parameter space are shown to be harmonic oscillations of an LC-branch, arising from two Andronov-Hopf bifurcations with oscillation frequencies between 0 and 80 Hz, an observation compatible with the widespread presence of relatively frequency-stable rhythms in brain signals. Anharmonic rhythms arising from global bifurcations (such as of Shil'nikov's type [80]) are thus special and exceptional, but nonetheless important for modeling pathological states such as those in epilepsy.

The second subject of inquiry comes about because local neuronal circuits are embedded in global brain networks and may experience high amplitude time-varying input from other parts of the brain. Because neural ensembles tend to oscillate intrinsically (this is shown in Chapter 5), such cortical input is very often periodic, as evidenced by the widespread occurrence of rhythmic activity in both extracranial and intracranial recordings [81]. For this purpose, a continuous periodic function over time is used as model input, approximating a periodic train of pulses. In this continuous function, each single pulse is similar (but not equal) to the single event used by Jansen and Rit for eliciting visual, evoked potentials [53, 54], or used in Bayesian inversion studies (e. g., [50, 66]). Both amplitude (intensity) and frequency

of the stimulation within the effective ranges are used. These ranges are derived from the work on the first subject, where constant inputs were considered. The entire parameter space is charted with the aid of characteristic *Lyapunov spectra* and the *Kaplan-Yorke dimension* as well as time series and power spectra.

As rhythmic and chaotic brain states are found virtually next to each other, small parameter changes can give rise to switching from one to the other. The *frequency entrainment* effect is found to spread over broader stimulus frequencies for higher stimulus intensities, while away from the entrainment ranges, complex behavior including *periodic*, *quasi-periodic*, and *chaotic dynamics* takes place. Chaotic behavior, in particular, provides continuous spectra of the sort commonly observed in electrophysiological recordings such as M/EEG data. The results indicate that a relatively simple model of a periodically forced local neuronal circuit is capable of producing surprisingly complex and diverse phenomena, which are observable in brain data and relevant for the explanation of brain function.

The third focus is on a deeper understanding of the mechanisms underlying the phenomena observed in a photic driving experiment [82] and on predicting the effects of stimulus frequency and intensity. Electrophysiological measurements such as M/EEG, *local field potentials* (LFP) or *single unit recordings* contain rich information on brain function. The phenomena may be related to specific cognitive processes, to general brain states, or to certain pathological conditions. For example, it is known that stimulation by repetitive light flashes entrains the alpha M/EEG rhythm (i. e., frequency entrainment) [82]. Neurons in the human visual cortex synchronize their firing to the frequency of flickering light, causing the M/EEG alpha frequency to change toward the stimulation frequency [83–85]. Clinically, this resonance effect is called *photic driving*. The occurrence of such an effect is an indicator for the functional flexibility of the cortex and thus a sign of its healthiness. Photic driving is widely used as an activation method in clinical prac-

tice: for instance, when diagnosing epilepsy, migraine, schizophrenia, or depression [86–88].

In order to gain further insight into mechanisms underlying such brain resonance effects and their relevance to brain function and pathology, and to make predictions concerning the stimulation parameters, a modified Zetterberg-Jansen model is again used. Since in the photic driving experiment one has to consider rhythmic input, the version is periodically forced. This is the second subject of the work. The model's response to rhythmic input is also of great importance in many other experimental settings such as those exploring the auditory system by isochronic tones (e. g., [89]).

The author fitted the output of the periodically forced NMM to data from a specific photic driving experiment in terms of frequency detuning and of the largest Lyapunov exponent, which measures the exponential separation or convergence of nearby trajectories. In this way, it was shown that the NMM is suitable for modeling for the dynamics of brain resonance phenomena and demonstrated that useful predictions concerning the parameter choice of entrainment experiments can be derived: the NMM can be used to study the mechanisms of, for example, perception and epileptic seizure generation.

The arrangement of the succeeding chapters is as follows. In the second chapter, neuronal modeling is introduced and the known neural models are outlined. The third chapter contains a general mathematical description of NMMs and the methods used in analyses and numerical calculations. In the fourth chapter the specific NMM of a cortical area is described. In the fifth chapter the model analyses and the results are discussed. Chapter six applies the NMM to the photic driving experiment.

To go into more detail: the 2nd chapter, the background of this work, is divided into four sections. The first is a brief overview of neuronal modeling. The second describes the forward model linking physiological processes to measurements. The third discusses how to

describe neuronal states on different scales. The fourth deals with the mean-field approximation on the mesoscopic scale.

The subject of Chapter 3 is the mathematical development of a general mean-field model and the methods for analyzing it. The existing mean-field models are classified on the general model framework, which is normalized with respect to characteristic physical constants. From this formulation the point-like voltage-based NMM for describing a cortical area is derived, its functions are described and its parameters are discussed in relation to Jansen and Rit [54].

In Chapter 4, the point-like voltage-based NMM is applied to the elementary circuit of a cortical area. The feedback structure of the cortical sheet is introduced and discussed. The PCs are identified as the most important structure for contributing to such electrophysiological data as M/EEG. The voltage-based model is applied to describe the neural states of a cortical area by a nonlinear system of differential equations. Since a single cortical area model is being analyzed, the observer system is simplified before applying to experimental data.

Chapter 5 is the core of this work. The dynamics of the constantly and periodically forced modified Zetterberg-Jansen model are systematically analyzed. The parameter space is discussed and the parameters selected for analysis are justified on the grounds that they make the investigations of the model computationally and mathematically tractable. As it was possible to define effective ranges for the extrinsic inputs, the analyses are complete. Stabilities and bifurcations are investigated as functions of the effective extrinsic input levels and the intrinsic characteristic time constants. The mechanisms for regimes are classified and mapped to the parameter space, so that it is possible to present a scheme for describing complex dynamics in M/EEG data. For the periodically forced model, the parameter space is extended to the intensity and frequency of the periodic extrinsic input. The analysis of the state-space as a function of stimulus intensity and amplitude yields a description of the complex behavior of the model. Finally,

the dynamics of the forced modified Zetterberg-Jansen model (whether forced constantly or periodically) are discussed.

Chapter 6 presents an important aspect, namely the application of the analytical work to experimental data. The periodically forced voltage-based NMM is applied data from a specific photic driving experiment, the aim being deeper understanding of the neural mechanisms which underlie such brain resonance phenomena as photic driving or visual frequency entrainment effects. Using the concept of coupled oscillators it is shown that the modified Zetterberg-Jansen model is suitable for explaining the effects of deterministic and chaotic behavior in such an experiment. Indeed, it is demonstrated that the NMM is useful in analyzing and understanding mechanisms behind brain functions and can be helpful in improving and designing experiments.

In Chapter 7, the model, its analysis, its application and its potential pitfalls are discussed.

2 Neuronal Modeling

*You can't say A is made of B or vice versa.
All mass is interaction.*

Richard Feynman, 1918–1988

This chapter gives the background to the work done. The scientific field of this research is *computational neuroscience* and there is an explanation of the concepts in Section 2.1. The complexity of neural models is discussed in terms of their mathematical tractability and the scales of description. The reasons why the Zetterberg-Jansen NMM is used in the work are made clear from a classification of models and from the relation of this particular NMM to neighboring scientific fields. Since the purpose of using it is to explain extracellular electrophysiological recordings, particularly noninvasive measurements such as M/EEG, the forward model that is necessary to fill the gap between neural mass action and measurements is described in Section 2.2. A brief overview of neural models from the microscopic to the macroscopic level is provided and discussed as the background to the extracellular measurements in Section 2.3. The approach of mean-field approximation that is used in this work for modeling the mean neural states is introduced and a review of mean-field models and its applications is presented.

2.1 Computational Neuroscience

Computational neuroscience, to which this work is a contribution, aims to understand the fundamental mechanisms of information processing in the central nervous system which underlie the brain's enormously complex function in health and disease, ranging, as it does, from primary sensor processing to cognition and motor control [90]. In this scientific field, great importance is placed on the development and the analysis of mathematical models of the central nervous system or parts thereof. Such models are usually based on dynamical system theory, neuroscience and artificial networks.

The central question of how the neural substrate computes particular functions is what distinguishes computational neuroscience from other fields such as biological cybernetics or artificial intelligence [91]. The approach to systems in cybernetics is top-down with black boxes, that is, without any a-priori knowledge about the inner components. *Cybernetics* studies the measurements in order to describe the system behavior (i. e., system identification) [92, 93]. In the case of artificial intelligence, there are various solution approaches, mainly developed to create devices for performing particular tasks of action and recognition (such as speech synthesis and analysis combined with learning and planning). None of these is necessarily concerned with biological processes [94, 95].

2.1.1 Extending the Scientific Method

Computational neuroscience extends the neuroscientific method with the incorporation of mathematical modeling into the cycle of observation, hypothesis, experimentation and independent verification [91].

Mathematical models are thus complementary to experiments when it comes to generating novel mechanistic hypotheses. Such models should principally satisfy three requirements, that they be (i) plausible and (ii) tractable as models, and (iii) that they be capable of predicting

and/or explaining experimental findings [91].

2.1.2 Complexity of Models

The tractability of a model is determined by its mathematical dimensionality in terms of variables and parameters and the complexity of the brain or parts thereof that should be plausibly modeled. The spatial scale over which the brain has to date been experimentally investigated ranges from 10^{-10} m of molecules to 10^{-2} m of fiber tracts and brain structures [90]. The spatial organization can be arranged into a microscopic level of molecules and synapses, a mesoscopic level of neurons and neural ensembles and a macroscopic level of large-scale networks of brain areas [4]. The temporal scale of the measured kinetics is also highly relevant. The dynamics range from 10^{-5} s for gating single ionic channels to weeks of biophysical and biochemical changes (e.g., long-term potentiation) that may underlie memory [91].

2.1.3 Classification of Models

Processes on several spatiotemporal levels have been modeled (see, for example, [96] for review). Mathematical models can be sorted according to these spatiotemporal scales depending on the measurements requiring explanation [90]. Note that a single model may cover several spatiotemporal scales. Particularly at the mesoscopic and macroscopic level (where most recordings are extracellular or even noninvasive), forward models are necessary to describe the experimental data (such as LFP, functional MRI, EEG and MEG). Changes in the state of the brain (e.g., from diseased to healthy or vice versa) may also change the spatial range necessary when modeling a specific process. For instance, the modified Zetterberg-Jansen model used in this work was originally designed to describe a local cortical area but its spatial scale has been extended to larger structures and even to the whole brain in cases when the model is capable of reproducing local phenomena such

as the alpha-rhythm [48] in the somatosensory cortex as well as generalized phenomena of the brain (i. e., of high spatial correlation) such as generalized epilepsy [64, 65]) and the transition(s) between them (see Section 5.1.3 and Section 7.2.3).

2.1.4 Classification of the Zetterberg-Jansen Model

In terms of dynamical system theory and cybernetics [92], the modified Zetterberg-Jansen model (see Chapter 4 for more details) is a closed-loop system comprising positive and negative feedback loops, where the output of a NM (i. e., of the PCs) is positively and negatively fed back to the input through two different NMs (i. e., EINs and IINs). Each set is biologically informed and comprises four input-output elements: synapses, a dendrite, a soma and an axon hillock (Sections 3.1 and 3.2). These elements are linear time-invariant systems, where the axon hillock describes a nonlinear transfer function (i. e., sigmoid function for neural ensembles, see Section 3.2.1 for more details).

Mathematically, the modified Zetterberg-Jansen model can be described as a nonlinear system of ordinary differential equations (see Eqs. (4.1) to (4.7)). In physical terms, the modified Zetterberg-Jansen model is a dissipative (see Section 5.2.3) and open system (see Fig. 4.1) with respect to the interactions with the extrinsic domains (i. e., there is extrinsic input on each of the three NM, and the NM of PCs projects back to the extrinsic domain). The modified Zetterberg-Jansen model is a self-sustained oscillator and a multi-stable system depending on the applied parameter set (see Section 5.1.3).

Based on a worst-case analysis of the parameter space (see Section 5.1.1), the modified Zetterberg-Jansen model is studied in the present work using the methods of mathematics and systems theory (see Section 3.3). There is analysis, for instance, of bifurcations (see Section 5.1.2), characteristic Lyapunov spectra and Kaplan-Yorke dimension (see Section 5.2.2).

Because the modified Zetterberg-Jansen model is an elementary cir-

cuit that can be interpreted in several respects (as presented above) it may applied in broader scientific fields such as engineering and automation of feedback systems or physics of self-organizing systems [97].

Finally, the Zetterberg-Jansen model [53,54,58] that is modified, analyzed and applied in the present work describes a synchronized cortical area (i. e., cortical neural ensemble) which is capable of comprising several extracellular measurements on different scales depending on the forward model. Although the aim of this research is to describe phenomena in M/EEG data, a general scheme of the forward model is presented in Section 2.2. The descriptions of the neuronal states are introduced in Section 2.3.

2.2 Forward Model

When the most important questions in neuroscience are being tackled, the underlying information processes (e. g., electrochemical processes) are usually hidden (e. g., for M/EEG) and, therefore, a forward or generative model for brain measurement such as M/EEG can be specified by two separate systems: the state \mathcal{P}_ϕ and the observer system \mathcal{P}_χ

$$\phi = \mathcal{P}_\phi(\psi, \theta_\phi), \quad (2.1)$$

and

$$\chi = \mathcal{P}_\chi(\phi_\chi, \theta_\chi) + \epsilon. \quad (2.2)$$

The state system \mathcal{P}_ϕ explains the usually hidden neuronal states ϕ such as the flow of ions through the membrane of nerve cells at the microscopic level as an explanation of patch-clamp data, or the mean membrane potentials of neural ensembles at the mesoscopic and macroscopic level that potentially generate M/EEG [4]. The observer system \mathcal{P}_χ relates the relevant neuronal states ϕ to the measurements χ (e. g.,

membrane potentials of cortical PC ensembles to M/EEG). The states ϕ are parameterized by θ_ϕ and described by the operator \mathcal{P}_ϕ , usually a differential operator under the perturbation ψ covering different types of input: sensory input (e.g., light, odor or pressure), experimental manipulations (e.g., medication or transcranial magnetic stimulation), and input from structures; even covering processes that are not explicitly considered (e.g., glia cells or vascular and muscle motion). The observations χ are, in a uniform manner, parameterized by θ_χ and described by the operator \mathcal{P}_χ linking relevant states $\phi_\chi : \phi_\chi \subseteq \phi$ to the measurements χ linearly superimposed by noise processes ϵ such as thermal noise of the measuring apparatus. The observer system \mathcal{P}_χ has to take into account a physical model [70] of the sources (e.g., the equivalent dipole model) [27, 98], the media (i.e., geometry and tissue of the head) [99, 100] and the measuring apparatus (e.g., SQUID^a magnetometry or electrodes and amplifier) [26, 101].

For the state system \mathcal{P}_ϕ a NMM of a cortical area is what is need in this work; and for the observer system \mathcal{P}_χ a linear output function (leadfield). In this work, it is not necessary to consider leadfield modeling because only a single area is modeled. The state systems will be described in more detail in the following paragraphs.

2.3 Neuronal States

Developing biophysical informed models of the brain or parts thereof, one gains an insight into the formation of operations underlying brain functions such as stimulus adaption, learning or pattern discrimination [4]. From this insight, the options are to design very detailed and thus complex models or to design reduced and therefore simple models [96]. Due to the vast diversity of biophysical (e.g., cell types), biochemical (e.g., neurotransmitters) or morphological entities (e.g.,

^a*Superconducting QUantum Interference Device*, for short SQUID, is used as a sensitive biomagnetic field detector. See section 2.2.3 in Andr  and Nowak [26] for more details.

size of cell bodies) (e.g., [102, 103]) modeling the whole brain in every detail would produce working brain copy of enormous complexity. Such a unified model, covering the whole range from the micro- to macroscale (bottom-up), would lack tractability and suffer from incomprehensibility [91]. In particular, the huge number of variables to be initialized and parameters to be specified would result in mathematical intractability for directed predictions and explanations. It must be admitted that such a brain replica would offer an alternative to the model organism approach and would obviate invasive experiments. However, because neurons are embedded in networks for interaction at different scales, it is to be expected that networks will follow common laws of operation, given the anatomical and physiological similarity that exists throughout the brain (or at least in parts) [4, 104]. Hence, the physical reduction processes (simplification, approximation and idealization) of the brain inspire qualitative models [49]. To meet particular challenge of balancing biological plausibility against mathematical and thus computational tractability, several models have been developed and analyzed under different aspects at different scales depending on the measurements it was desired to explain.

2.3.1 Neurons – The Dynamic Computational Units

In the school of thought that sees the brain (or more generally the whole central nervous system) as automata (i.e., an information processor) it is a fair assumption that functional specialization emerges from interactions of the dynamical computational units, the neurons [105]. At a neuron, information converges from 10^2 neurons and diverges to approximately 10^3 other neurons featuring a spatiotemporal pattern [91]. One assumes that the pattern of emitted action potentials (i.e., jitter of firing rate and timing) evolving in time and space encodes information shared by neurons (i.e., an information unit) in a neuronal circuit [105]. This is one way of describing the microscopic level on which all representations and computations rest [4]. For instance, at

this level models have successfully described the ionic fluxes through the membrane of neurons forming action potentials [60] as measured with single-cell recordings (e.g., the patch-clamp technique) or the release of neurotransmitters in the synaptic cleft and its receptors governing the efficacy of synaptic connections between neurons (e.g., [106]), as measured biochemically. On the basis of such microscopic descriptions, complex compartment models can be composed [107–110]. Simplified neuronal models such as the abstract integrate-and-fire models [111] or detailed neuronal models such as the Hodgkin-Huxley model and its derivatives (for a review see [109, 112, 113]) contribute to the understanding of neuronal computations at the microscopic level [109, 110].

2.3.2 Ensembles – The Unit of Brain Functions

Computations underlying brain functions such as action, perception, learning, language and cognition are, in what has so far been said, assumed to operate from neural ensembles at the mesoscopic level (e.g., [3, 4, 114]). There is an alternative school of thought which hypothesises that individual neurons are highly specialized (for a discussion see [115]) which would imply the modeling and study of networks that comprise up to an order of 10^{11} neurons at the microscopic level (e.g., [116]). However, electrophysiological studies [117–119] provide evidence that the cerebral cortex is, indeed, functionally organized in vertically oriented columns of 2×10^{-6} m to 5×10^{-8} m in diameter containing 10^2 to 10^5 of neurons (for a review see [120]). Neural ensembles arise through functional integration of neurons due to strong interconnections at the microscopic level (i.e., local connections) to a common state when a certain number of neurons are coherent stimulated (e.g., by synchronization [105, 121]). A further support for this view is an assumption of fundamental correspondences among anatomical structures, their functions and the spatiotemporal pattern of activity [122]. At the mesoscopic level, models usually approximate the complex microscopic level and describe the density or the mean of the spatiotemporal

dynamics of neural ensembles, such as the mean *postsynaptic potentials* (PSP) or mean of action potentials (or firing rates) as extracellularly measured, for instance, with LFP [4]. On the basis of such mesoscopic models, networks of local brain areas (e.g., [54, 55, 123]) or whole brain networks can be composed. At this macroscopic level, there are pathways like large axons running through the cortex (gray matter) and fiber bundles running through the white matter interconnecting the hemispheres (i.e., long-range connections [124]). They selectively bind emerged specific neural ensembles at the macroscopic level [105] forming metastable patterns [115, 125]. Models at the mesoscopic level are able to explain the dynamics at the macroscopic level [69, 126] which are found with appropriate temporal resolution when noninvasive measurements like M/EEG take place [12, 13].

2.4 Mean-Field Approximation

It is thought that the emergence of specific neural ensembles is what supplies the functional elements of brain activity which carry out the basic operations of informational processing [3–11, 115, 125]. From this point of view, the states of an emerged neural ensemble rather than those of single neurons are of interest. In the tackling of the problem of diversity of a neural ensemble at the mesoscopic level, mean-field theory is of assistance, approximating the states of an ensemble. Mean-field theory primarily arose in statistical physics when dealing with complex systems and is extensively used there [127]. A famous example, (mentioned in [4]) is the description first by Maxwell and then by Boltzmann of the motion of gas molecules, which was found by the approximation method using temperature and pressure.

2.4.1 Ensemble Density Models

If one applies the mean-field approximation to neurons at the mesoscopic level one can describe the density dynamics of neural ensembles

– the so-called population or ensemble density models [4, 109, 128–138]. Such models explicitly deal with the effects of stochastic influences (e. g., action potential timing), so that probability densities over trajectories in the state space provide a probabilistic description of the variability (or randomness) of a neural ensemble. Smooth effects of stochastic influences such as diffusion processes can be described by stochastic or partial differential equations, in particular by use of the Fokker-Planck formalism [4]. For example, in physics, the Fokker-Planck equation is used to describe Brownian velocity in fluids and gases or laser noise [139]. Further constraints are required: for instance, that the ensemble has a Gaussian distribution due to a present stimulation and that the non-linearity does not dominate the interacting elements [4, 128]. Deco and colleagues [4] describe the approximation of ensemble dynamics by their probabilistic evolution (e.g., Fokker-Planck equation) based on a single spiking neuronal model (i. e., integrate-and-fire model). The ensemble density approach can be related to measurements like EEG, for example, by the expectation value (or mean) of firing rates or membrane potentials of an average neuron within an ensemble [130]. However, numerical calculation of the probabilistic evolution for given initial conditions of neural ensemble dynamics (i. e., integrating the Fokker-Planck equation) would usually require binning of the continuous density (i. e., state space). Attention to multiple states of a neural ensemble would result in a vast number of differential equations and thus parameters. The density approach is thus not feasible for systematic parameter studies [4] or even system inversions (e.g., Bayesian techniques). The options necessitated are to reduce the number of states and/or approximate the ensemble densities can be approximated (e.g., linearly).

NMMs are a special case of the ensemble density approach which are in line with both state reduction and approximation. Here, the ensemble dynamics with all their diversities are reduced to an averaged neural state of a neural ensemble such as mean firing rate or mean mem-

brane potential (i. e., expectation values of densities). Thus, NMMs are parsimonious in terms of parameters and suitable for parameter study and for system inversions of given data like that of M/EEG [50]. The main impact of this reduction is that it enables the states to be coupled simply by the expectation (i. e., first moment) of a state, while the Fokker-Planck formalism permits coupling of each statistical moment of a probability density within and between neural ensembles. Finally, the Fokker-Planck formalism explicitly shows the variability of a state, whereas the reduced NMMs only features variability implicitly (i. e., slope of the sigmoidal transfer function [140–142]). The interested reader will find more on this general subject in the excellent papers about density models [4, 130] and the citations therein. What is dealt with in the present work is NMMs, and the following subsection introduces the concept and the related mathematics.

2.4.2 Neural Mass Models

NMMs provide an explanation of averaged dynamics of neural ensembles at a mesoscopic and macroscopic level and were designed to strike a balance between mathematical simplicity and biological plausibility. They are a type of model widely used for explaining electrophysiology measurements (e. g., [50, 64, 69]). In line with the mean-field theory, NMMs summarize the states of neurons within an ensemble (i. e., mean firing rate and mean membrane potential) assuming a point ensemble or point mass (i. e., delta-density distribution). Hence, NMMs are a special case of the ensemble density approach. The distinguishing feature is that, in contrast to ensemble density models, after approximation only first-order moments are available for coupling the average states within or between NMs. NMMs usually describe two states, namely mean firing rates and the mean PSPs using the familiar dynamic firing rate model [109, 141]. The term NMM goes back to the fundamental work of Freeman [49], who used the name neural mass action model. These he introduced as an alternative to ensemble density models [4].

To meet the spatial extension of neuronal dynamics, NMMs can be defined as mean-field models assuming a homogeneous continuum of the neuronal substrate. Such neural mean-field models are thus a generalized formulation of NMMs.

The following subsections deal with the concept behind NM modeling. Neural-field models and NMMs are briefly reviewed and discussed.

Concept of Describing Neural Mass Action

The motivation for NMMs is the desire to describe of the basic electrophysiological features of neurons with as few parameters as possible. Since the information processing underlying brain functions such as action, perception, and cognitive functions in health and disease is carried out by ensembles of interacting neurons [3–11], it is not necessary to take each single neuron into account. Thus, neural ensembles are assumed to be the basic units for brain function. This assumption is confirmed from observation with electrophysiological measurements such as M/EEG and LFP [12–14]. M/EEG reflect the synchronous activity of 10^5 to 10^9 of neurons (i. e., mean postsynaptic activity) rather than single neural activity (e. g., action potentials) [143].

To summarize, the idea is to develop models which are biophysiologicaly inspired (i. e., mechanisms) which are plausible (i. e., parameters), and which are, at the same time, parsimonious: to describe the mesoscopic and macroscopic level of neural ensembles as observed electrophysiological approaches like M/EEG. The parsimony should leave scope for model inversions to allow data to be fitted in corroboration of experimental hypotheses (e. g., using Bayesian techniques) and for parameter studies to underpin new hypotheses (e. g., the designing of new experiments and/or models).

According to Freeman’s approach, similar neurons can be lumped together as so called neural mass (NM) described with only one set of parameters using mean-field approximations.

It follows that an ensemble state is the synchronous activity of simi-

lar neurons within a NM. Underlying this is a classification of neurons because the neuronal substrate features homogeneity of certain features (e. g., cell densities) as well as heterogeneity of others (e. g., cell shapes). A classification could be made in terms of morphology (e. g., layer or position, shape and cytoarchitecture) such as Brodmann's parcellation of the human cerebral cortex [144] and/or in terms of physiology (e. g., excitability and activation patterns) [102,145,146]. In this view the neuronal substrate under consideration is homogenized and decomposed by a set of NMs, where each set or class is determined by a set of a few (equivalent) parameters. Following Freeman's terminology classifications are subject to the following assumptions [49]:

- (a 1) neurons must share the same input with adjacent neurons – uniform excitation;
- (a 2) the state of a neuron depends on the input – uniform state.

Given (a 1) and (a 2) there will be two basic types of NMs: KO-sets and KI-sets (K for Katchalsky) for designing networks based on the following assumptions of embeddedness:

- (a 3) neurons of a neuronal set do not interact with each other;
- (a 4) within a neuronal set each neuron is uniformly connected with vicinal neurons.

In accordance with considerations (a 2) to (a 3), a KO-set is characterized by a pool of similar neurons with a common input (a 1), driving the neurons in a common state (a 2) so that the neurons produce a common output (i. e., excitatory or inhibitory) without having interactions (a 3). A KI-set is then a collection of similar and homogeneously interconnected (a 4) neurons with a common input (a 1) and output (a 2). On the basis of these two fundamental types of NMs, networks can be developed in a way, such that a KII-set consists of interacting KI-sets, and so forth. Again, the two sets differ in their interconnectivity.

Since neurons in a KO-set do not interact with each other, the average state of such an ensemble can be deduced from a single neuron, or, in other words, the ensemble behaves just like a single neuron. As a consequence, a KO-set can physiologically be compared to exemplary single neurons and thus described, for instance, using a Hodgkin and Huxley model [60] or a integrate-and-fire model [111]. Because throughout the brain neurons are embedded in networks [124,147] a set of isolated neurons is a purely academic concept. For practice, KO-sets convert to scaled single-cell models at the microscopic level, and KI-sets are more relevant for modeling both the microscopic and the macroscopic level. In contrast to KO-sets, because KI-sets take interconnections among neurons into account, the emerging states depend strongly on the interactions and cannot be reduced to states of a generic single neuron. As a consequence, for specifying KI-sets analogous models or equivalent parameters for single neural models have to be found. Equivalent parameters can be determined using in-vivo single-cell recordings or intracranial measurements like LFP.

Spatially Distributed Dynamics – Neural Field Models

The first neural field models were published in the 1950s and 1960s [148–150]. Wilson and Cowan [141,142] formulated a neural field model for membrane potentials and Nunez [57] derived an equivalent description of a neural field which took into account firing rates rather than membrane potentials. The neural fields in both these sources consider two coupled ensembles of excitatory and inhibitory neurons. These equivalent descriptions were analyzed by [57,151,152] and generalized by [153,154]. Due to the spatial extension and the finite propagation via axonal time delays [153,154], distributed time delays [155,156] were introduced and analyzed (e.g., [155–160]). Neural field models were applied as generative forward models for electrophysiological data such as M/EEG or LFP incorporating physiological details for a number of purposes, the generation of rhythms [13,126,161] during sensorimotor

coordination [153,154], for producing event-related potentials [162,163] or for indicating anesthesia [164–166], epilepsy [167–169] and stages of sleep [79]. Interested readers can refer to excellent reviews by Jirsa [6] and Ermentrout [170] on neural field models and the citations therein.

The connections between neural ensembles take a major aspect in neural field models, because such models especially focus on the functional role of spatial patterns of neuronal states. It is thus assumed that the structural connectivity shapes functional dynamics in terms of brain function [171] and also during brain development [172]. From the architecture of the brain, neural connections, or more precisely axonal projections has to be classified, for instance, by means of their spatial range (e.g., distance between the locations of the projecting neuron or neural ensemble and its targets) or pathway (e.g., running within or by leaving and/or entering the cortical sheet) [124], diameters or densities (i.e., number of axon fibers per cross sectional area) [173,174] and/or myelination (e.g., number of oligodendrocytes) [175]. For example, the time of an action potential for propagating along axons depends particularly on two factors: (i) the geometry (length of the pathway and the axonal diameter, e.g., [176,177]), and (ii) the degree of myelination (e.g., [178]). Considering the whole human brain, a so-called connectome [171,179], that is, a complete description of the structural connectivity, can be assessed by considering multiple recording techniques such as in vivo diffusion-weighted MRI (e.g., [30,31]) or post-mortem: dissection techniques [180,181], tract tracing (e.g., [182]) or optical methods [32].

In order to study neural field models at the macroscopic scale such a connectome can be approximated locally to be homogeneous, meaning translationally invariant (i.e., short-range connections) and globally to be heterogeneous, meaning sparse and translationally variant (i.e., long-range connections) [6]. Homogeneity could be defined, for example, by a cytoarchitectonic parcellation of the cortex, according to Brodmann [144], into regions of approximately $2 \times 10^{-2} \text{ m}^2$. In case of spatially

homogeneous connections, the spatiotemporal dynamics of neural field models are well studied (e. g., [126, 142, 154, 157]), where, for instance, the connectivity probability decays exponentially over the distance (see Section 3.1.3). Its worth to note that the impact of heterogeneous (long-range) connections were analyzed [183, 184].

Mean-field models are computational expensive and parsimonious only under such restrictive conditions as homogeneity. Consequently, a model inversion, for example, using a Bayesian inference scheme, is limited. The integration of the mean-field equations (e. g., integro-differential equations) requires binning of the space, which leads to a spatial arrangement of point masses.

Describing such electrophysiologically measurements as M/EEG at the macroscopic scale requires a coarse sampling of the spatial domain (e. g., dividing the cortex in areas of $1 \times 10^{-2} \text{ m}^2$), because of the relative low spatial resolution of the techniques (e. g., relative to functional MRI or two-photon excitation microscopy). Thus, a point mass comprises the local homogeneity (i. e., a NM) and the connections between such NMs comprises the heterogeneity of a connectome. Furthermore, from the point of view of analyzing M/EEG one tries to explain the data with a minimum of generators (e. g., a set of equivalent current dipoles). Consequently, for model inversion, NMMs that comprise spatially sparse networks of NM (e. g., number of NMs is less or equal to the number of sensors) are more appropriated.

Point-Like Dynamics – Neural Mass Models

NMM has been used for explaining rhythms in health [48, 51, 54–56, 58, 64, 69, 123, 163, 168, 185–189, 189–196] and disease [51, 58, 64, 65, 162, 168, 169, 192], event-related [53, 54, 67, 68, 70, 71, 73, 74, 163] as well as steady-state responses [72, 197] and interactions in network [48, 54, 64, 66–69, 73–75, 169, 190, 192–196, 198]. It has been possible to design such models exploiting diffusion-weighted- [69, 195] as well as functional MRI [69, 190, 193, 195, 196] and to combine them with hemodynamic

models in order to explain functional MRI-data [195].

The first point-like NMM was published by Lopes da Silva in 1974 [55] about two decades after the first mean-field model [148], and before Freeman wrote his fundamental work in 1975 [49]. Lopes da Silva and coworkers [55] presented a linear two-ensemble model of the thalamus (i. e., interacting excitatory relay cells and IINs) capable of generating and examining the alpha-rhythm (frequency band around 10 Hz) which is widely observable in M/EEG-data. Later, this model was extended to the spatial domain explaining phase velocities [185]. Another extension by Zetterberg and co-workers describes a three-ensemble model of the cortex referring the ensembles to local cortical excitatory PCs and EINs as well as IINs [58]. This takes into account the nonlinear properties (e. g., time-invariant sigmoid shape of activation) of interacting neurons and ensembles. Nearly ten years later, Freeman [123] studied the olfactory system using a nonlinear NMM of twelve ensembles forming a KIII-set (i. e., of three KII-sets, each consisting of excitatory and inhibitory KI-sets formed with two KO-sets), which shows deterministic chaos similar to M/EEG patterns. In 1993 Jansen and colleagues picked up the local cortical model of Zetterberg and colleagues [58] and modified it (i. e., by neglecting self-projections of PCs) to study visual event-related potentials [53], and, later, the alpha-rhythm in EEG [54].

Cortical Models

The single cortical area model has been used to explain both epilepsy-like brain activity [64, 65] and various narrow band oscillations ranging from the delta to the gamma frequency band [48, 51, 187]. The underlying mechanisms of rhythms, in terms of bifurcations, were identified by [189] for the Jansen and Rit configuration [54], and, more generally, by [51] for Zetterberg's model structure regarding the effective input ranges on all three neural ensembles or masses. A natural extension of this local approach is to model a spatially distributed network of cortical areas as a collection of coupled single-area models, thereby

accounting for more complex transient [54, 64, 66–68, 70, 73–75] and oscillatory behavior [48, 54, 64, 69] for the purpose of studying interactions, for example, [190, 193, 194, 196, 198]. The inversion of these dynamic generative models from given M/EEG data (e.g., [187, 190, 193, 196], or Bayesian inversion, 'dynamic causal modeling' [50, 68], available in the free academic software 'Statistical Parametric Mapping' [199]) has been developed for the analysis of event-related [68, 70, 71], steady-state responses [72, 197] and rhythms [187, 190, 193, 196]. These techniques, using a cortical area model [53, 54, 58], have been used experimentally to test novel hypotheses about brain function at a systems level [73–75, 190, 193, 196].

Thalamus and Thalamocortical Models

However, the cortex cannot be considered in isolation. One of the most important input and relay stations for the cortex is the thalamus. Several studies have drawn on Lopes da Silva's thalamus model [55, 56] and studied nonlinearities involved in generating the alpha-rhythm in EEG-data [186]. Furthermore, thalamocortical models (i.e., coupling thalamus and cortical areas) have been designed for explaining focal attention through event-related desynchronization and synchronization in the M/EEG alpha- [188], beta- and gamma-band [191] such models have also addressed rhythms [69, 163, 195], as well as event-related potentials [163], and epileptic seizures [168, 169, 192]. The contribution of the thalamus to cortical rhythms in thalamocortical models was structurally analyzed by [200].

3 Mathematics and Methods

*In mathematics you don't understand things.
You just get used to them.*

John von Neumann, 1903–1957

The mathematical backbone and the analysis methods are the subject of this chapter. Section 3.1 develops the general mathematical framework for modeling the mean activity of a NM. In Section 3.2 the basic ordinary differential equations for describing the NMs in the modified Zetterberg-Jansen model [54, 58] are derived and discussed. The methods and algorithms that are used to study the dynamics of the NMM and the experimental data are listed and described in Section 3.3. The experimental paradigm is shown in Section 3.4.

3.1 Mean-Field Framework

The NMs that constituted the Zetterberg-Jansen model which this piece of work has used in modified form can be directly derived from a general framework of the mean-field of the neural substrate. The modification was necessary because the existing generalized mean-field approach of Jirsa and Haken [153, 154] took no account of (i) the integration of temporal kinetics of axons and dendrites and (ii) the incorporation of velocity distributions of propagation delays. Extending the Jirsa and

Haken [153, 154] formulae to incorporate the first factor, in particular, meant that the kinetics of the point-like NMs in the Zetterberg-Jansen model could be described. This provides a sufficient framework for most of the neural point-like and spatial distributed mean-field models.

Having extended the general mean-field framework a second-order ordinary differential equation is derived, describing the point-like NM. The elementary functions and operators are discussed and the parameters are related to the parameters used by Jansen and Rit [54] that can be traced back to the works of Lopes da Silva [55] and Freeman [49].

3.1.1 Definition

The neural state $\phi(t) = (u \ m)^T$ of a neural ensemble (this term describes synchronous activity in a NM) at time t comprises the mean PSP $u(t)$ and the mean firing rate $m(t)$. The PSP describes the activities of the dendrites and the cell bodies, which are assumed to be chemically passive, while the mean firing rate describes the actions of the axons with their passive and active processes. Two conversion operators are used: (i) a rate-to-potential operator that captures the PSPs due to presynaptic firing, (ii) and an potential-to-rate operator, accounting for the firing patterns as a function of the PSP.

According to the definition of Jirsa and Haken [153, 154] the neuronal mass Ω is considered as a continuous field of mean potentials and mean firing rates. Additionally, in the present framework, Ermentrout's views of activity- and voltage-based models are included (see Fig. 3.1). The rate-to-potential conversion $\mathcal{Q}_j(r_1, r_2, t)$ computes the PSP, relative to the resting membrane potential, $u_j(r_2, t)$ at the synpto-dendritic complex for a (target) class of neural ensemble $j : j \in J$ located at r_2 from the mean firing rate $m_j(r_1, t)$ of all neural ensembles located at

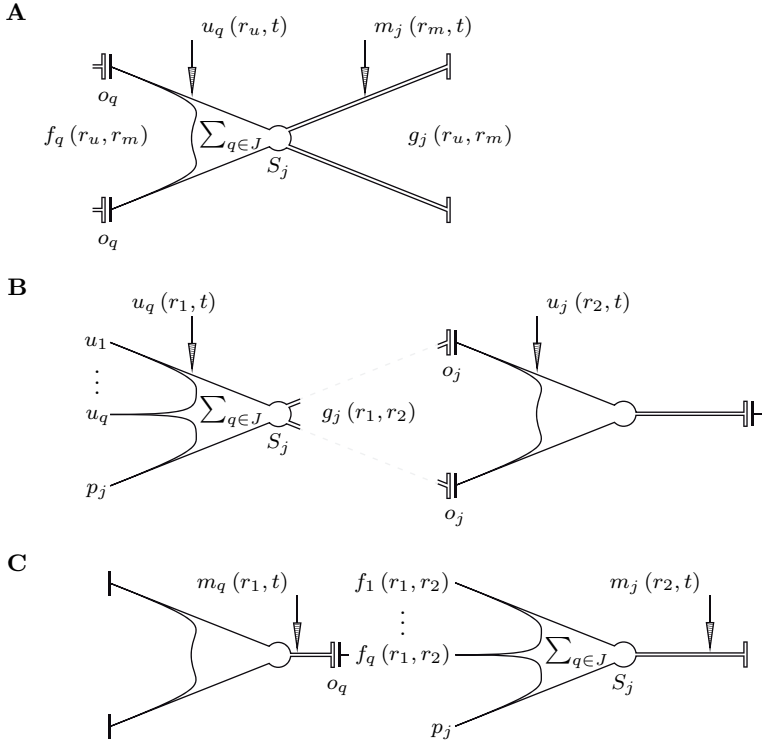


Fig. 3.1. Synaptic terminals interconnect structures of neural ensembles **A** assuming arborized axons **B** or dendrites **C**. In the principal scheme **A** axonal projections terminate on a neural ensemble of type j through synapses distributed over the dendritic tree with $f_q(r_u, r_m)$ depending on projecting ensemble q . The effect of the mean action potentials $m_j(r_m, t)$ (i.e., firing rate) recorded at r_m hitting terminals on the mean PSPs $u_q(r_u, t)$ recorded at r_u is linear and scaled by o_q . PSPs $u_q(r_u, t)$ passively superimpose along the dendritic tree towards the soma over types $\sum_{q \in J} u_q$ and convert back to a mean firing rate at the axon hillock by the transfer function S_j . Axonal projections of the ensemble type j transmit the caused mean firing rate in space with $g_j(r_u, r_m)$. Voltage-based models **B** describe the summed PSPs $u_j(r_2, t)$ of single dendrites for intrinsic u_q and extrinsic projections p_j of ensembles of type j located at r_2 due to distributed terminating axons $g_j(r_1, r_2)$ from ensembles at r_1 . Activity-based models **C** describe the mean firing rates $m_j(r_2, t)$ of single axons, each for an target class of ensemble j at r_2 due to PSPs of distributed dendrites $f_q(r_1, r_2)$ caused by ensembles located at r_1 . For a detailed description see Chapter 3.1.1.

r_1 in the considered spatial domain Ω of neural mass, so that

$$u_j(r_2, t) = \int_{\Omega} dr_1 f_j(r_1, r_2) \mathcal{Q}_j(r_1, r_2, t), \quad (3.1)$$

with the corresponding spatial distribution function $f_j(r_1, r_2)$ of dendrites describing the contribution or connectivity of the rate-to-potential conversions \mathcal{Q}_j at location r_1 to the PSP u_j at a target location r_2 . Note that the set J could denote types of neural ensembles $j \in J$ or specific types of connections (e.g., projections of IINs on PCs). The potential-to-rate operator $\mathcal{O}_j(r_1, r_2, t)$ computes the mean firing rate $m_j(r_2, t)$ at the axon hillock for a target class of a neural ensemble located at r_2 caused by the PSPs $u_j(r_1, t)$ of ensembles located at r_1 in Ω

$$m_j(r_2, t) = \int_{\Omega} dr_1 g_j(r_1, r_2) \mathcal{O}_j(r_1, r_2, t), \quad (3.2)$$

with the spatial distribution function $g_j(r_1, r_2)$ of axons depending on the spatial connectivity. The following considerations assist with the combination of Eqs. (3.1) and (3.2):

- (a 1) In ensembles of neurons the rate-to-potential conversions at chemical synapses are linear [49, 108, 201, 202], and
- (a 2) the potential-to-rate conversion of the axon hillock is nonlinear [49, 203–205].
- (a 3) PSPs as well as action potentials and thus mean firing rates are temporally low-pass filtered when propagating through dendrites [108, 201, 202, 206–209] and axons [206, 208, 210].
- (a 4) Extrinsic inputs are established such that afferent axons terminate on dendrites at chemical synapses.

Taking (a 1) to (a 4) into account, it is possible to define both conversions as temporal convolutions of the input response functions $h_j(t)$

and $k_j(t)$ with the mean firing rate $m_j(r_1, t)$ and the PSP $u_j(r_1, t)$:

$$\mathcal{Q}_j(r_1, r_2, t) = o_j \int_t ds h_j(t-s) \quad (3.3)$$

$$\times \int_{\Gamma} dv l_{m_j}(v) m_j(r_1, s - \Delta_{m_j}(r_1, r_2)/v),$$

$$\mathcal{O}_j(r_1, r_2, t) = \int_t ds k_j(t-s) \int_{\Gamma} dv l_{u_j}(v) \quad (3.4)$$

$$\times S_j\left(p_j(r_1, s - \Delta_{u_j}(r_1, r_2)/v)\right)$$

$$+ \sum_{q \in J} u_q(r_1, s - \Delta_{u_q}(r_1, r_2)/v),$$

where $\Delta_{u_j}(r_1, r_2)/v$ and $\Delta_{m_j}(r_1, r_2)/v$ denotes time delays due to finite propagation speed $\Gamma : v \in \mathbb{R}^+$ along dendritic and axonal distances $\Delta_{u_j}(r_1, r_2)$ and $\Delta_{m_j}(r_1, r_2)$ with the specific velocity distribution functions $l_{u_j}(v) : \mathbb{R}^+ \rightarrow \mathbb{R}^+$ and $l_{m_j}(v) : \mathbb{R}^+ \rightarrow \mathbb{R}^+$ of ensemble $j \in J$ between r_1 and r_2 [57, 141, 154], o_j is simply a factor to scale the linear effect, $p_j(r_1, t)$ is extrinsic input, and $S_j(u)$ is a differentiable and steadily increasing transfer function $S_j : \mathbb{R} \rightarrow \mathbb{R}^+$. Both impulse-response functions $h_j, k_j : \mathbb{R} \rightarrow \mathbb{R}$ are continuous and integrable for all $t \in \mathbb{R}$. For a scheme of the neural ensemble see Fig. 3.1. The impulse-response functions can be recast as Green's functions and thus satisfy the preconditions $D_j k_j(t) = \delta(t)$ and $C_j h_j(t) = \delta(t)$, where $C_j(\partial/\partial t)$ and $D_j(\partial/\partial t)$ are the temporal differential operators with the polynomials C_j and D_j of constant coefficients $C_j(\lambda_u) = \sum_{i=0}^{n_u} a_i \lambda^i$ and $D_j(\lambda_m) = \sum_{i=0}^{n_m} b_i \lambda^i$ of the orders $n_u \geq 0$ and $n_m \geq 0$, and δ is the Dirac delta function

$$\delta(t) = \begin{cases} \infty & t = 0 \\ 0 & t \neq 0 \end{cases}, \quad (3.5)$$

with $\int_{-\infty}^{\infty} \delta(t) dt = 1$. Hence, the conversions (3.3) and (3.4) can be

read as follows

$$C_j \left(\frac{\partial}{\partial t} \right) \mathcal{Q}_j (r_1, r_2, t) = o_j \int_{\Gamma} dv l_{m_j} (v) \quad (3.6)$$

$$\times m_j (r_1, t - \Delta_{m_j} (r_1, r_2) / v),$$

$$D_j \left(\frac{\partial}{\partial t} \right) \mathcal{O}_j (r_1, r_2, t) = \int_{\Gamma} dv l_{u_j} (v) \quad (3.7)$$

$$\times S_j \left(p_j (r_1, t - \Delta_{u_j} (r_1, r_2) / v) \right. \\ \left. + \sum_{q \in J} u_q (r_1, t - \Delta_{u_q} (r_1, r_2) / v) \right).$$

Inserting the differential equations for the conversions (3.6) and (3.7) into the state Eqs. (3.1) and (3.2) yields the main integro-differential equations for the two spatiotemporal states in relation to each other

$$C_j \left(\frac{\partial}{\partial t} \right) u_j (r_2, t) = o_j \int_{\Omega} dr_1 f_j (r_1, r_2) \int_{\Gamma} dv l_{m_j} (v) \quad (3.8)$$

$$\times m_j (r_1, t - \Delta_{m_j} (r_1, r_2) / v)$$

$$D_j \left(\frac{\partial}{\partial t} \right) m_j (r_2, t) = \int_{\Omega} dr_1 g_j (r_1, r_2) \int_{\Gamma} dv l_{u_j} (v) \quad (3.9)$$

$$\times S_j \left(p_j (r_1, t - \Delta_{u_j} (r_1, r_2) / v) \right.$$

$$\left. + \sum_{q \in J} u_q (r_1, t - \Delta_{u_q} (r_1, r_2) / v) \right).$$

3.1.2 Activity-Based and Voltage-Based Models

This developed general model is an n th-order system of integro-differential equations, where $n = n_u + n_m$. However, the two state conversions (3.8) and (3.9) are at this stage spatially not yet connected so as to yield a closed form. For this purpose at least one of the two spatial distribution functions $f_j (r_1, r_2)$ and $g_j (r_1, r_2)$ must be δ -like. Neglect-

ing the arborizations of dendrites $\lim_{r_1 \rightarrow r_2} f_j(r_1, r_2) = \delta(r_2 - r_1)$ (see Eq. (3.5)) and the corresponding time delay $\lim_{r_1 \rightarrow r_2} \Delta_{m_j}(r_1, r_2)/v = 0$ reduces the rate-to-potential conversion (3.8) to

$$C_j \left(\frac{\partial}{\partial t} \right) u_j(r_2, t) = o_j m_j(r_2, t). \quad (3.10)$$

This simplification allows insertion of the potential-to-rate conversion (3.9) into the ratio-to-potential operator (3.10), thus canceling out the mean firing rate $m_j(r_2, t)$

$$\begin{aligned} L_j \left(\frac{\partial}{\partial t} \right) u_j(r_2, t) &= o_j \int_{\Omega} dr_1 g_j(r_1, r_2) \int_{\Gamma} dv l_{u_j}(v) \\ &\times S_j \left(p_j(r_1, t - \Delta_{u_j}(r_1, r_2)/v) \right. \\ &\left. + \sum_{q \in J} u_q(r_1, t - \Delta_{u_q}(r_1, r_2)/v) \right), \end{aligned} \quad (3.11)$$

with the differential operator $L_j = C_j D_j$ of order $n = (n_u + n_m) \geq 0$.

This approach to developing the system equations (3.8) and (3.9) with respect to the PSPs $u_j(r_2, t)$ is also called a "voltage-based model" (see Fig. 3.1), in acknowledgement of the fact that, irrespective of the incoming PSPs $u_q(r_1, t - \Delta(r_1, r_2)/v)$ and $p_j(r_1, t - \Delta(r_1, r_2)/v)$, the averaged PSP $u_j(r_2, t)$ of an ensemble j always has the same shape and only differ in sign and amplitude depending on type of projection (i.e., inhibitory or excitatory) and projection strength (i.e., average number of synapses) [170]. However, neglecting the axonal arborization $\lim_{r_1 \rightarrow r_2} g_j(r_1, r_2) = \delta(r_2 - r_1)$ (see Eq. (3.5)) and the corresponding time delay $\lim_{r_1 \rightarrow r_2} \Delta_{u_j}(r_1, r_2)/v = 0$ reduces the potential-to-rate conversion (3.9) to

$$D_j \left(\frac{\partial}{\partial t} \right) m_j(r_2, t) = S_j \left(p_j(r_2, t) + \sum_{q \in J} u_q(r_2, t) \right). \quad (3.12)$$

Another version of the system of (3.8) and (3.9) in combination with respect to the mean firing rate $m_j(r_2, t)$ comprising the rate-to-potential conversion (3.8) together with the potential-to-rate conversion (3.12) is "activity-based model", meaning (see Fig. 3.1) that the input $m_j(r_1, t - \Delta_{m_j}(r_1, r_2)/v)$ governs the shapes of the PSPs $u_j(r_2, t)$ [170]. In contrast to the voltage-based model (3.11), the nonlinear transfer function S_j (a.2) separates both conversions (3.8) and (3.12). The rate-to-potential conversion (3.8) can only be inserted into the potential-to-rate conversion (3.12) if the transfer function S_j is assumed to be linear and the temporal dendritic differential operator C_j uniform for all classes of ensembles or connection $j \in J$. At all events, the system of (3.8) and (3.12) represents a closed form, although without such assumptions as the linearization of the transfer function.

The formulation for modeling PSP and mean firing rate dynamics (i.e., voltage-based (3.11) and activity-based model (3.8) and (3.12)) comprises an unspecified number of neural ensemble classes j and the temporal low-pass filter effects of the membrane when potentials propagate through axonal or dendritic tree (see Consideration (a.3)) by introducing the temporal differentiation operators C_j and D_j into the conversion operators (3.6) and (3.7). The formulation here developed also takes into account positive finite velocity distribution functions l_{u_j} and l_{m_j} , which determine the propagation delays over distances Δ_{u_j} and Δ_{m_j} . It can thus be applied to the majority of neural field models as well as to point-like-models.

Table 3.1. Activity-based models.

Study	Functions						
	(n_u, n_m)	$f_j(r)$	$g_j(r)$	$l_{u_j}(v)$	$l_{m_j}(v)$	c_j	$S_j(u)$
<i>Cortical Models</i>							
Robinson et al. [20, 162, 167]	$(2, 2^b)$	$\delta(\Delta r)$	\exp^b	1	$\delta(v - v_0)^b$	Fixed	Sigmoid
Rennie et al. [211, 212]; Wright et al. [213, 214]	$(2, 2^b)$	$\delta(\Delta r)$	\exp^b	1	$\delta(v - v_0)^b$	1 st -order	Sigmoid
Wilson and Cowan [141]	$(1, 1)$	$\delta(\Delta r)$	$\delta(\Delta r)$	1	1	Fixed	Sigmoid ^a
Wilson and Cowan [142]	$(1, 1)$	\exp	$\delta(\Delta r)$	1	$\delta(v - v_0)$	Fixed	Sigmoid ^a
<i>Thalamocortical Models</i>							
Robinson et al. [162]	$(2, 2^b)$	$\delta(\Delta r)^b$	\exp^b	1	$\delta(v - v_0)$	Fixed	Sigmoid
Rennie et al. [163]; Robinson et al. [215]	$(2, 2^b)$	$\delta(\Delta r)$	\exp^b	1	$\delta(v - v_0)^b$	Fixed	Sigmoid
Robinson et al. [168]; Breakspear et al. [169]	$(2, 2^b)$	$\delta(\Delta r)$	1	1	$\delta(v - v_0)^b$	Fixed	Sigmoid

^a $S_j(0) = 0$.

^b Functions are summarized to a partial differential operator.

3.1.3 Model Equivalence

The two Tables 3.1 and 3.2 below are a list of voltage-based and activity based models, aspects of their equivalence to the Eqs. (3.8),(3.11) and (3.12). They are presented at this stage to make the explanation which now follows easier to absorb.

The Eqs. (3.8),(3.11) and (3.12) presented in Section 3.1.2 correspond to the Jirsa and Haken model [153,154], if fixed propagation velocities $v_0 : l_{u_j}(v) = l_{m_j}(v) = \delta(v - v_0)$ (i.e., fixed delays) are considered and only the spatial dynamics of excitatory and inhibitory ensembles ($j : j \in J$ with $J = \{e, i\}$) are focussed on. In that model, the time constants of the axonal and dendritic membranes are therefore assumed to be much smaller than the effects originating from thalamocortical or corticocortical pathways such as the temporal low-pass filter effects of axons and dendrites (– this is addressed by Consideration (a3)). Both temporal differential operators C_j and D_j (see Eqs. (3.6) and (3.7)) can thus be neglected $C_j = D_j = 1$ which means that the impulse-response functions h_j and k_j are Dirac delta functions (i.e., $h_j(t) = k_j(t) = \delta(t)$) so that the conversions (3.3) and (3.4) become $\int ds \delta(t - s) \mathcal{Y}(r_1, s - \Delta(r_1, r_2)) = \mathcal{Y}(r_1, t - \Delta(r_1, r_2))$ with $\mathcal{Y}(r_1, t) = \{m_j(r_1, t), S_j(p_j(r_1, t) + \sum_{q \in J} u_q(r_1, t))\}$. Wilson and Cowan model [141] and the extension thereof [142] are compatible with the activity-based model (Eqs. (3.8) and (3.12)) for considering excitatory and inhibitory ensembles with first-order dendritic kinetics and propagation delays but without axonal kinetics $D_j = 1$. The extended Wilson and Cowan model [142] additionally considers an exponential spatial distribution function $f_j(r_1, r_2) = f_j(r_2 - r_1)$ indicating a homogeneous field which depends only on the distance $\Delta(r_1, r_2) = |r_2 - r_1|$ with $r = r_2 - r_1$ (i.e., translationally symmetrical with respect to the spatial domain Ω). The Eqs. (3.8) and (3.9) also correspond to the homogeneous Robinson model [20,167,216] for the consideration of excitatory and inhibitory ensembles with second-order kinetics of axons as well as dendrites, and spatial distribution

functions which are exponential for the axons $g_j(r)$ with fixed propagation velocities $v_0 : l_{u_j}(v) = \delta(v - v_0)$ and which are neglected for the dendrites. Robinson and colleagues combined the axonal spatial and temporal kinetics to a second-order partial differential equation D_j that is compatible with the activity-based model ((3.8) and (3.12)). The Robinson model was extended, building thalamocortical models [162, 163, 168, 169, 215] and a cortical model using first-order kinetics for the scaling factor o_j describing the synaptic kinetics [211–214]. Similarly, Liley [126, 217] developed a voltage-based cortical model by using second-order synaptic kinetics o_j , but first-order dendritic kinetics C_j . The voltage-based model (3.11) corresponds to the Nunez model [57] in respect of excitatory and inhibitory ensembles with propagation delays and an exponential spatial translationally symmetric distribution function $g_e(r)$ for the excitatory neural ensemble, neglectable spatial distribution $g_i(r)$ and delays for the inhibitory ensemble, and without dendritic and axonal kinetics $C_j = D_j = 1$. Lopes da Silva and colleagues [55] built a model of the thalamus that corresponds to the voltage-based Eq. (3.11) in respect of two ensembles (i.e., excitatory and inhibitory ensemble) with second-order dendritic kinetics and without spatial distributions and delays. Zetterberg and colleagues extended the Lopes da Silva thalamic model by considering three ensembles (i.e., two excitatory and one inhibitory ensemble) in the description of a cortical area [58], which was picked up later by Jansen and colleagues for describing event-related potentials [53, 54]. Furthermore, the Lopes da Silva model was also extended by van Rotterdam and colleagues [185] by using exponential spatial distribution functions $g_e(r)$ and $g_i(r)$. The Amari mean-field model [152] is compatible with the voltage-based model (3.11) for the consideration of excitatory and inhibitory ensembles with exponential spatial distribution functions $g_e(r)$ and $g_i(r)$ of identical first-order dendritic kinetics $C_e = C_i$ and without delays and axonal kinetics $D_j = 1$. Atay and Hutt [157, 160] took the Nunez model with second-order dendritic kinetics and extended it by

a gamma velocity distribution function l_{u_j} [158, 159]. However, in the literature these models have been treated with different choices of operators, for instance, C_j and D_j . An overview of the voltage-based and activity-based models that are listed in this section and their equivalence to the Eqs. (3.8), (3.11) and (3.12) presented in Section 3.1.2 is given in Tables 3.1 and 3.2.

Table 3.2. Voltage-based models.

Study	Functions						$S_j(x)$
	(n_u, n_m)	$f_j(r)$	$g_j(r)$	$l_{x_j}(v)$	$l_{z_j}(v)$	c_j	
<i>Cortical Model</i>							
Nunez [57]	(1, 1)	$\delta(\Delta r)$	$g_e : \exp^d$	$\delta(v - v_0)$	1	Fixed	Linear
Amari [152]	(1 ^c , 1)	$\delta(\Delta r)$	exp	1	1	Fixed	Step
Zetterberg et al. [58]	(2, 1)	$\delta(\Delta r)$	$\delta(\Delta r)$	1	1	Fixed	Sigmoid
van Rotterdam et al. [185]	(2, 1)	$\delta(\Delta r)$	exp	1	1	Fixed	Linear
Jirsa and Haken [153, 154]	(1, 1)	$\delta(\Delta r)$	$g_e : \exp^d$	$\delta(v - v_0)$	1	Fixed	Sigmoid ^{a,e}
Liley et al. [126, 217]	(1, 2 ^b)	$\delta(\Delta r)$	exp ^b	1	$\delta(v - v_0)^b$	2 nd -order	Sigmoid
Atay and Hutt [157]	(2, 1)	$\delta(\Delta r)$	exp	$\delta(v - v_0)$	1	Fixed	Sigmoid
Hutt and Atay [160]	(2 ^c , 1)	$\delta(\Delta r)$	bi-exp	$\delta(v - v_0)$	1	Fixed	Sigmoid
Atay and Hutt [158, 159]	(2 ^c , 1)	$\delta(\Delta r)$	exp	$\Gamma(v - v_0)$	1	Fixed	Sigmoid
<i>Thalamic Model</i>							
Lopes da Silva et al. [55]	(2, 1)	$\delta(\Delta r)$	$\delta(\Delta r)$	1	1	Fixed	Linear

^c $L_e = L_i$.^d $g_i = \delta(\Delta r)$.^e Approximated by using a 3rd-order Taylor series expansion.

3.1.4 Normalization

In order to treat a system analytically or numerically it is often convenient to normalize time, space and velocity and this can be done for the Eqs. (3.1) to (3.4). For example, if τ , r_c , u_c , m_c and v_c are the characteristic time, length, mean membrane potential, mean firing rate and propagation velocity of the system, then one can define $\kappa = t/\tau$, $\bar{r} = r/r_c$, $x_j(\bar{r}, \kappa) = u_j(\bar{r}_c \bar{r}/\tau\kappa)/u_c$, $x_{jT}(\bar{r}, \kappa) = p_j(r_c \bar{r}, \tau\kappa)/u_c$, $z_j(\bar{r}, \kappa) = m_j(r_c \bar{r}, \tau\kappa)/m_c$, giving $\bar{C}_j(\partial/\partial\kappa) = \tau^{n_u} C_j(\tau^{-1}\partial/\partial\kappa)$, $\bar{D}_j(\partial/\partial\kappa) = \tau^{n_m} D_j(\tau^{-1}\partial/\partial\kappa)$, as well as, $\bar{f}_j(\bar{r}_1, \bar{r}_2) = f_j(r_c \bar{r}_1, r_c \bar{r}_2)$, $\bar{g}_j(\bar{r}_1, \bar{r}_2) = g_j(r_c \bar{r}_1, r_c \bar{r}_2)$, $\bar{v} = \tau v/r_c$, $\bar{l}_{x_j}(\bar{v}) = l_{u_j}(v_c \bar{v})$ and $\bar{l}_{z_j}(\bar{v}) = l_{m_j}(v_c \bar{v})$ so that Eqs. (3.8) and (3.9) become

$$\begin{aligned} \bar{C}_j \left(\frac{\partial}{\partial \kappa} \right) x_j(\bar{r}_2, \kappa) &= o_j \frac{m_c r_c v_c \tau^{n_u}}{u_c} \int_{\Omega} d\bar{r}_1 \bar{f}_j(\bar{r}_1, \bar{r}_2) \\ &\quad \times \int_{\Gamma} d\bar{v} \bar{l}_{z_j}(\bar{v}) z_j(\bar{r}_1, \kappa - \Delta_{z_j}(\bar{r}_1, \bar{r}_2)/\bar{v}), \end{aligned} \quad (3.13)$$

$$\begin{aligned} \bar{D}_j \left(\frac{\partial}{\partial \kappa} \right) z_j(\bar{r}_2, \kappa) &= \frac{m_c r_c v_c \tau^{n_u}}{u_c} \int_{\Omega} d\bar{r}_1 \bar{g}_j(\bar{r}_1, \bar{r}_2) \int_{\Gamma} d\bar{v} \bar{l}_{x_j}(\bar{v}) \\ &\quad \times S_j \left(x_{jT}(\bar{r}_1, \kappa - \Delta_{x_j}(\bar{r}_1, \bar{r}_2)/\bar{v}) \right. \\ &\quad \left. + \sum_{q \in J} x_q(\bar{r}_1, \kappa - \Delta_{x_q}(\bar{r}_1, \bar{r}_2)/\bar{v}) \right), \end{aligned} \quad (3.14)$$

which has the same form as Eqs. (3.8) and (3.9).

3.2 Point-Like Voltage-Based Model

Using a point-like voltage-based NMM (3.11) to describe a cortical area according to Zetterberg et al. [58] and Jansen et al. [53, 54], and following the normalized formula (i. e., Eqs. (3.13) and (3.14)) of the voltage-based model, the spatial scale $\bar{r}_1 = \bar{r}_2$ can be neglected and the distribution function $\bar{g}_j(\bar{r}_1, \bar{r}_2)$ can be set to δ -like $\bar{g}_j(\bar{r}_1, \bar{r}_2) = \delta(\bar{r}_2 - \bar{r}_1)$.

Because of the short distances between the neural ensembles $j \in J$ in a cortical area and fast propagations due to myelinated axons all propagation delays are assumed to be zero $\lim_{\bar{r}_1 \rightarrow \bar{r}_2} \Delta_{z_j}(\bar{r}_1, \bar{r}_2) / \bar{v} = 0$ and thus the velocity distribution function \bar{l}_{x_j} can also be neglected $\bar{l}_{x_j} = 1$. In the spatially distributed model (3.13) to (3.14) the projection of a neural ensemble j onto another is coded on the basis of different locations \bar{r}_1 and \bar{r}_2 . Due to the loss of the spatial scale a projecting neural ensemble is indexed by $a : a \in J$ and the target ensemble is now indexed by $b : b \in J$ so that $j = ba$ in Eq. (3.11)

$$\bar{L}_{ba} \left(\frac{d}{d\kappa} \right) x_{ba}(\kappa) = \frac{o_{ba} m_c \tau^n}{u_c} S_a \left(x_{aT}(\kappa) + \sum_{q \in J} x_{aq}(\kappa) \right), \quad (3.15)$$

The linear scaling factor o_{ba} is proportional to the average number of synaptic contacts established between neural ensembles a and b .

3.2.1 Potential-to-Rate Transfer Function

For the transfer function $S_a(x_a)$ that converts the normalized mean PSP $x_a = x_{aT} + \sum_{q \in J} x_{aq}$ to the normalized mean firing rate (i.e., at the axon hillock), with $a \in J$, is taken to have a differentiable and steadily increasing sigmoidal shape

$$S_a(x_a) = \frac{1}{1 + \gamma_a \exp(-x_a)}, \quad (3.16)$$

where γ_a represents the distribution of firing thresholds or the variation of the dendritic tree of neurons within a NM. The maximum slope of the sigmoid function is $1/4$ at the point of inflection $(x_I, z_I) = (\log(\gamma_a), 1/2)$. The shape of the sigmoid function is thus constant but the conversion is weighted by the characteristic mean firing rate m_c and the characteristic PSP u_c . Consequently, a change in these characteristic constants can be interpreted as a change of the sigmoid function in terms of the slope $(\partial m_a / \partial u_a = \partial z_a / \partial x_a \times m_c / u_c)$. For detailed

properties of the sigmoid function (3.16) see Appendix A.1.

Interpretation

The sigmoid function 3.16 can be interpreted as an approximation of the superposition of many Heaviside (step) functions with Gaussian-distributed threshold values [140,141] (or see [126,160] for a more detailed treatment). A number of experimental studies have shown that the transfer of mean potentials into mean firing rates in neural ensembles is a sigmoid function [203–205].

Symmetry

The most important dynamic aspect of the biological sigmoid curve used here is the fact that for each PSP x_a the output is positive $S_a : \mathbb{R} \rightarrow \mathbb{R}^+$. This takes into account that neurons in an ensemble can fire spontaneous even if the PSP (relative to the resting potential) is zero [104], with the result that the mean firing rate of an ensemble $z_a(\kappa)$ is always positive. Other studies shift the sigmoid curve along the axes (x_a, z_a) so that the function satisfies $S_a(0) = 0$ by adding the term $-1/(1 - \gamma_a)$ to Eq. (3.16), where the function is not centrally symmetric $\gamma_a \neq 1$ [71,141,142] or centrally symmetric $\gamma_a = 1$ [66,68,70] relatively to the point of origin $(0,0)$. Such a shift leads to a stable model for the case that the extrinsic inputs $x_{aT}(\kappa)$ are zero no matter how complex the model structure (i.e., network) or the kinetics (i.e., order of differential operators) are. Another effect is that the mean firing rates z_a can be negative, which can be interpreted as mean rate below a basis firing rate. It is also worth noting that the transfer function $S_a(x_a)$ has been approximated as linear (e.g., [55,57,154]) or described by a Heaviside (step) function (e.g., [152]). Here, however, the biological sigmoid function (i.e., $S_a(0) \neq 0$) is used that maps mean PSP to positive firing rates. This transfer function represents the nonlinear element in the model of a cortical area that is mainly responsible for the diversity of dynamics and phenomena.

Effective Range of the Sigmoid Function

By definition, the PSP of any NM $x_a(\kappa)$ can reach arbitrary values due to the unconstrained extrinsic input firing rates. However, the saturation property of the potential-to-rate transfer function, that is, the sigmoid function (3.16) limits the impact of such PSP changes on the mean firing rate of the NM $z_a(\kappa)$. Due to its sigmoidal shape, the potential-to-rate operator $S_a(x_a)$ has a limited effective dynamic range $[x_I - x_{S/2}, x_I + x_{S/2}]$, with the point of inflection $(x_I, z_I) = (\log(\gamma_a), 1/2)$ (see Appendix A.1), where the sigmoid function is centrally symmetric (i. e., $S_a(x_I - x_a) = -S_a(x_I + x_a)$). The following definition is used for the half-width of the effective spectrum $x_{S/2}$. According to Eq. (3.16), the normalized maximum slope \bar{s}_{\max} of the sigmoid function, and hence the maximum influence of the PSP-changes on the output mean firing rate occurs symmetrically around the point of inflection x_I

$$\begin{aligned}\bar{s}_{\max} &= \left. \frac{\partial}{\partial x_a} S(x_a) \right|_{x_a=x_I} \\ &= 1/4.\end{aligned}\tag{3.17}$$

The effective range (around the inflection point (x_I, z_I)) is taken to be the PSP-value for which the slope of the function has dropped to $\mu \bar{s}_{\max}$. The properties of the sigmoid function mean that $x_{S/2}(\mu) = 2 \tanh^{-1}(\sqrt{1-\mu})$ (see Appendix A.1 for details). Choosing a 1%-criterion for the maximum slope s_{\max} with $\mu = 1 \times 10^{-2}$ gives $x_{S/2} = 5.986$ for standard parameters of the sigmoid function [54]. If the PSP temporarily falls or rises beyond these limits, there is no further significant change in the firing rate with respect to the μ -criterion.

3.2.2 Temporal Differential Operator

For the dendritic differential operator in Eq. (3.15) second-order kinetics are considered, that is, $n = 2$. The corresponding second-order normalized kernel $\bar{h}_{ba}(\kappa)$ in the rate-to-potential conversion (3.3), that

is, the alpha function first proposed by Rall [108,141,142,202,208], can be interpreted as the characteristic PSP elicited by a single incoming spike that is assumed to be a Dirac's delta function (i.e., $\bar{h}_{ba}(\kappa)$ is an impulse response function). This alpha function has been found to adequately describe the synaptic response of a neural ensemble [49,208] (see also [53], and the references therein)

$$\bar{h}_{ba}(\kappa) = \begin{cases} \beta_{ba}^2 \kappa \exp(-\beta_{ba} \kappa) & \text{if } \kappa \geq 0 \\ 0 & \text{if } \kappa = 0 \end{cases} \quad (3.18)$$

where the factor β_{ba} is the intrinsic temporal ratio of a characteristic time constant τ to the specific dendritic time constant τ_{ba} with $\beta_{ba} = \tau/\tau_{ba}$. The dendritic time constant τ_{ba} constitutes combined representation of passive dendritic cable delays and neurotransmitter kinetics, predominantly corresponding to fast synaptic activity (glutamate AMPA receptors^f and GABA_A receptors^g) [126]. This approach relies on some simplifying assumptions [170]. The first assumption is that the width of the spikes is negligible (e.g., it can be modeled as a Dirac delta function). The second assumption is that the effects of different spikes add up linearly (summator in Fig. 4.1), which ignores any reciprocal influences between synapses and active dendritic behavior. In the history of neuronal modeling a biexponential function has been used for fitting the impulse-response function in experimental data [49,219]. The biexponential kernel is, effectively, to the well-studied alpha function (3.18) if the area under both functions is normalized to unity and the dendritic rise time and fall time are equal (see Appendix A.2). Here, the area under the alpha function (3.18) is normalized to unity $\int_{\kappa} d\kappa \bar{h}_{ba}(\kappa) = 1$. However, the kernel function (3.18) can

^fAlpha-Amino-3-Hydroxy-5-Methyl-4-Isoxazolepropionic Acid receptor, or in abbreviated form AMPA receptor are receiving the neurotransmitter glutamate and cause excitatory PSP [218].

^gGABA_A receptor is sensitive to gamma-aminobutyric-acid of type A, in abbreviated form GABA_A and is described in more details with the footnote about GABA in Chapter 4.

be recast as a Green's function and thus stipulates $\bar{L}_{ab}\bar{h}_{ba}(\kappa) = \delta(\kappa)$ introducing a second-order differential operator

$$\bar{L}_{ba}(\lambda) = \lambda^2 + 2\beta_{ba}\lambda + \beta_{ba}^2. \quad (3.19)$$

3.2.3 Linear System of a Lumped Neural Mass

The point-like voltage-based NMM (3.15) considering the second-order differential operator (3.19) can be expressed as two first-order linear inhomogeneous differential equations

$$\dot{x}_{ba}(\kappa) = y_{ba}(\kappa) \quad (3.20)$$

$$\dot{y}_{ba}(\kappa) = -2\beta_{ba}y_{ba}(\kappa) - \beta_{ba}^2x_{ba}, \quad (3.21)$$

$$+ \alpha_{ba}\beta_{ba}^2S_a\left(x_{aT}(\kappa) + \sum_{q \in J}x_{aq}(\kappa)\right)$$

where $\alpha_{ba} = o_{ba}m_c/u_c$ contains the linear scaling factor o_{ba} , the characteristic constants of firing rates m_c and PSPs u_c . The derivatives of $x_{ba}(\kappa)$ and $y_{ba}(\kappa)$ with respect to κ are denoted by $\dot{x}_{ba}(\kappa)$ and $\dot{y}_{ba}(\kappa)$. The first derivative of the normalized mean PSP $y_{ba}(\kappa)$ can be interpreted as the mean current flow through the membrane. The coupling factor α_{ba} describes the type of impact. A mean firing rate (i. e., input) exhibits, inhibits or does not affect the neural ensemble (i. e., $J = \{e, i\}$) if the coupling factor is positive ($\alpha_e : \alpha_{ba} > 0$), negative ($\alpha_i : \alpha_{ba} < 0$), or zero ($\alpha = 0$) respectively.

In Chapter 4 the voltage-based model of a cortical area will be developed based on the mathematics presented in this section. Finally, the linear system of a lumped NM describes the normalized mean PSP $x_{ba}(\kappa)$ perturbed by the extrinsic caused PSP $x_{aT}(\kappa)$ and by the intrinsic caused PSP $\sum_{q \in J}x_{aq}(\kappa)$ under the coupling factor α_{ba} , the sigmoid parameter γ_a and the dendritic time constant τ_{ba} .

Table 3.3. Jansen and Rit parameters in physical units [54] and normalized.

Transfer	Couplings	Characteristics		
		Time	Potential	Rate
<i>Jansen and Rit</i>				
$u_0 = 6 \text{ mV}$	$H_e = 3.25 \text{ mV}$	$\tau_e = 10 \text{ ms}$	$r = 0.56 / \text{mV}$	$2e_0 = 5 / \text{s}$
	$H_i = -22 \text{ mV}$	$\tau_i = 20 \text{ ms}$		
	$c_{13} = 135$			
	$c_{23} = c_{13}/4$			
	$c_{31} = 4 c_{13}/5$			
	$c_{32} = c_{13}/4$			
<i>Normalized</i>				
$\gamma = 28.79$	$\alpha_{13} = 12.285$	$\beta = 1/2$	—	—
	$\alpha_{23} = \alpha_{13}/4$	$(\tau = \tau_e)$		
	$\alpha_{31} = 4 \alpha_{13}/5$			
	$\alpha_{32} = -11 \alpha_{13}/13$			

3.2.4 Equivalence – Jansen’s Configuration

In the previous Section, 3.2, the point-like voltage-based NMM was introduced in a normalized form, that is, all variables and parameters are normalized with respect to a set of characteristic constants (see Section 3.1.4 and Table 3.3). The basic Eqs. (3.16), (3.20) and (3.21) of the model yield a set of compact parameters comprising several experimentally quantifiable parameters described, for example, in Freeman’s studies [49, 52, 220]. An analysis of the mathematical description of NMMs that incorporate such experimentally quantities (e.g., [54]) shows clearly that several parameters such as the synaptic gains and the mean numbers of synaptic contacts affect the system in the same way. They are, therefore, lumped together here. That the system variables and parameters match these which are obtained experimentally is demonstrated using the example of Jansen’s definitions [54] (see Table 3.3). The normalized system variables, that is, the normalized mean membrane potential $x_{ba}(\kappa)$ and normalized mean firing rate $z_a(\kappa)$ cor-

respond to the variables in the Jansen and Rit model as follows

$$x_{ba}(\kappa) = r u_{ba}(\kappa\tau) \quad (3.22)$$

$$z_a(\kappa) = m_a(\kappa\tau)/(2e_0). \quad (3.23)$$

The system parameters, which are the coupling factor α_{ba} , the intrinsic temporal ratio β_{ba} and the sigmoid parameter γ_a , correspond to Jansen's parameters as follows

$$\alpha_{ba} = 2e_0 r c_{ba} \rho_{e,i} \quad (3.24)$$

$$\gamma_a = \exp(r u_0) \quad (3.25)$$

$$\beta_{ba} = \tau/\tau_{e,i}, \quad (3.26)$$

where u_0 is the PSP for which a 50% mean firing rate e_0 is achieved. In the original Jansen model a dendritic alpha kernel is used according to van Rotterdam and colleagues [185]. In this case, the area ρ under the alpha function (3.18) is normalized to the product of maximum amplitude $H_{e,i}$ of the excitatory and inhibitory PSP and the dendritic time constant $\tau_{e,i}$, that is, $\rho_{e,i} = H_{e,i} \tau_{e,i}$ in (3.24).

Thus, the linear scaling factor α_{ba} is equal to a connectivity constant c_{ba} multiplied by the area $\rho_{e,i}$ under van Rotterdam's alpha kernel, used in Jansen's model $\alpha_{ba} = c_{ba} \rho_{e,i}$. The characteristic mean membrane potential u_c is equal to the slope of the sigmoid function in Jansen's parametrization with $u_c = 1/r$ and the characteristic mean firing rate m_c is equal to the maximum mean firing rate of a neural ensemble in Jansen's model with $m_c = 2e_0$.

3.3 Methods

Several analytical and numerical methods were applied to the analysis of the modified Zetterberg-Jansen model and the experimental data. The major part of the analyses, in particular, the bifurcation analysis of

the system, was done with the MATLABTM numerical computing environment [221] employing the standard algorithms implemented therein. The remaining algorithms were written in Fortran-77 and Fortran-90 programming language. This section lists and briefly describes the setups of the methods used for this research. In the case of non-standard MATLABTM functions, the specific algorithms are explained.

3.3.1 Bifurcation Diagrams

Bifurcations indicate qualitative changes in the dynamics of a system as a function of a set of varying parameters θ . Hence, a bifurcation diagram of a system delivers a compact representation of its dynamics in the parameter space, which is divided into domains, each characterized by a specific dynamic regime (e. g., a single stable LC and/ or an unstable focus). Each qualitative regime can be represented by a phase portrait. It consists of fixed points and their stabilities, the local and/or global bifurcations, the branches of LCs, and the phase portraits corresponding to each qualitative regime (see, for example [222]). The bifurcation method applied here is discussed in more detail in Section 5.1.2. In Appendix A.4 the analysis is demonstrated using two examples of single NMs.

In the case of the constantly forced modified Zetterberg-Jansen model used here, the fixed points can be algebraically determined in the state space against the varying parameters. The kind of stability is then characterized by linearizing the system and evaluating the eigenvalues of the Jacobian matrix at the fixed points. For this purpose the Jacobian is set up analytically. Due to the complexity of the system (14-dimensional nonlinear system; see Section 4.1) the eigenvalues of the Jacobian are calculated numerically. For this purpose, the extrinsic input on PCs is linearly sampled with 10^4 discrete points. The critical points were identified using the Nelder-Mead simplex method [223] implementation in MATLABTM (*fminsearch* function as part of the MATLABTM optimization toolbox [221]) with a tolerance of 10^{-32} (on function and output),

maximum iterations of 10^3 and function evaluations 10^3 per iteration.

The branches of LCs are numerically computed using the continuation package CL_MATCONT for MATLAB™ by Govaerts, Kuznetsov and colleagues [224–226] as function of the extrinsic input level on PCs (i. e., $u_{3T}(t)$ or respectively $x_{3T}(\kappa)$) with an initial, minimum and maximum step size of 1.82×10^{-4} (3.25×10^{-7} V for the characteristic mean membrane potential $u_c = 1.79 \times 10^{-3}$ V according to Jansen and Rit [54]), 1.82×10^{-5} (3.25×10^{-8} V) and 7.3×10^{-3} (1.3×10^{-3} V) for a maximum of 4×10^3 continuation points.

3.3.2 Time Series

For some analyses (i. e., state space analyses) or for verifying the analyses (i. e., bifurcation diagrams and their classification) time series of the system states are calculated by numerically integrating the differential equations over time using the fourth-fifth order Runge-Kutta method.

The constantly forced modified Zetterberg-Jansen model was numerically integrated using the *ode45* in MATLAB™ for verifying the compiled bifurcation diagrams (see, for example, Fig. 5.1) in terms of time series (see, for example, Fig. 5.12). For the former case, the system was integrated over $\kappa = 10^4$ in time (which equals 100 s for a characteristic time constant $\tau = \tau_c$ with $\tau_c = 10 \times 10^{-3}$ s, as suggested by Jansen and Rit [54]; see Table 3.3) with a relative tolerance of 10^{-3} . Due to the step-size control of the integration method the computed time series were non-equidistantly sampled over time. Time series were sampled linearly ($\Delta\kappa = 25/128$) for analyzing the last 2560 samples ($\kappa = 500$, that is, 5 s for the characteristic time $\tau = \tau_c$, Table 3.3).

For the example of the ordered sequences (see Fig. 5.12) the equations are integrated over $\kappa = 2 \times 10^3$ in time (which equals 20 s for the characteristic time constant $\tau = \tau_c$ in Table 3.3) with a relative tolerance of 10^{-12} . The first period of $\kappa = 800$ (8 s for the characteristic time constant $\tau = \tau_c$ in Table 3.3) is discarded because of transient behavior at the beginning due to the noise process used here and possible

displacements from a stable state (e. g., fixed point).

In the case of the periodically modified Zetterberg-Jansen model a widely used subroutine *DVERK* is applied based on the fourth-fifth order Runge-Kutta formulas written in Fortran [227]. The differential equations over $\kappa = 30 \times 10^3$ in time (which equals 5 min are computed for a characteristic time constant $\tau = \tau_e = 10 \times 10^{-3}$ s, according to Jansen and Rit [54]; see Table 3.3) with a relative tolerance of 10^{-11} , and then linearly sampled ($\Delta\kappa = 10^{-2}$) for further analysis.

A general problem with differential equations is the so-called initial value problem. This is solved with the compiled bifurcation diagrams that indicates the conditions for the existing states. In most cases the evolution is initialized at a stable fixed point unless otherwise specified.

3.3.3 Characteristic Lyapunov Spectra

The *characteristic Lyapunov spectrum* gives a quantitative measure of the sensitivity of the states of the system towards the initial conditions, or, more precisely, the average rate of divergence or convergence of two neighboring trajectories in the state space (see, for example [228]). It quantifies the exponential rates of divergence λ of initially infinitesimally displaced trajectories V_0 in the i -dimensional state space

$$|V(\kappa)| = |V_0| \exp(\kappa \lambda) \quad (3.27)$$

with $V(\kappa)$ being the displacement at time κ . The characteristic Lyapunov spectrum can be estimated using the formula

$$\lambda = \lim_{\kappa \rightarrow \infty} \frac{1}{\kappa} \ln \frac{|V(\kappa)|}{|V_0|}. \quad (3.28)$$

The spectrum λ consists of a set of Lyapunov characteristic exponents, the number of which is equal to the dimension of the state space i (number of states) $\lambda_1 > \lambda_2 \dots > \lambda_i$. The growth rate of the i -dimensional manifold (ellipsoid) in state space is the sum of the Lyapunov

exponents $\sum_1^i \lambda_i$. The mean prediction time is $1 / \left(\sum_1^i \lambda_i \right)$.

The Lyapunov spectrum of which the formulae have not been expounded characterizes the behavior of a system. A system is dissipative or conservative, if and only if the sum of all Lyapunov characteristic exponents $\sum_i \lambda_i$ is negative or zero. Conservative means that the momentum (derivative of states) is conserved, that is, not dissipated (reduced) during evolution, and a particular set (domain) of states and its derivatives remains. Dissipative means that the momentum (derivative of states) is continually decreasing with displacement during evolution (energy is lost with continued evolution) until the magnitude of the momentum reaches zero (kinetic energy reaches zero). For instance, a Hamiltonian system is indicated as a conservative system where pairs of Lyapunov characteristic exponents exist $\lambda_i = -\lambda_j$. A positive Lyapunov characteristic exponent $\lambda_i > 0$ reflects unstable direction of stretching and folding and indicates chaos in the system. A zero Lyapunov characteristic exponent $\lambda_i = 0$ reflects a conserved neutrally stable direction (i.e., Lyapunov stable). A negative Lyapunov characteristic exponent $\lambda_i < 0$ reflects a dissipative direction of attraction, for instance, to a stable fixed point or a stable LC (i.e., asymptotically Lyapunov stable).

Turning to the periodically forced modified Zetterberg-Jansen model, the characteristic Lyapunov spectra are directly computed from the differential equations, using the Fortran algorithm by Chen and colleagues [229], integrated for $\kappa = 1\,073\,742.00$ (≈ 3 h for a characteristic time constant $\tau = \tau_c$ with $\tau_c = 10 \times 10^{-3}$ s, as in Jansen and Rit [54]; see Table 3.3) using a constant sample interval $\Delta\kappa = 10^{-3}$. In the Chen algorithm, a constant time-step fourth-order Adams-Bashforth integration method and a QR-reorthogonalization is used in order to preserve the orthogonality, especially for higher-dimensional systems. The actual computing of the whole characteristic Lyapunov spectra took place at Ilmenau University of Technology, Ilmenau, on a parallel cluster in the advanced computing unit at the Computer Center there.

The largest characteristic Lyapunov exponents of the photic driving experiment (see Section 3.4) are estimated from the time series using the approach of Wolf and colleagues [230] written in Fortran-77 programming language. An embedding dimension of 16, a time delay of nine ($\approx 50 \times 10^{-3}$ s for the characteristic time $\tau = \tau_c$, Table 3.3) and an evolving time of five ($\approx 25 \times 10^{-3}$ s for the characteristic time $\tau = \tau_c$, Table 3.3) is used for the investigation of flicker stimulations.

3.3.4 Kaplan-Yorke Dimension

The *Kaplan-Yorke dimension* gives an estimate of the upper bound for the information dimension of the system, which quantifies the complexity of the geometry of the attractor [231]. It is given by

$$D_{KY} = k + \frac{\sum_{i=1}^k \lambda_i}{|\lambda_{k+1}|}, \quad (3.29)$$

based on the characteristic Lyapunov spectra, consisting of all Lyapunov exponents $\lambda_1 > \lambda_2 > \dots > \lambda_i$ with respect to an i -dimensional system in which k is chosen such that $\sum_{i=1}^k \lambda_i \geq 0$, and $\sum_{i=1}^{k+1} \lambda_i < 0$. The Kaplan-Yorke dimension is algebraically calculated in MATLABTM.

3.3.5 Poincaré Map

A *Poincaré map* P considers the intersections of an evolving trajectory in the d -dimensional state space with a hyperplane of dimension $d - 1$, where only those intersections count that traverse the hyperplane from the same side [228]. Such a map (also called a recurrent map) turns a continuous dynamical system into a discrete one. With an adequately chosen hyperplane, the qualitative behavior of the system can be preserved and the resulting discrete series of intersection points allows a characterization of near periodic solutions in dynamic systems. The dynamics can be analyzed on the basis of the structure of the Poincaré map P (e.g., its Jacobian and the eigenvalues thereof). For instance,

if a periodic orbit traverses a hyperplane perpendicular to its surface in the d -dimensional state space the two-dimensional manifold of the orbit reduces to a periodic intersecting point in the hyperplane.

However, the determination of the hyperplane is a delicate problem for which no general approach is to be found [228]. In the study of the periodically forced modified Zetterberg-Jansen model a suitable hyperplane was chosen, traversing the LC of the unperturbed system and its unstable fixed point.

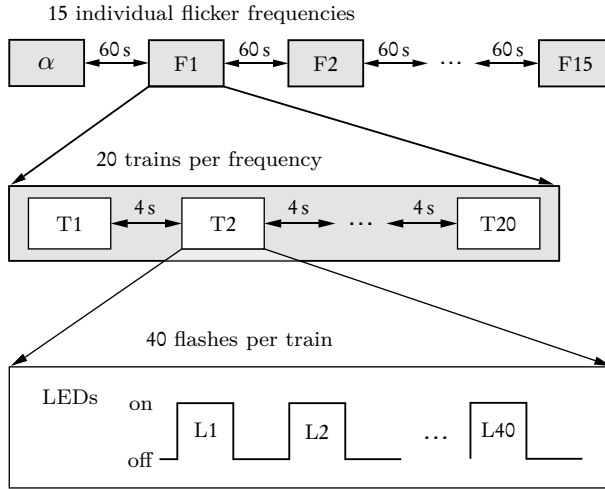


Fig. 3.2. Experimental design of the flicker stimulation study. The light-emitting diodes (LEDs) were powered for half of each period. The raise and decay time for the LEDs was measured to be 100 μ s.

3.4 Experimental Data

The experimental data on which the periodic forced model was tested are those in [82]. Ten healthy probands (22 to 40 years of age, five male

and five female) were stimulated by an intermittent flickering light, while the EEG (32 channels, enhanced 10-20 system with a 10-10 system over the occipital region, Compumedics Neuroscan, El Paso, USA) was recorded. The sampling for the EEG was 1000 Hz and hardware-filtered between 0.1 Hz and 300 Hz. An initial resting condition of 60 s was recorded to define the individual alpha rhythm of each proband. After this period, flicker stimulations were conducted for 15 fixed frequencies with an alpha ratio (flicker frequency/individual alpha) ranging from 0.4 to 1.6 in each proband (randomized order of presentation). The flicker stimuli were generated by two LEDs outside the measurement chamber and were delivered via optical fibers to about 9×10^{-2} m in front of the closed eyes of the subjects in order to ensure relatively stable luminance over subjects. Each stimulation frequency was presented in a sequence of 20 trains. A single train contained 40 flashes and was followed by a resting period (4 s). The complete experimental design is given in Fig. 3.2. Data were filtered and down-sampled to 200 Hz. For each proband, periods of 62.5 s ($n = 12500$ data points) were analyzed for the 15 flicker frequencies presented (the shortest available data length of the individual flicker blocks F1 to F15 is 62.5 s over all probands investigated).

4 Zetterberg-Jansen Model

*If you try and take a cat apart to see how it works,
the first thing you have on your hands is a non-working cat.*

Douglas Adams, 1952–2001

Although local neuronal circuits are complex (see, for example, [145]), there is a strong tendency for local axonal collaterals of PCs in cortical layers III to VI to make synaptic contacts to GABAergic^a interneurons (i.e., IINs), which themselves have only short axonal processes and therefore make contact with local cells, such as PCs. This forms intralaminar (PCs in layers III to VI) as well as interlaminar (PCs in layers III and IV) inhibitory feedback loops. Such feedback loops may also be excitatory (i.e., principally glutamatergic), mediated either by (smaller) PCs or by EINs, mostly so-called spiny stellate cells in layer IV [102, 145]. Therefore, the membrane potential of the PCs can be modeled as a weighted sum of the effects of extrinsic inputs to the cortical area and feedback influences from interneurons.

^aGABAergic neurons release gamma-aminobutyric-acid, or in abbreviated form GABA: the principal inhibitory neurotransmitter in the cerebral cortex that plays a potential role in regulating neuronal excitability [232, 233] where a imbalance may result in pathological states such as epilepsy [234] or schizophrenia [235]. The corresponding receptors can be structurally classified between GABA_A and GABA_B receptors (e.g., [236, 237]). The fast and slow kinetics of GABA_A receptors are believed to underlie gamma and delta rhythms, for instance, in hippocampal pyramidal cells (e.g., [238]).

When the local neuronal circuit is reduced to a parsimonious model, the following points are to be regarded as important: (i) there are PCs sending axons to other brain areas which, due to their long apical dendrites arranged in parallel, give rise to measurable EEG and MEG [27], (ii) collaterals from these PCs contact excitatory and inhibitory cells with local axonal arbors (interneurons), and (iii) it is highly probable that these interneurons will, in turn, make synaptic contacts with the PCs, thus forming feedback loops. In line with this, Zetterberg and colleagues [58] and later Jansen and colleagues [53, 54]^b described the cortical area as a basic element composed of three NMs: PCs, EINs and IINs, interacting through positive and negative feedback loops. In their model, extrinsic input (i.e., from other brain areas) only targets the PCs. However, since there is strong evidence that this input also targets interneurons, the model was extended accordingly by David and colleagues [66]. Its structure is illustrated in Fig. 4.1. Applying Freeman’s terminology (see Section 2.4.2) the model represents a KII structure composed of three interacting KI-sets (PCs, EINs and IINs).

Note that the feedback loops may be modeled dynamically (see, for example, [57, 153, 168, 239], see also, e. g., [76, 77] in order to consider propagation delays). However, in the modified Zetterberg-Jansen model, the connections are assumed to be local (within a single cortical area). That means only small spatial extension and transmission times are considered, describing the feedback connection by a gain constant.

The mean membrane potential of the PCs is caused by three different inputs: excitatory input from local EINs, excitatory input from other areas (referred to as extrinsic inputs), and inhibitory input from local

^bJansen and Rit [54] identified this network with a cortical column according to the findings of Mountcastle and colleagues [117]. However, because the universality of the concept of columnar organization of the cortex is controversial [120], the term cortical area is used instead. The key mechanisms of the model are unaffected by this re-interpretation.

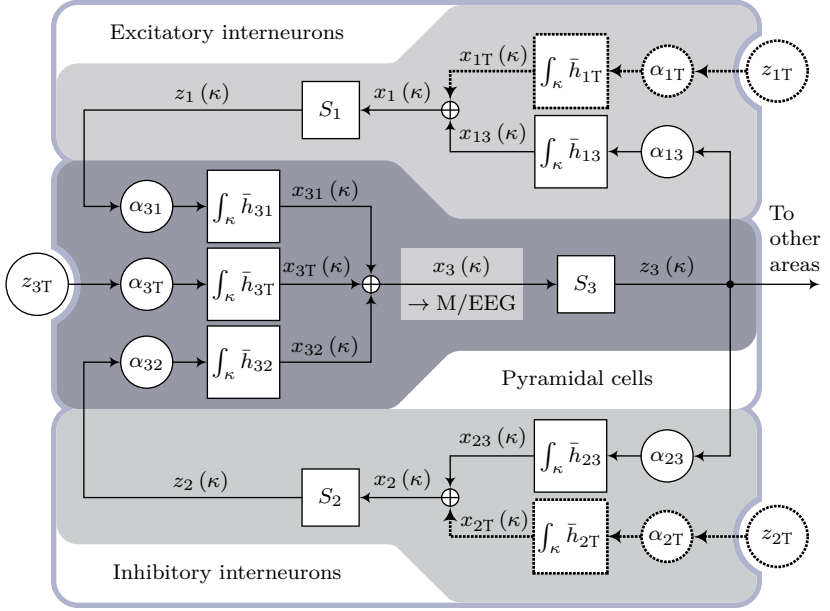


Fig. 4.1. Modified structure of the Zetterberg-Jansen model. The model consists of three NMs ($J = \{1, 2, 3\}$, where $a : a \in J$ and $b : b \in J$), representing PCs receiving positive and negative feedback via EINs and IINs. Operators (boxes) are S — the potential-to-rate operator transforming the mean PSP x_a to the average firing rate z_a at the axon hillock, $\int d\kappa \bar{h}_{ba}$ — the rate-to-potential conversion computing the mean PSP x_{ba} at the soma for a NM b by convolution of the synaptic kernel $h_{ba}(\kappa)$ (including the dendritic time constants) with the incoming mean firing rate z_a of neuron a , weighted according to the mean number of synaptic contacts α_{ba} , and \oplus — the summation operator gathering the PSPs $\sum_a x_{ba}$ rising in the dendritic tree at the soma. Parameters (circles) are α_{ba} — the coupling factor of synaptic contacts established between NM a to b and z_{aT} — the extrinsic input firing rate of the NM a , with J assuming 1 (EINs), 2 (IINs), 3 (PCs) and T (extrinsic input). Variables (describing the flows) are z_b — the mean firing rate of the NM b , and x_{ba} — the PSP of NM b due to input a . Mean PSPs of PCs $x_3(\kappa)$ mainly contribute to M/EEG. Modifications to the classical structure to the Zetterberg-Jansen model [53, 54, 58] are shown by dotted lines.

IINs, $x_3(\kappa) = x_{31}(\kappa) + x_{32}(\kappa) + x_{3T}(\kappa)$. The present NMM takes into account extrinsic input from other cortical and/or subcortical areas (e.g., from cortical areas of the other hemisphere or from thalamic nuclei) not only to the PCs (z_{3T}), but also to both types of interneurons (excitatory z_{1T} and inhibitory z_{2T}). This approach, first used by David and colleagues [66], is based on findings that interneurons also receive input from other cortical areas. For example, the spiny stellate cells (EINs) as well as GABAergic basket cells (IINs) in layer IV of primary sensory cortices receive input from the thalamus (e.g., [240–242]). This is also in line with inter-area connection schemes as postulated, for example, by Felleman and Van Essen [243]^c.

The neuronal currents underlying M/EEG generation are believed to be produced mainly by the membrane potentials of the PCs [27] as a result of the asymmetric shape of these cells (with apical dendrites) and their parallel alignment perpendicular to the cortical surface [147]. The linear output function (leadfield; see Eq. (2.1)), mapping the mean membrane potentials of the PCs to the measurements outside the brain, has to take into account a physical model of the head [70]. In this work, it is not necessary to consider leadfield modeling (Eq. (2.1)) because only a single area is studied.

4.1 System

The modified Zetterberg-Jansen model of a cortical area (see Fig. 4.1) can be described by a system of 14 nonlinear first-order differential equations using the point-like voltage based Eqs. (3.20) and (3.21) with the ensemble set $J = \{1, 2, 3\}$, where $a : a \in J$ and $b : b \in J$.

^cThe modified Zetterberg-Jansen model as analyzed here can be related to the original configuration of Jansen and Rit [54] without extrinsic inputs to the interneurons as follows. Variation in the extrinsic input levels in the extended model is equivalent to variation in the firing thresholds of the corresponding target NMs in the original model if, and only if, the extrinsic inputs are constant in time (or change slowly as compared to the time constants of the system).

PCs (3) to EINs (1)

$$\begin{aligned}\dot{x}_{13}(\kappa) &= y_{13}(\kappa) \\ \dot{y}_{13}(\kappa) &= -2\beta_{13} y_{13}(\kappa) - \beta_{13}^2 x_{13}(\kappa) \\ &\quad + \alpha_{13}\beta_{13}^2 S_3(x_{31}(\kappa) + x_{32}(\kappa) + x_{3T}(\kappa))\end{aligned}\tag{4.1}$$

PCs (3) to IINs (2)

$$\begin{aligned}\dot{x}_{23}(\kappa) &= y_{23}(\kappa) \\ \dot{y}_{23}(\kappa) &= -2\beta_{23} y_{23}(\kappa) - \beta_{23}^2 x_{23}(\kappa) \\ &\quad + \alpha_{23}\beta_{23}^2 S_3(x_{31}(\kappa) + x_{32}(\kappa) + x_{3T}(\kappa))\end{aligned}\tag{4.2}$$

EINs (1) to PCs (3)

$$\begin{aligned}\dot{x}_{31}(\kappa) &= y_{31}(\kappa) \\ \dot{y}_{31}(\kappa) &= -2\beta_{31} y_{31}(\kappa) - \beta_{31}^2 x_{31}(\kappa) \\ &\quad + \alpha_{31}\beta_{31}^2 S_1(x_{13}(\kappa) + x_{1T}(\kappa))\end{aligned}\tag{4.3}$$

IINs (2) to PCs (3)

$$\begin{aligned}\dot{x}_{32}(\kappa) &= y_{32}(\kappa) \\ \dot{y}_{32}(\kappa) &= -2\beta_{32} y_{32}(\kappa) - \beta_{32}^2 x_{32}(\kappa) \\ &\quad + \alpha_{32}\beta_{32}^2 S_2(x_{23}(\kappa) + x_{2T}(\kappa))\end{aligned}\tag{4.4}$$

Extrinsic input (T) to EINs (1)

$$\begin{aligned}\dot{x}_{1T}(\kappa) &= y_{1T}(\kappa) \\ \dot{y}_{1T}(\kappa) &= -2\beta_{1T} y_{1T}(\kappa) - \beta_{1T}^2 x_{1T}(\kappa) + \alpha_{1T}\beta_{1T}^2 z_{1T}(\kappa)\end{aligned}\tag{4.5}$$

Extrinsic input (T) to IINs (2)

$$\begin{aligned}\dot{x}_{2T}(\kappa) &= y_{2T}(\kappa) \\ \dot{y}_{2T}(\kappa) &= -2\beta_{2T}y_{2T}(\kappa) - \beta_{2T}^2x_{2T}(\kappa) + \alpha_{2T}\beta_{2T}^2z_{2T}(\kappa)\end{aligned}\tag{4.6}$$

Extrinsic input (T) to PCs (3)

$$\begin{aligned}\dot{x}_{3T}(\kappa) &= y_{3T}(\kappa) \\ \dot{y}_{3T}(\kappa) &= -2\beta_{3T}y_{3T}(\kappa) - \beta_{3T}^2x_{3T}(\kappa) + \alpha_{3T}\beta_{3T}^2z_{3T}(\kappa)\end{aligned}\tag{4.7}$$

The intrinsic and extrinsic coupling factors α_{ba} and α_{bT} are defined as $\alpha_{ba} = o_{ba}m_c/u_c$ and $\alpha_{bT} = o_{bT}m_c/u_c$ with the subscripts $ba = \{13, 23, 31, 32\}$ (where $j = ba$) and $b = \{1, 2, 3\}$. The extrinsic inputs from other cortical and subcortical areas can be seen as deterministic and/or stochastic processes, here denoted by $x_{1T}(\kappa)$, $x_{2T}(\kappa)$ and $x_{3T}(\kappa)$ for extrinsic afferents on EINs (1), IINs (2) and PCs (3).

4.2 Extrinsic Input

The PSP of a NM b caused by NM a can be decomposed into intrinsically and extrinsically caused components (i.e., input from the same NM or different NMs in the same structure, such as a cortical area, and input from other structures, such as the thalamus or other cortical areas). While the latter is principally unrestricted in range, the former is restricted by the potential-to-rate transfer function of the presynaptic NM. Its range $[x_{ba, \min}, x_{ba, \max}]$ is $[0, \alpha_{ba}]$ for excitatory and $[\alpha_{ba}, 0]$ for inhibitory inputs according to Eqs. (3.13), (3.16) and (3.18). Hence, extrinsically caused PSPs $x_{bT}(\kappa)$ range effectively between $(x_I - x_{S/2} - x_{ba, \max})$ and $(x_I + x_{S/2} - x_{ba, \min})$. This is explained more fully in Appendix A.3. Extrinsic inputs beyond this range do not affect the dynamics, thus effective ranges for all inputs can be identified

and translated into ranges of firing rates (see Table 4.1)^d.

Table 4.1. Effective ranges of the normalized extrinsic input of the modified Zetterberg-Jansen model. Positive and negative (normalized) PSPs are due to excitatory and inhibitory inputs. By multiplying the normalized PSPs and rates by chosen characteristic potential and rate constants u_c and m_c (see, for example, Table 3.3) one obtains the physical values.

Extrinsic input on	Postsynaptic potential	Maximum firing rate	
		Excitation	Inhibition
EINs	−14.91 to 9.35	102.71	12.10
IINs	−5.7 to 9.35	102.71	4.62
PCs	12.45 to 50.93	559.63	10.11

^dNote that only positive firing rates are biologically possible. In contrast, PSPs can be negative as well as positive, and induced by inhibitory as well as excitatory extrinsic projections. Therefore, PSPs are used rather than mean firing rates to characterize extrinsic inputs.

5 Modes of a Cortical Area

To know a thing well, know its limits.

Frank Herbert, 1920–1986

In this chapter there is an analysis of how the modified Zetterberg-Jansen model responds to changes in the extrinsic inputs and the dendritic time constants. For the extrinsic input signal both constant and periodic time courses are considered (the constant in Section 5.1 and the periodic in Section 5.2). The parameters and the (effective) ranges selected for the analysis are described and justified. The selection allows the dimensionality of the general system to be reduced (Eqs. 4.1 to 4.7). Finally, the results are classified, exemplarily described and interpreted with respect to phenomena observed in M/EEG data.

5.1 Constantly Forced Model

The subject of this chapter is the modified Zetterberg-Jansen model, which is the NMM used in Bayesian inversion schemes, where the original Jansen and Rit model configuration is included as a special case: In this NMM, extrinsic input may target the two populations of interneurons [66]. Here, in Section 5.1, the focus is on the single-area version of this modified Zetterberg-Jansen model, with the question of which dynamic regimes this single-area model can experience. Included in

the investigation is the entire effective parameter space of the model, rather than just the specific parameter set proposed by Jansen and Rit [54]. The analysis produces a catalogue of dynamic regimes, which can be directly used for modeling M/EEG data and shows that the dynamics of the single-area model are richer and probably more useful for modeling purposes than previously thought. If it is the case that one can model a large class of phenomena with the single-area modified Zetterberg-Jansen model as here shown, comprehensive knowledge about single-area dynamics, as provided by the results, may therefore be valuable for the network analysis of M/EEG and electrophysiology data using such Bayesian model inversion schemes as dynamic causal modeling [50]. A systematic description of the dynamic properties of the modified Zetterberg-Jansen model as a function of its key parameters is given. One way of approaching these rich dynamics is to look at the bifurcations indicating sudden transitions in dynamic behavior and at the LC branches which have not been described before [189]. Bifurcation diagrams are used due to the compact and intuitively accessible representations of the system dynamics against varying parameters. Knowledge of this dynamic behavior is an important tool, because it tells the modeler how the system will behave qualitatively when system parameters change slowly. LC-branches are systematically classified and the associated dynamics are discussed in detail, including their conditions of changing as a function of key parameters, namely the extrinsic inputs from other cortical and subcortical areas to the three NMs, and the dendritic time constants. This bifurcation analysis yields a comprehensive catalogue of potential oscillatory regimes. A potential use of this catalogue is that the modeler can decide whether the single-area modified Zetterberg-Jansen model is sufficient to model any specific phenomenon (e. g., in M/EEG) or whether a more complex model, such as a network of brain areas, should be chosen. Moreover, the modeler can use the catalogue to select a specific parameter set that best reproduces the observed signals. In addition, the bifurcation

Table 5.1. Range of the varied system parameters: dendritic time constants for inhibitory and excitatory synaptic terminals $\tau_{e,i}$ and PSPs due to extrinsic afferent projections on EINs u_{1T} , IINs u_{2T} and PCs u_{3T} . The normalized ranges can be obtained by dividing the parameters with the characteristic constants in Table 3.3.

Param.	Range	Step size	Unit
$\tau_{e,i}$	2 to 60	2	ms
u_{1T}	-27, -22, -17, -12, -8, -4, -2, 0, 2, 4, 8, 12, 17	Discrete	mV
u_{2T}	-11, -8, -4, -2, 0, 2, 4, 8, 12, 17	Discrete	mV
u_{3T}	12.45 to 50.93	Continuous	mV

diagrams inform the modeler which slow-moving trajectories through parameter space will cross bifurcation points. This means that apparently complex M/EEG phenomena can be explicitly modeled as an ordered sequence of switches between different oscillatory regimes. In principle, this enables one to model phenomena like the progression of pathology, epileptic events (see, for example, [76–78], for thalamocortical models), pharmacological interventions, sleep stages [79], or general changes in the oscillatory regime due to contextual state changes. This approach is illustrated using some synthetic examples. The analysis in this work enables the selection of a highly constrained parameterization. Bayesian inversion (as used in dynamic causal modeling, e. g., [50, 66]) should, in principle, be able to identify the free parameters of ordered sequence models, for example, the slowly changing function needed to induce the switching behavior.

5.1.1 Parameter Space

This section explores the dynamics of the single cortical area model as a function of the five system parameters which are most relevant for the richness of the dynamics: the excitatory and inhibitory dendritic time constants (or respectively intrinsic temporal ratios) and the extrinsic

input (i. e., from other cortical and subcortical areas) to the three NMs. The choice made is justified below.

Dimension Reduction

In the form described in Eqs. (4.1) to (4.7), the system has 20 parameters^a, which is prohibitive to analysis. Jansen and Rit [54] suggest distinguishing the rate-to-potential conversion only for excitatory and inhibitory synaptic contacts, described by the kernels $\bar{h}_e(\kappa)$ and $\bar{h}_i(\kappa)$, the afferent connections originating from the PCs and EINs are exclusively excitatory (i. e., $\bar{h}_{13}(\kappa) = \bar{h}_{23}(\kappa) = \bar{h}_{31}(\kappa) = \bar{h}_e(\kappa)$). Afferents from IINs are inhibitory i. e., $\bar{h}_{23}(\kappa) = \bar{h}_i(\kappa)$). Extrinsic afferents (i. e., from other cortical or subcortical areas) could be excitatory or inhibitory (i. e., $\bar{h}_{bT}(\kappa) = \{\bar{h}_e(\kappa), \bar{h}_i(\kappa)\}$, $b = \{1, 2, 3\}$). In contrast to van Rotterdam [185], moreover, it seemed reasonable to assume that the cortical areas under the dendritic kernels (3.18) are the constant products of Jansen’s maximum amplitude of PSPs $H_{e,i}$ and dendritic time constants $\tau_{e,i}$, that is, $\rho_{e,i} = H_{e,i} \tau_{e,i}$ in Eq. (3.24). This is supported by computational modeling [206, 244]. The respective constant products for both cases $\rho_e = 32.5 \times 10^{-6} \text{ V s}$ and $\rho_i = -440 \times 10^{-6} \text{ V s}$ are derived from the original Jansen and Rit parameter set, similar to the definition used by David and Friston [48]. As shown later, these constraints on the area under $\bar{h}_{e,i}(\kappa)$ fix the equilibrium states of the system under the condition of constant extrinsic inputs to interneurons.

It should be noted that the intrinsic and extrinsic coupling factors α_{ba} and α_{bT} incorporate $\rho_{e,i}$ (see Section 3.2.3 or Section 4.1). The coupling factors for the extrinsic inputs α_{bT} simply scale linearly the extrinsic inputs $z_{bT}(\kappa)$ for $b = \{1, 2, 3\}$ and can therefore be fixed to $\alpha_{e,T}$ and $\alpha_{i,T}$ for excitatory and inhibitory input when considering a

^aThese are: the coupling factors α_{ba} , the intrinsic temporal ratios β_{ba} , with $ab = \{13, 23, 31, 32\}$; the parameters γ_b of the sigmoid function S_b (3.16); the extrinsic input levels to the three neural ensembles $z_{bT}(\kappa)$; the extrinsic temporal ratios β_{bT} and the coupling factors α_{bT} with $b = \{1, 2, 3\}$.

single cortical area with $\alpha_{e,T} = \rho_e m_c / u_c$ and $\alpha_{i,T} = \rho_i m_c / u_c$ (see Table 3.3). Following Jansen and Rit [54], the parameters of the sigmoid functions γ_b are assumed to be the same for all NMs $\gamma_b = \gamma$ and thus $S_b(x_b) = S(x_b)$ with $b = \{1, 2, 3\}$ (see Section 3.2.4 in Chapter 3). Furthermore, the characteristic time τ is chosen to be equal to the excitatory dendritic time constant $\tau = \tau_e$, so that β_{13} , β_{31} and β_{32} become unity $\beta_{13} = \beta_{31} = \beta_{32} = 1$, $\beta_{23} = \beta$ is the ratio of excitatory to inhibitory dendritic time constant $\beta = \tau / \tau_i$ and β_{bT} are either unity or β with $b = \{1, 2, 3\}$.

Of the remaining nine free parameters, five are selected for further analysis: the intrinsic temporal ratio $\beta = \tau / \tau_i$ (i. e., excitatory and inhibitory dendritic time constants $\tau_e = \tau$ and τ_i) and the extrinsic inputs levels $m_{1T}(\kappa)$, $m_{2T}(\kappa)$, and $m_{3T}(\kappa)$. The time constants (i. e., intrinsic temporal ratio β) are chosen because they are expected to exercise a major influence on the system's ability to oscillate and the frequency of these oscillations. The constant (or slowly changing, relative to the time constants of the system) extrinsic input levels to the three NMs are of major importance if the system is part of a larger network of cortical areas. They depend upon connections between brain areas, which have been used in Bayesian inversion schemes [66].

Here, the parameter γ of the sigmoid function (3.16) and the intrinsic linear scaling factors are neglected. Variations in the extrinsic input levels, which are analyzed in Section 5.1.2, are equivalent to variations in γ of the sigmoid functions, and to variations in intrinsic linear scaling factors α_{13} , α_{23} , α_{31} and α_{32} . This holds if the system has a stable fixed point, and the extrinsic inputs change slowly relative to the characteristic time τ_e of the system. Therefore, these parameters are not varied, but chosen according to the suggestions of Jansen and Rit [54].

To summarize, the dynamics of the system are captured by varying five parameters: the extrinsic input levels to the three NMs (i. e., $x_{1T}(\kappa)$, $x_{2T}(\kappa)$ and $x_{3T}(\kappa)$), and the excitatory and inhibitory dendritic time constants (i. e., τ_e and τ_i) resulting in different ratios β . All

other parameters are chosen according to the suggestions of Jansen and Rit [54]. The reduction to five effective control parameters implies stable manifolds in the original 14-dimensional state space, thus allowing its reduction to twelve dimensions^b.

It should be pointed out that this type of analysis can be modified or extended in several ways, for example, by using other parameters for the bifurcation analysis, by using higher co-domains, or by applying the analysis to other models such as networks of several single area NMMs.

Parameter Ranges

Extrinsic input on all three NMs are specified to cover the effective ranges of extrinsic inputs as discussed in Sections 3.2.1 and 4.2. Simulations of single neurons have shown that the dendritic time constants of the somatic response due to synaptic input for single neurons seem to vary between 4×10^{-3} s and about 30×10^{-3} s, depending on the distance between soma and synapse [206, 207]. For the sake of inclusive treatment, the range of 2×10^{-3} s to 60×10^{-3} s is used; as did David and Friston [48]. The ranges of the five varied parameters (i.e., excitatory and inhibitory dendritic time constant and the three extrinsic inputs) are listed in Table 5.1.

5.1.2 System Analysis Using Bifurcation Theory

Bifurcation diagrams show the asymptotically invariant behavior of a system by displaying the steady-state phase portrait, or a projection thereof, as a function of one or more system parameters. With smooth changes in these parameters, the dynamic behavior of the system may undergo sudden and drastic changes called bifurcations. Throughout this work, the diagrams are of codimension one bifurcation, and plot

^bBecause afferents from PCs on EINs and IINs are excitatory, under the assumption that $h_{13}(\kappa) = h_{23}(\kappa) = h_e(\kappa)$, Eqs. (4.5) and (4.6) can be merged as follows: $x_{13}(\kappa) = o_{13} x_{03}(\kappa)$ and $x_{23}(\kappa) = o_{23} x_{03}(\kappa)$ with $x_{03}(\kappa) = m_c/u_c \int_{\kappa} ds \bar{h}_{13}(\kappa - s) z_3(s) = m_c/u_c \int_{\kappa} ds \bar{h}_{23}(\kappa - s) z_3(s)$.

the asymptotic states of PSPs of the PCs (e.g., fixed points, LCs or chaotic behavior evolving in time) against the extrinsic input on the PCs (see Fig. 5.1 and Figs. 5.9 to 5.12). To give an impression of the whole parameter space, planes of the dendritic time constants (see Figs. 5.4, 5.6 and 5.8) and of the extrinsic inputs on EINs as well as IINs (see Fig. 5.5 and Fig. 5.7) are spanned using a classification of codimension one branches (see Fig. 5.3). An excellent treatment of the essentials of bifurcation diagrams with special emphasis on their use for neuronal dynamics can be found in Breakspear and Jirsa [239]. A system analysis of a single NM can be found in the Appendix A.4.

Bifurcation diagrams are created to analyze the impact of extrinsic inputs and dendritic time constants on the system output, that is, the PSPs of the PCs, which are believed to be the main contributors to M/EEG (see Section 4). In the first step, the fixed point or equilibrium curve is defined. The state system \mathcal{P}_ϕ (see Eq. (2.1) in Section 2.2) can be expressed in vector form $d\phi/d\kappa = \mathcal{P}_\phi(\phi, \theta)$, with the state vector $\phi(\kappa) = (\mathbf{x} \ \mathbf{y})^T$, where $\mathbf{x}(\kappa)$ is the seven-dimensional vector of the PSPs (see Eqs. (4.1) to (4.7)), and $\mathbf{y}(\kappa)$ is the vector of the derivatives of $\mathbf{x}(\kappa)$ (i.e., currents) and the five-dimensional parameter vector $\theta = (z_{1T}(\kappa) \ z_{2T}(\kappa) \ z_{3T}(\kappa) \ \tau_e \ \tau_i)^T$. The derivative state vector $d\phi/d\kappa$ is a smooth function \mathcal{P}_ϕ of the system state vector $\phi(\kappa)$ and the system parameter vector θ .

Fixed Points

Fixed points of the system ϕ_0 are obtained by setting the derivatives to zero, that is, $d\phi/d\kappa = \mathbf{0}_{14 \times 1}$, where $\mathbf{0}_{14 \times 1}$ is the 14-dimensional zero vector. The coordinates of the fixed points cannot be expressed explicitly as a function of the extrinsic inputs. There is, however, a way to express the relationship between the system output (PSP of PCs) and the extrinsic input on PCs. To calculate the equilibria $\mathbf{0}_{14 \times 1} = \mathcal{P}_\phi(\phi_0, \theta_0)$ is mapped to the PSP of the PCs $x_{3,0} = x_{31,0} + x_{32,0} + x_{3T,0}$. From Eqs. (4.1) to (4.7) it follows that the fixed points $x_{3,0}$ of the PSP

of PCs can be defined in the $(x_{3,0}, x_{1T,0}, x_{2T,0}, x_{3T,0})^T$ space

$$\begin{aligned} x_{3,0} = & \alpha_{31} S_1(\alpha_{13} S_3(x_{3,0} + x_{1T,0})) \\ & + \alpha_{32} S_2(\alpha_{23} S_3(x_{3,0} + x_{2T,0})) + x_{3T,0}, \end{aligned} \quad (5.1)$$

where the constant extrinsic PSPs $x_{bT,0}$ simply represent just linear weighted constant mean firing rates of projections from outside $x_{bT,0} = \alpha_{bT} z_{bT,0}$ with $b = \{1, 2, 3\}$. This equation can be solved for the extrinsic input on PCs $x_{3T,0}$ as a fixed point curve function of the extrinsic inputs on interneurons and the PSP of the PCs, yielding unique mapping that can be used for the analytical computations. Note that, as described above (see Section 5.1.1), the area under the kernels and thus the coupling factor α_{ba} is fixed. Hence, the shape of the fixed point curve only depends on the extrinsic inputs to the EINs and IINs, but not on the intrinsic temporal ratios β_{ba} (i.e., τ_e and τ_i). Every fixed point is completely determined algebraically in the state space by the fixed point term $x_{3,0}$ of the PSPs of the PCs, $\phi_0 = \mathcal{P}_{0,\phi}(x_{3,0}, z_{1T,0}, z_{2T,0}, z_{3T,0})$ with

$$\phi_0 = \begin{pmatrix} \alpha_{13} S_3(x_{3,0}) \\ \alpha_{23} S_3(x_{3,0}) \\ \alpha_{31} S_1(\alpha_{13} S_3(x_{3,0}) + \alpha_{1T} z_{1T,0}) \\ \alpha_{32} S_2(\alpha_{23} S_3(x_{3,0}) + \alpha_{2T} z_{2T,0}) \\ \alpha_{1T} z_{1T,0} \\ \alpha_{2T} z_{2T,0} \\ \alpha_{3T} z_{3T,0} \\ \mathbf{0}_{7 \times 1} \end{pmatrix}, \quad (5.2)$$

where $\mathbf{0}_{7 \times 1}$ is the seven-dimensional zero vector. In the second step, the behavior near the fixed points ϕ_0 can be studied by linearizing the 14-dimensional system and evaluating its Jacobian matrix at the fixed points (5.2). The eigenvalues of the Jacobian are analyzed in order to specify the local stability properties such as stable or unstable nodes,

foci or saddles. Since there is no explicit form for the eigenvalues of the Jacobian as function of the extrinsic input on the PCs, the eigenvalues are computed for 10×10^4 equally spaced points. Note that the Jacobian depends on the extrinsic inputs as well as on the intrinsic temporal ratios. This means that, for any particular extrinsic input configuration, although the fixed point curve is constant in the 14-dimensional state space, the behavior in the vicinity of the fixed points varies with the dendritic time constants (or the intrinsic temporal ratio). System stability changes if at least one eigenvalue of the system crosses the imaginary axis. Points with zero real part(s) are called critical or nonhyperbolic fixed points, indicating possible *local bifurcations*.

Bifurcations

To identify bifurcations, the critical points are first located using a numerical nonlinear optimization technique (for more details about the method and its setup see Section 3.3.1 in the Mathematics and Methods Chapter 3). Second, the bifurcations are classified using the mathematical theory of codimension one bifurcations [222,245]. Here, the analysis distinguishes between the Andronov-Hopf (AH) bifurcation family and the saddle type. AH-bifurcations occur if a change in the investigated system parameter (in the present case the extrinsic input to the PCs) causes two complex conjugate eigenvalues to cross the imaginary axis (i. e., the real part changes from positive to negative or vice versa). In this case, LCs can arise. Depending on the first-order Lyapunov exponent, supercritical and subcritical AH-bifurcations are differentiated; in the first case, the LCs are stable; otherwise they are unstable. The saddle bifurcation family occurs if at least one (but not all) eigenvalue crosses the imaginary axis so that the eigenvalues in at least one of the two states have both negative and positive real parts. Depending on the leading eigenvalue (which plays an important role, especially for Shil'nikov's homoclinic bifurcations present in the dynamics), there are

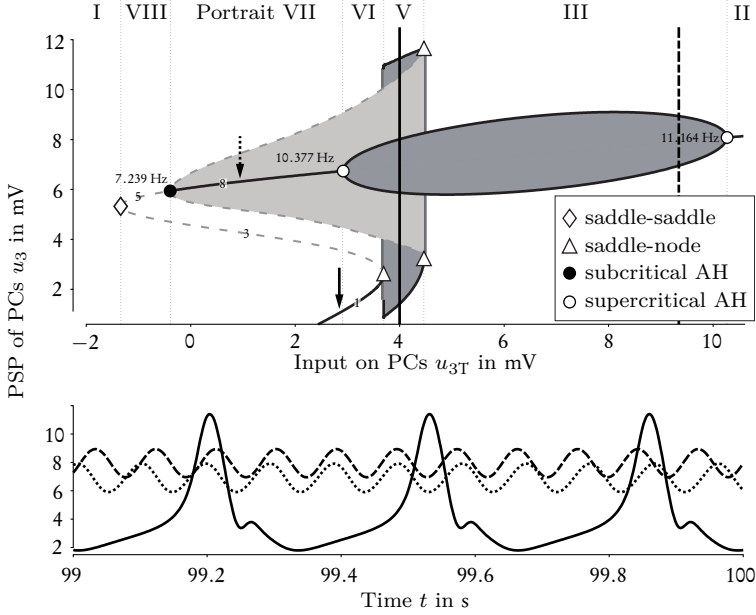


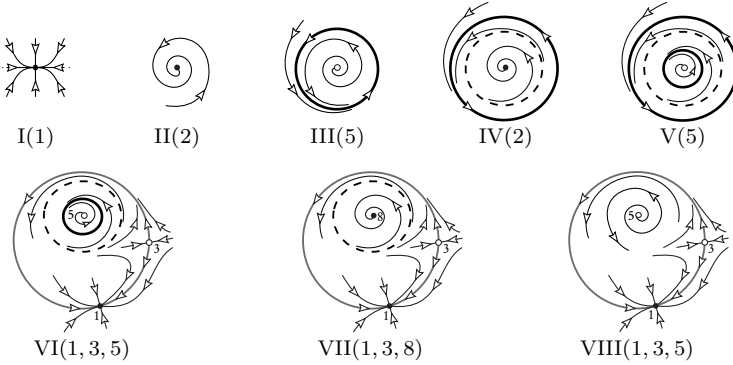
Fig. 5.1. Bifurcation diagram of Jansen's configuration ($u_{1T} = u_{2T} = 0$, $\beta = 1/2$, $\tau = 10$ ms and $u_c = 1.786$ mV). The diagram shows two telescoped branches of type I-B and II-AA (see Fig. 5.3). Solid and dashed curves represent stable and unstable states respectively. LC-branches correspond to gray regions with solid or dashed edges for stable or unstable LCs. For all AH-bifurcations, the eigenfrequencies are indicated. Bifurcations stratify the parameter axis (i. e., extrinsic input on PCs) into domains with characteristic phase portraits (presented in Fig. 5.2). The gray vertical lines indicate global bifurcations, here a saddle-node bifurcation in a Poincaré map occurring at the transition V-III and a Shil'nikov bifurcation (saddle-node) at the transition VI-V. Different input levels (bold black and dashed vertical lines) result in different behavior depending on the initialization (arrows). For inputs of portrait V, the system produces sinusoidal oscillations (dotted line) starting from the dotted arrow and spiking activity (solid line) starting from the solid arrow. For inputs beyond portrait V, the system is independent of the past, and produces sinusoidal oscillations (dashed line) within portrait III, for example.

three possible types of counterpart state, and this leads to the definition of three types of saddle bifurcations. For saddle-node bifurcations, all real parts of the hyperbolic eigenvalues have the same sign and the crossing eigenvalues (non-hyperbolic) are real-valued. If all real parts of the hyperbolic eigenvalues have the same sign and the crossing eigenvalues are complex conjugate, one speaks of a saddle-focus bifurcation. Finally, if the hyperbolic eigenvalues still have both negative and positive real parts, the bifurcation is of the saddle-saddle type, meaning that the topology of the saddle and not its stability changes. In general, a saddle-saddle bifurcation refers to the situation where two saddles of different types collide and vanish. All bifurcations are checked for their genericity^c. Saddle bifurcations which have homoclinic orbits, are called Shil'nikov bifurcations [80, 222, 246], and a check is made for further *global bifurcations* by using a numerical continuation algorithm (there are more details of the method and its setup in Section 3.3.1 of the Mathematics and Methods Chapter 3). The term global refers to the fact that the trajectory depends on more than the local properties in the vicinity of the fixed point.

In the last step, the bifurcation analysis is completed by the identification of the branches of LCs arising from local and global bifurcations. The bifurcating LCs are followed away from the bifurcation points. The initial periodic solutions for initializing the continuations of LC are taken from the bifurcation points, using a numerical continuation algorithm (again, see Section 3.3.1 in the Mathematics and Methods Chapter 3 for details).

^cEigenvalues reveal critical fixed points at which bifurcations could exist. However, the generation of a bifurcation at such a critical fixed point depends on non-degeneracy and transversality conditions, the so-called genericity conditions [222]. These conditions are inequalities involving partial derivatives of \mathcal{P}_ϕ with respect to ϕ , z_{1T} , z_{2T} and z_{3T} , evaluated at the nonhyperbolic fixed point.

Phase portraits



Fixed point characteristics

Type	Stable		Unstable					
	Node	Focus	Saddle			Node		Focus
Label	1	2	3	4	5	6	7	8
Leading	l_+	-	λ_1	λ_1	$\lambda_1 = \lambda_2^*$	$\lambda_1 = \lambda_2^*$	λ_1	$\lambda_1 = \lambda_2^*$
Eigenvalues	l_-	λ_1	$\lambda_1 = \lambda_2^*$	λ_2	$\lambda_2 = \lambda_3^*$	λ_3	$\lambda_3 = \lambda_4^*$	-

Fig. 5.2. Schematic phase portraits representing the qualitative system states of the domains in the bifurcation diagrams. Note that these phase portraits display the principal features in a plane according to the leading eigenvalues, while the actual phase portraits live in 14-dimensional space. There is a reference to the regimes here portrayed in the bifurcation diagrams (e. g., Portrait III) in Fig. 5.1 and Figs. 5.9 to 5.11. Portraits I and II show stable fixed points, portraits III-V are due to AH-bifurcations and portraits VI-VIII are possible combinations of these, and lead to heteroclinic cycles. Portrait I is a stable node and II is a stable focus. Phase portrait III consists of one stable LC. Phase portraits IV and V are similar to III, but with more than one LC: one stable and one unstable LC in IV and two stable and one unstable LC in V. Phase portraits VI-VIII comprise heteroclinic cycles due to the coexistence of a saddle and a node. The LCs in VI and VII as well as the unstable focus in VIII force the system to connect unstable and stable manifolds of the saddle and node stabilities, that is, to produce heteroclinic cycles. The fixed points in the phase portraits are characterized with respect to the leading eigenvalues, which play an important role, especially for the Shil'nikov bifurcations. The eigenvalues with positive (or negative) real parts that are closest to the imaginary axis are called the unstable l_+ (or stable l_-) leading eigenvalues.


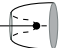
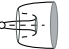






Type I	Bifurcations for generation	Transitions of orbits
A 	1 supercritical AH (○) 1 Shil'nikov (gray disk)	—
B 	1 subcritical AH (●) 1 Shil'nikov	1 global bifurcation (gray circle) e. g., saddle-node bifurcation in Poincaré maps
C 	1 supercritical AH (○) 1 Shil'nikov	2 global bifurcations (see type I-B)
Type II		
AA 	2 AH of the same type (○)	—
AB 	1 super- (○) and subcritical (●) AH	1 global bifurcation (see type I-B)
AC 	2 AH of the same type (○)	2 global bifurcations (see type I-B)
BB 	2 AH of the same type (●)	2 global bifurcations (see type I-B)
BC 	1 super- (○) and subcritical (●) AH	3 global bifurcations (see type I-B)
CC 	2 AH of the same type (○)	4 global bifurcations (see type I-B)

Fig. 5.3. Classification of the globally stable branches of LCs. Principal types I or II were classified according to the number of involved AH-bifurcations. The number of global bifurcations (red circles) that change the stability of the LCs is indicated by capital letters (A to C). Each global bifurcation is assigned to a AH-bifurcation by the shortest distance on the equilibrium curve. Fundamental frequencies of LCs of branch type II-AA are relatively stable because the orbit is generated by AH bifurcations only. On the other hand, the oscillation frequencies vary across a broad range for all LC-branches of type I due to the involved Shil'nikov bifurcation. Sinusoidal or harmonic oscillations are exclusively produced in the LC-branch type I-B and II-BB. All other branch types produce both types of oscillations.

Out of all these procedures come bifurcation diagrams comprising fixed points, stabilities, local as well as global bifurcations, branches of LCs and schematic phase portraits representing each state. As an example, Fig. 5.1 shows the bifurcation diagram of the standard parameter configuration proposed by Jansen and Rit [54]. The dynamic behavior for a specific parameter value can be illustrated by schematic phase portraits (see Fig. 5.2). These phase portraits show transient and steady-state trajectories in a two-dimensional subspace of the state space in a qualitative way. One can recognize oscillatory and non-oscillatory dynamics in the vicinity of fixed points and LCs, as well as heteroclinic orbits (see Fig. 5.2 for further details).

A Systematic Classification of LC-Branches

The analysis revealed various topological arrangements of branches of LCs for varying input and they were classified by their degree of nesting, as alternately stable and unstable LCs, separated by stability-changing global bifurcations. A comprehensive chart of all (globally) stable branches in the projection plane (x_{3T}, x_3) is shown in Fig. 5.3. First, branches are classified as principal types according to the number of AH-bifurcations involved, indicated by Roman numerals. Here, branches involving either one or two AH-bifurcations (principal types I and II) are found. Furthermore, each branch is classified more precisely according to its number of LC-stability-changing global bifurcations. Starting from a particular AH-bifurcation, the number of such global bifurcations is counted, indicated by capital letters. For example, branches are classified as A, B or C with no, one or two stability-changing global bifurcations, respectively. For branches of type II, each global bifurcation is assigned to either of the two AH-bifurcations (e.g., label AC for a type II branch means that one AH-bifurcation is not associated with any LC-stability-changing global bifurcation, while the other AH-bifurcation is associated with two global bifurcations). The association of AH to global bifurcations is based on the shortest distance to the

fixed point curve. Branches with a maximum of two stability-changing global bifurcations (labeled C) are found. Several LCs coexist for the same parameter set if (i) the corresponding branches are of type B or higher (see Fig. 5.3), (ii) branches are encapsulated in one another (see, for example, Fig. 5.9 for a II-AA branch encapsulated into an II-AB branch), or (iii) branches are telescoped into each other (see, for example, Fig. 5.10 for a II-AA branch telescoped into a II-AB branch). In the latter case, at least one global bifurcation (which changes the LC-stability) of a branch is in the range of another branch.

5.1.3 Results

As a first step, the standard configuration proposed by Jansen and Rit [54] is analyzed in which extrinsic inputs from other cortical and subcortical areas on interneurons (i. e., $x_{1T} = x_{2T} = 0$, $\tau = 1 \times 10^{-2}$ s and $\beta = 1/2$ with $\tau = \tau_c$) are not considered. This can be considered as an extension to the work of Grimbert and Faugeras [189] where an additional bifurcation is found. Then, the five-dimensional parameter space, spanned by the extrinsic input levels (at the PCs, EINs and IINs) and the inhibitory/excitatory dendritic time constants (see Table 5.1 for values used), is scanned systematically, computing a bifurcation diagram of the fifth parameter (i. e., extrinsic input level to the PCs) for each point in that space. In terms of steady-state dynamic behavior, two different basic oscillatory regimes were observed, which would be reflected in M/EEG: low amplitude sinusoidal oscillations caused by AH-bifurcations (referred to as *harmonic oscillations* throughout this work), and high-amplitude *anharmonic oscillations* (e. g., spike-like) caused by global bifurcations such as of Shil'nikov type. These phenomena were further characterized, in particular by determining the frequencies and amplitudes of the oscillations generated as well as their stability with respect to varying system parameters, and by considering the transitions between different oscillatory regimes through bifurcations. The classification scheme of the stable LC-branches intro-

duced in Section 5.1.2 is used in order to map the incidence of these topologies as well as the associated oscillatory regimes to the parameter space. Finally, some representative configurations are shown revealing new behavior, which is of potential biological interest.

The Jansen and Rit Configuration

The standard configuration of the NMM according to Jansen and Rit [54] was analyzed, reproducing and extending the results obtained by Grimbert and Faugeras [189]. See Fig. 5.1 for the bifurcation diagram. Fig. 5.2 shows the associated phase portraits, schematically illustrating the trajectories for the different regions of the bifurcation diagram. In accordance with Grimbert and Faugeras [189], One subcritical and two supercritical AH-bifurcations, a homoclinic saddle-node (Shil'nikov) and a global bifurcation were found. The two supercritical AH-bifurcations cause a branch of type II-AA (see Fig. 5.3), producing sinusoidal oscillations around $\eta_{\text{intr}} = 10.8 \times 10^{-2}$ (i. e., 10.8 Hz for $\tau = \tau_c$; see Table 3.3), which might serve as a theoretical basis for alpha rhythm generation, as suggested by Jansen and Rit [54]. The subcritical AH-bifurcation produces a branch of type I-B (see Fig. 5.3) featuring unstable LCs, and the saddle-node bifurcation causes stable homoclinic LCs with a fundamental frequency ranging between 1×10^{-3} and 4.6×10^{-2} , which could be used for modeling epilepsy-like spiking activity (see, for example, [64, 65, 76, 78]). Both stable homoclinic and unstable LCs collide and vanish through a global bifurcation (saddle-node bifurcation in Poincaré maps).

In addition to these results, a local saddle-saddle bifurcation was found that was not reported in the work of Grimbert and Faugeras [189]. This type of bifurcation does not represent a change in stability (i. e., lying within an unstable section of the fixed point curve) but a topological change of the saddle, in this case caused by complex conjugate

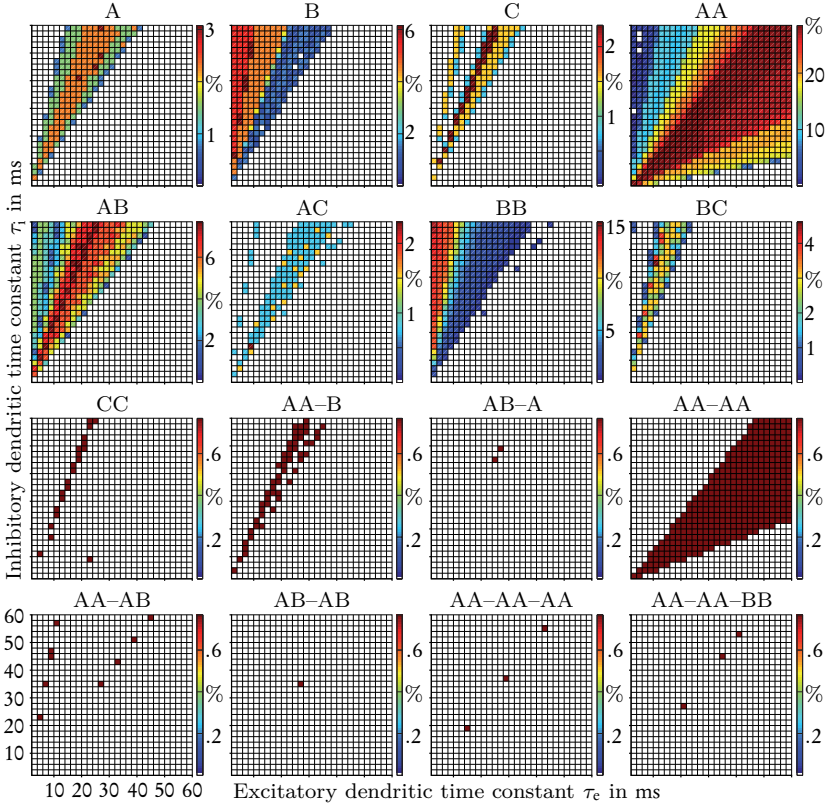


Fig. 5.4. Occurrence of branch types projected in the plane of the dendritic time constants. The most frequent type is II-AA, with 76.7%, followed by type II-AB (7.7%), II-BB (6.8%), II-B (4.2%), I-A (1.9%), II-BC (1.1%), I-C (1%), II-AC (0.6%) and II-CC (0.1%). Branches of type II-AA exist for configurations with dendritic time constant ratios $\beta < 5$, most frequently around ratios of $\beta = 1$. For increasing ratios, other types appear in the order: II-AB ($\beta < 0.77$, most frequently $\beta \approx 0.42$), II-AC ($\beta = 0.2$ to 0.73 scattered), I-A ($\beta = 0.24$ to 0.7), I-B as well as II-BB ($\beta < 0.65$, most frequently $\beta < 1/6$), I-C ($\beta = 0.17$ to 0.6 scattered, most frequently $\beta \approx 0.4$), II-CC ($\beta \approx 2/5$) and II-BC ($\beta = 0.17$ to 0.4). Combinations of types (1.7% of all of all configurations where stable LCs occur) and type II-CC occur rarely (singular phenomena). The configuration according to Jansen and Rit ($u_{1T} = u_{2T} = 0$, $\beta = 1/2$) is such a special case since it consists of branches of type I-B and II-AA. For the classification of branch types see Fig. 5.3.

eigenvalues. In particular, this bifurcation indicates that the system produces unstable oscillations for low amplitude inhibitory extrinsic input on PCs (i. e., lying on the section of the fixed-point curve between this local saddle-saddle bifurcation and the subcritical AH-bifurcation, see Fig. 5.1), due to the unstable focus in the corresponding phase portrait VIII in Fig. 5.2. Just like the saddle family of bifurcations in general, saddle-saddle bifurcations are, in principle, able to cause homoclinic LCs (Shil’nikov saddle-saddle bifurcation). However, in this case, no homoclinic LCs could be found using the Cl_MatCont package.

Mechanisms for Oscillations

Next, the modified model of a cortical area was analyzed by considering non-zero constant extrinsic input levels, $z_{1T}(\kappa)$, $z_{2T}(\kappa)$ and $z_{3T}(\kappa)$, on all three NMs, and by systematically varying these inputs as well as the dendritic time constants τ_e and τ_i . Therefore, a five-dimensional parameter space (see Table 5.1 for discretizations) was captured by computing a bifurcation diagram of the PSPs of the PCs against the extrinsic input $z_{3T}(\kappa)$ on the PCs for each combination of the remaining four parameters. The configuration of Jansen and Rit, as described above, represents only one particular case in this analysis.

Generally, two mechanisms for generating oscillations were found: AH-bifurcations and Shil’nikov bifurcations. For AH-bifurcations, one can compute eigenfrequencies. Although, in a strict sense, these frequencies apply only to the bifurcation point, they nevertheless give a good approximation for the oscillation frequencies of LCs at some distance in adjacent branches. In contrast, Shil’nikov, or more generally speaking, global bifurcations, usually do not offer such indications of oscillation frequencies because of the global dependencies, which are not reflected by the local eigenvalues. Upon passing Shil’nikov bifurcations, the homoclinic LCs suddenly appear with high amplitudes. The oscillation frequency is zero at the bifurcation point and greatly increases with increasing distance. Thus, in response to variations of the

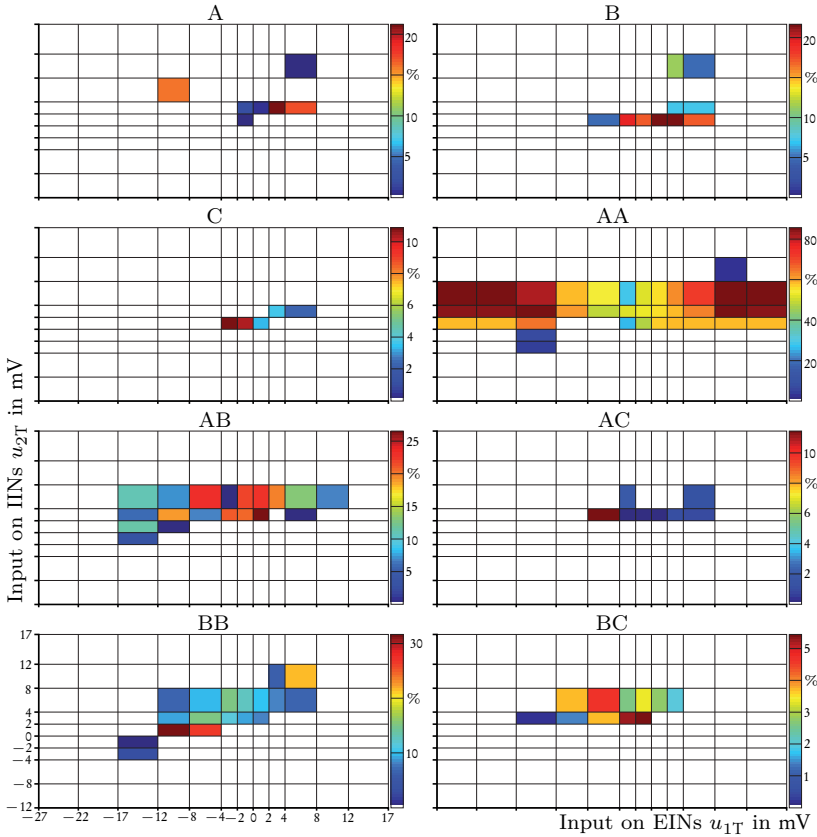
extrinsic input level to the PCs, the fundamental oscillation frequency is relatively constant for AH-LCs (*harmonic oscillations*) and quite variable for Shil'nikov's homoclinic cycles (*anharmonic oscillations*).

Upon passing the AH-bifurcation, the harmonic oscillations emerge gradually. Variations in the extrinsic input to the PCs (e.g., noise) result in some variations in amplitude and only small variations in frequency. This gives rise to waxing and waning oscillations of relatively stable frequency, as, for example, observed in EEG alpha waves. In contrast, upon passing a Shil'nikov bifurcation, highly anharmonic (i.e., spike-like) oscillations appear suddenly with high amplitude and low frequency (initially zero). The outcome of temporal variations in the extrinsic input to the PCs is moderate changes in amplitude and drastic changes in frequency. As a result, for noisy input, anharmonic oscillations that resemble M/EEG phenomena during epileptic seizures^d appear (see, for example, [64, 65, 76, 78]). Overall, the fundamental frequency ranged between 1×10^{-3} and 79.6×10^{-2} (i.e., 0.1 Hz and 79.6 Hz for $\tau = \tau_c$; see Table 3.3), covering the bulk of relevant frequency bands in M/EEG.

Conditions for Harmonic and Anharmonic Oscillations

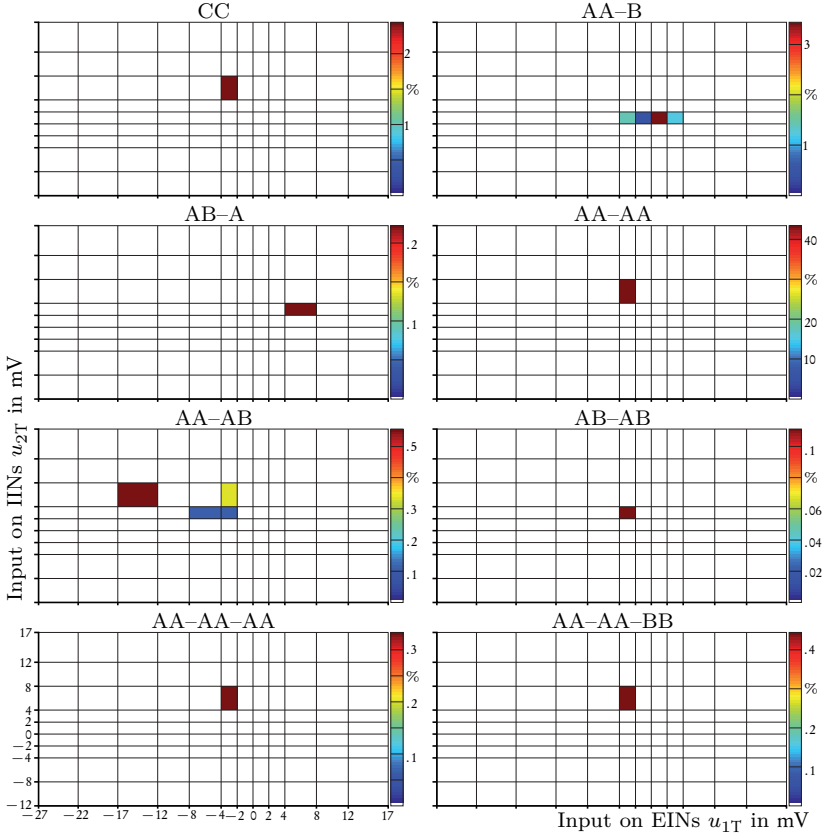
In Figs. 5.4 and 5.5, how frequently the various branch types occur (see Fig. 5.3) is plotted against the system parameters. The dynamics of the AA-branches caused by two supercritical AH-bifurcations are by far the most common phenomena (comprising about 77% of all investigated loci in parameter space where stable LCs occur). In particular, this type of behavior occurs in configurations with approximately equal inhibitory and excitatory dendritic time constants, that is, $\beta \approx 1$ in combination with extrinsic excitatory input on the IINs of less than

^dIt should be pointed out that, in general, all types of LCs can degenerate due to the nonlinearity and surjection (global shape) of the fixed point curve.



(a) Type I-A to C and type II-AA to BC

Fig. 5.5. Occurrence of branch types projected to the plane of the extrinsic input on INs (applying the characteristic mean PSP $u_c = 1.786$ mV). LC-branches of type II-AA are most frequent for configurations with extrinsic excitatory input on the IINs of less than 8 mV and with extrinsic input on the EINs of either less than about -17 mV (i. e., inhibitory) or more than about 8 mV (i. e., excitatory). Between -17 mV and 8 mV, most branches of type II-AA pass over to branches of type II-AA-AB, II-AA-BB and/or I-AA-B. Most LC-branches occur for input on IINs.



(b) Type II-CC and combinations of type II branches

Fig. 5.5. Branches of type II-AA-AA arise independently of the extrinsic input on EINs, but all other types and combinations of branches arise focally for a certain range. This means that extrinsic input on EINs causes most II-AA-AA branches to turn into more complex branches and combinations. The projection also reveals that combinations of branch types and branches of type II-CC are quite rare and local. The dominant combination of branches is II-AA, with 83.2 %, followed by AA-B (12.5 %), AA-AB (2.1 %), AA-AA-BB (0.9 %), AA-AA-AA (0.6 %), AB-A (0.4 %) and AB-AB (0.2 %). See Fig. 5.3, for the classification of branch types.

$x_{2T} \leq 4.48$ ($u_{2T} \leq 8 \times 10^{-3}$ V) or $z_{2T}^{(e)} \leq 49.23$ ($m_{2T}^{(e)} \leq 246.15$ spikes/s)^e and with extrinsic input on the EINs of either less than about $x_{1T} \leq -9.52$ ($u_{1T} \leq -17 \times 10^{-3}$ V) or $z_{1T}^{(i)} \geq 7.727$ ($m_{1T}^{(i)} \geq 38.64$ spikes/s) due to inhibition or more than about $x_{1T} \geq 4.48$ ($u_{1T} \geq 8 \times 10^{-3}$ V) or $z_{1T}^{(e)} \geq 49.23$ ($m_{1T}^{(e)} \geq 246.15$ spikes/s) due to excitation. In this list, the physical values that correspond to the Jansen and Rit parameters [54] have been put in parentheses, a convention which will be repeated in the rest of the chapter.

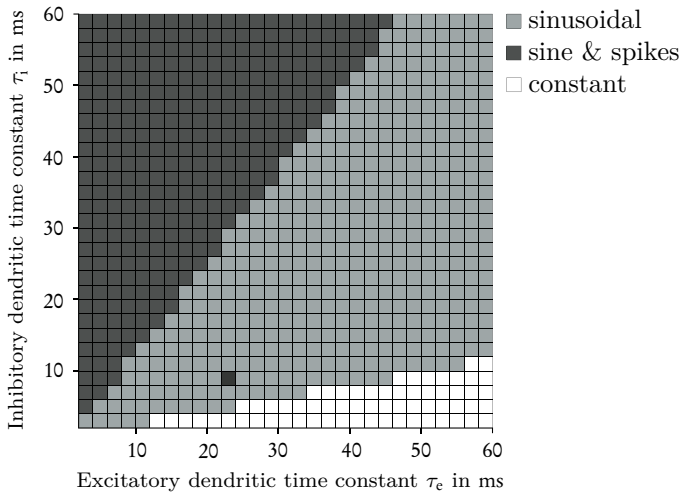


Fig. 5.6. LC-mechanisms of the parameter space projected onto the plane of the dendritic time constants. No LCs occur for dendritic time constant ratio $\beta \geq 5$ ($\beta = \tau/\tau_i$ with $\tau = \tau_e$). LCs occur for 24% of all parameter configurations. For ratios $\beta \leq 5$, configurations with AH-cycles exist, and further, for ratios $\beta \leq 0.77$, configurations containing both harmonic and anharmonic oscillations exist.

^eThe transformation from normalized PSP to normalized mean spike rate is done by division by the excitatory or inhibitory coupling factor $\alpha_{e,T}$ or $\alpha_{i,T}$.

Spontaneous average spike rates found in actual experiments do not usually exceed 10 Hz (in rats; e. g., [247,248]), but activity related rates can be as high as 80 Hz (see, for example, [249], for activity of pre-motor neurons in monkeys). This suggests that, in the model, the AA-branch behavior depends on a rather strong inhibition of the EINs. If the inhibitory dendritic time constant is larger than 1.3 times the excitatory one, that is, $\beta \approx 3/4$ and any of three conditions apply: the extrinsic input to the EINs lies between about $-9.52 \leq x_{1T} \leq 4.48$ ($-17 \times 10^{-3} \text{ V} \leq u_{1T} \leq 8 \times 10^{-3} \text{ V}$) or inhibitory input of less than $z_{1T}^{(i)} < 7.727$ ($m_{1T}^{(i)} < 38.64 \text{ spikes/s}$) or excitatory input of less than $z_{1T}^{(e)} < 49.23$ ($m_{1T}^{(e)} < 246.15 \text{ spikes/s}$), than branches of type II-AB occur, allowing both harmonic and highly anharmonic (often spike-like) oscillations. This scenario is more compatible with the typical moderate spike rates observed experimentally. If the inhibitory dendritic time constant is approximately three times larger than the excitatory one, that is, $\beta = 1/3$ BB- (only anharmonic oscillations) or B-branches appear with predominantly spiking activities. In the model, other branch types, in particular combinations of the basic types, cover only small portions of the parameter space. For example, the specific branch combination corresponding to the standard configuration of Jansen and Rit (i. e., AA-B) is restricted to input to IINs between $0 \leq x_{2T} \leq 1.12$ ($0 \leq u_{2T} \leq 2 \times 10^{-3} \text{ V}$) or excitatory input of less than $z_{2T}^{(e)} < 12.32$ ($m_{2T}^{(e)} < 61.54 \text{ spikes/s}$) and to input to EINs between $-2.24 \leq x_{1T} \leq 2.24$ ($-4 \times 10^{-3} \text{ V} \leq u_{1T} \leq 4 \times 10^{-3} \text{ V}$) or inhibitory input of less than $z_{1T}^{(i)} < 1.82$ ($m_{1T}^{(i)} < 9.09 \text{ spikes/s}$) or excitatory input less than $z_{1T}^{(e)} < 24.62$ ($m_{1T}^{(e)} < 123.08 \text{ spikes/s}$) and also limited to inhibitory time constants about twice that of the excitatory ones, that is, $\beta \approx 1/2$. Note that the translation from PSP to mean spike rate depends on the assumed products of dendritic time constant and synaptic gain, which was set to the values proposed by Jansen and Rit [54]. Moreover, the resulting mean spike rates represent the mean input rates of the respective NMs, which relate to the mean firing rates of the presynaptic neurons,

given connectivity constants ($z_{bT} = c_{bT} z_{T,b} = \{1, 2, 3\}$). These were set to 1 in this analysis, with the assumption that, on average, each presynaptic neuron contacts one postsynaptic one. Other values for the connectivity constants would result in scaling of the firing rates.

LC-branches of type II-AA provide harmonic oscillations with relatively stable fundamental frequencies because the orbit is only generated by AH-bifurcations. In contrast, due to the Shil'nikov bifurcation involved in all branches of type I, the oscillation frequencies vary across a broad range of values. The frequency ranges of all other branch types are dependent on the global bifurcations involved which change the stability of the LCs and generate anharmonic oscillations.

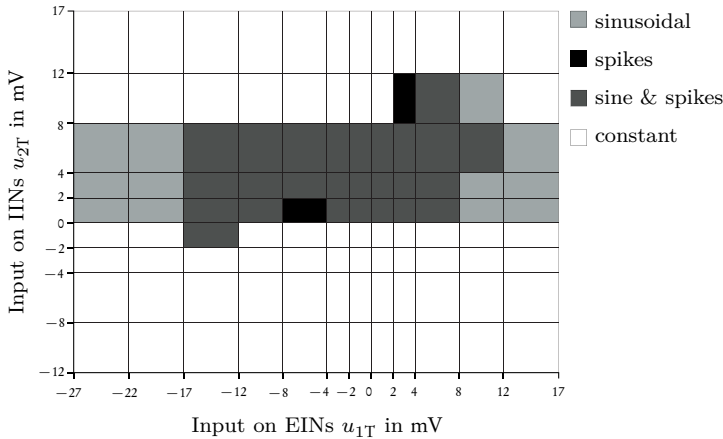


Fig. 5.7. LC-mechanisms of the parameter space projected onto the plane of the extrinsic inputs ($u_c = 1.786 \text{ mV}$). Inhibited IINs induce no LCs (with some exceptions). LC-branches, especially with harmonic oscillations, mainly occur for excited IINs (up to roughly 8 mV) for all inputs on EINs. Input on EINs is relevant for generating anharmonic oscillations (approximately between -17 mV to 8 mV).

Fig. 5.6 and Fig. 5.7 provide an overview of the circumstances under which the system produces harmonic and anharmonic (spiky) oscillations.

tions. In general, either type of oscillation is only possible if the dendritic time constant of the inhibitory synapses between interneurons and PCs is not too short compared to one of the excitatory synapses: $\beta \leq 5$ (see Fig. 5.6). Since the effective dendritic time constant increases with the average distance between synapses and soma (e.g., [207]), this means that, especially with excitatory input to more remote dendritic branches, there must be inhibitory synapses with rather large time constants in order to render the system capable of oscillating. The dendritic time constants also have a profound influence on the type and frequency of the oscillations that can be produced. If $\beta \leq 3/4$, the system may (depending on the extrinsic inputs and the initial conditions) produce high-amplitude anharmonic oscillations. Otherwise, only harmonic oscillations are generated, the frequency of which depends on the dendritic time constants in a systematic way; see Fig. 5.8 for examples. In general, the period of stable LCs increased with the dendritic time constants. In extension of the simulation-based frequency analysis of David and Friston [48], the generating mechanisms for the oscillations were captured.

For the standard configuration of Jansen and Rit [54], the parameter range where David and Friston [48] identified harmonic oscillations can be divided into two regions. For relatively short inhibitory dendritic time constants, that is, $\beta > 5$, stable foci were found instead of stable LCs, and therefore the system could only oscillate in the presence of constant perturbing extrinsic input, for example, noise. In contrast, if the inhibitory dendritic time constant is larger $\beta \leq 5$, stable LCs occur and the system oscillates autonomously, even with constant input. In particular, the anharmonic oscillations referred to as *hypersignals* by David and Friston are revealed to be due to LCs caused by global bifurcations. Bifurcation analysis thus offers a general means of having been distinguishing between intrinsic oscillations (stable LCs) and extrinsically driven oscillations (e.g., noise-driven stable foci).

With respect to the extrinsic inputs on EINs and IINs, Fig. 5.7 gives an overview of the conditions of occurrence for oscillations. Clearly, the system only oscillates if the IINs are not inhibited and are not excited above about 4.48 (8×10^{-3} V; with few exceptions). Moreover, anharmonic oscillations are limited to extrinsic inputs on the EINs between approximately -9.52 (-17×10^{-3} V, i. e., inhibition of the EINs and IINs) and 4.48 (8×10^{-3} V, i. e., excitation of the EINs and IINs).

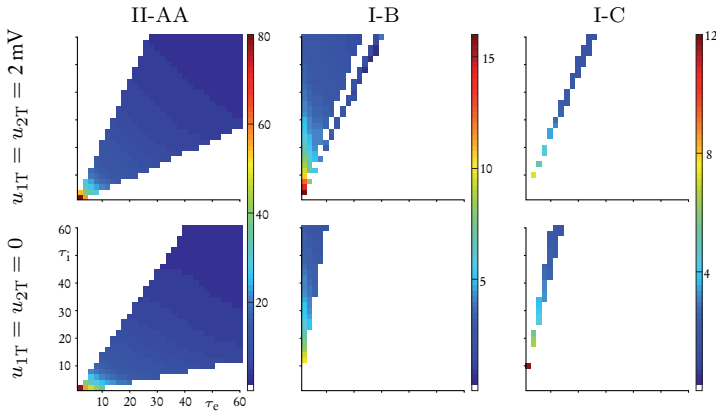


Fig. 5.8. Frequency charts of LC-branches. For two configurations of extrinsic inputs on INs (rows), it can be seen that the charts of branch types II-AA, I-B and I-C (columns) depending on the excitatory and inhibitory dendritic time constants (τ_e and τ_i). The configuration according to Jansen and Rit can be found in the first row ($u_{1T} = u_{2T} = 0$, $\tau_e = 10$ ms, $\tau_i = 2 \tau_e$). The oscillation frequency values of LCs in branches of type II-AA represent mean values over Hopf-cycle ranges and single values for type I branches (constant distance in relation to Shil'nikov bifurcations). For the classification of branch types see Fig. 5.3.

Example Configurations Illustrating Potential Applications

This section describes four exemplary configurations using the bifurcation diagrams. They have been selected to illustrate interesting transitional behavior between regimes, which may be potentially relevant

for modeling the brain processes underlying real M/EEG phenomena, such as ordered sequences of dynamic regimes (for modeling sequences in epilepsy by using thalamocortical models see, for example, [76–78]).

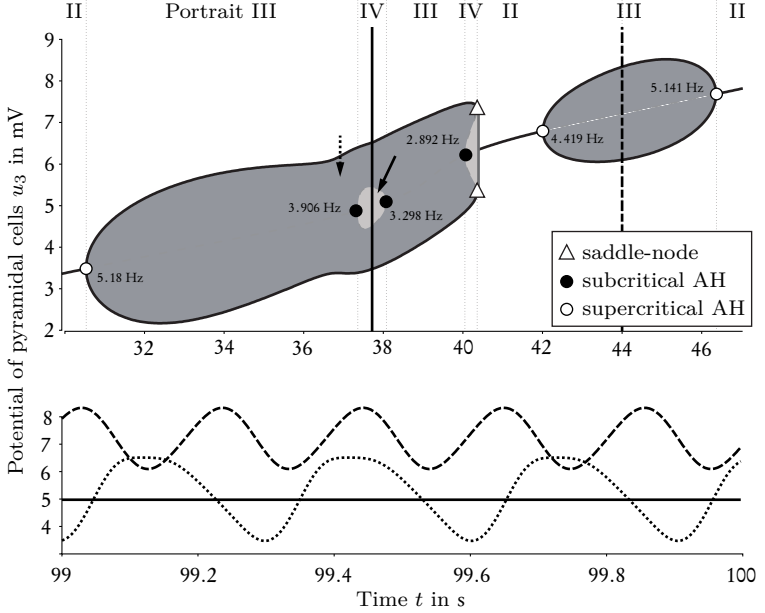


Fig. 5.9. Encapsulated LC (unstable II-AA) within another LC (II-AB next to a II-AA) of opposite stability (configuration: $u_{1T} = -4$ mV, $u_{2T} = -u_{1T}$, $\beta = 0.77$ with $\tau = 26$ ms and $u_c = 1.786$ mV). Anharmonic oscillations arises (e.g., black line) if the system is initialized outside of the unstable LC (dotted arrow and line). Otherwise, the output is constant (solid arrow and line), and may suddenly switch to oscillatory activities if moved over the separatrix by a perturbation. See Fig. 5.1 for further explanations.

The first example is presented in Fig. 5.9. It shows the system behavior for extrinsically inhibited EINs and excited IINs ($x_{1T} = -2.24$ and $x_{2T} = -x_{1T}$ or, alternatively, $u_{1T} = -4 \times 10^{-3}$ V and $u_{2T} = -u_{1T}$)

and a intrinsic temporal ratio of $\beta = 13/17$ (e. g., dendritic time constants $\tau_e = 26 \times 10^{-3}$ s and $\tau_i = 34 \times 10^{-3}$ s), which correspond approximately to the upper limit of the physiologically plausible range (see Section 4.2 for ranges of the system parameters). This example demonstrates the simultaneous existence of more than one LC-branch for the same parameter range; that is, for an unstable branch of type II-AA which is encapsulated in a branch of the same type but of opposite stability. Such stable II-AA-AB branches make up about 2% of all observed multi-branch configurations (see Figs. 5.4 and 5.5). The unstable AH-LCs act as the separatrix^f separating two system modes of behavior (here unstable from stable LCs). If the system is initialized inside the unstable AH-LCs, it will produce constant output, or, in the presence of low amplitude perturbations, damped oscillations (idle mode). If the system is then perturbed beyond the separatrix, it suddenly enters an excitation mode and produces anharmonic oscillations. This mechanism also works in the opposite way, from excitation to idle mode. However, the interesting feature is that this transition behavior is generally irreversible; that is, the system will not revert to its original mode even after the perturbing stimulus is gone. Such switching behavior in response to a brief stimulus is characteristic of many normal and pathological processes in the brain, such as, redirection of attention by a relevant sound or touch, waking up by salient stimulation, or epileptic seizures elicited by sudden, unexpected stimuli (startle epilepsy).

The second example in Fig. 5.10 shows a case with still stronger inhibition of the EINs ($x_{1T} = -9.52$ and $x_{2T} = 2.24$ or, alternatively $u_{1T} = -17 \times 10^{-3}$ V and $u_{2T} = 4 \times 10^{-3}$ V) and short dendritic time constants for the excitatory synapses, meaning an intrinsic temporal ratio of $\beta = 2/11$ (e. g., dendritic time constants $\tau_e = 4 \times 10^{-3}$ s and $\tau_i = 5.5 \tau_e$). The bifurcation diagram reveals overlapping but separate

^fA separatrix marks a boundary between trajectories with different properties.

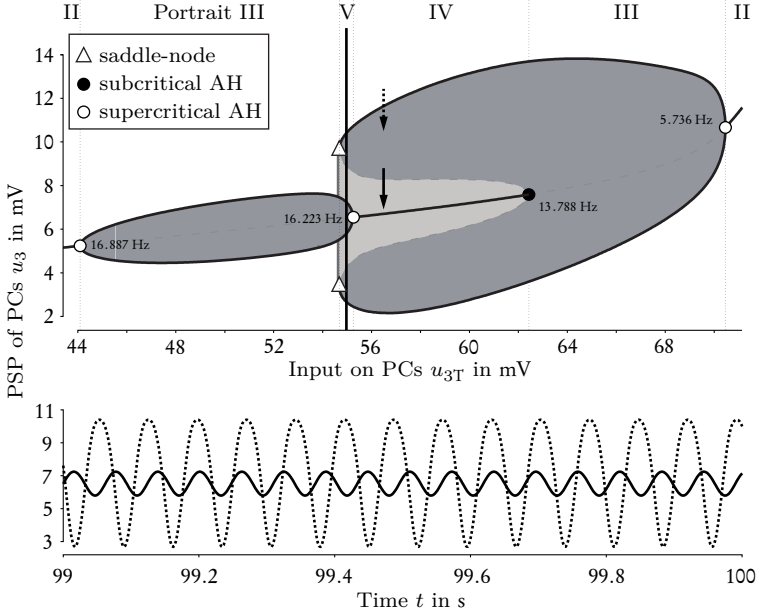


Fig. 5.10. Overlapping branches (II-AA and II-AB) provide two coexisting stable LCs (configuration: $u_{1T} = -17$ mV, $u_{2T} = 4$ mV, $\beta = 2/11$ with $\tau = 4$ ms and $u_c = 1.786$ mV; see also Fig. 5.1). The coexistence is sensitive to the initialization (arrows). The state changes from low- (solid arrow) to high-amplitude LCs by passing the subcritical AH-bifurcation (e. g., exciting the PCs by 8 mV), and remains unless the system passes the saddle-node bifurcation (e. g., inhibiting PCs by -3 mV).

branches, which provide three LCs for the same parameter setting: a branch of type II-AA which is shifted into a branch of type II-AB (with about 2% occurrence, where 20% of these are telescoped). This configuration reveals that it is possible to enter into an LC both suddenly and continuously, also to switch suddenly between LCs. The system traverses regimes (branches) in qualitatively different ways for increasing and decreasing extrinsic input on PCs. For instance, the system suddenly switches from idle mode (stable focus in phase portrait IV with initialization indicated by the blue arrow and an input level of

about $x_{3T} = 31.36$ or $u_{3T} = 56 \times 10^{-3} \text{ V}$) to excitation mode (high amplitude anharmonic oscillations) for increasing input (exceeding about $x_{3T} = 35.84$ or $u_{3T} = 64 \times 10^{-3} \text{ V}$) by passing the subcritical AH-bifurcation (here the phase portrait switches from type IV to III). It remains in the excitation mode even after cessation of the input perturbation (potential back to $x_{3T} = 31.36$ or $u_{3T} = 56 \times 10^{-3} \text{ V}$), thus providing a mechanism for irreversible change caused by a transient input perturbation (see previous example). Additionally, the system may change suddenly from one excitation mode (anharmonic oscillations) to another (harmonic oscillations) for decreasing inputs (below about $x_{3T} = 30.24$ or $u_{3T} = 54 \times 10^{-3} \text{ V}$) by passing through a global bifurcation (changing the phase portrait from V to III). If the input to the PCs then returns to the original level, the system returns to its original idle mode by passing a supercritical AH-bifurcation (to phase portrait IV). Hence, in contrast to the configuration shown in Fig. 5.9, the effects of strong perturbations are reversible by traversing several different states (represented by the respective phase portraits, see Fig. 5.2).

The third example in Fig. 5.11 describes the system behavior for extrinsically inhibited EINs and excited IINs ($x_{1T} = -2.24$ and $x_{2T} = -x_{1T}$ or, alternatively, $u_{1T} = -4 \times 10^{-3} \text{ V}$ and $u_{2T} = -u_{1T}$) and an intrinsic temporal ratio of $\beta = 7/9$ (e.g., dendritic time constants $\tau_c = 14 \times 10^{-3} \text{ s}$ and $\tau_i = 18 \times 10^{-3} \text{ s}$). This configuration shows that several branches might coexist separately along the fixed point curve, lined up like beads on a string. This configuration (type II-AA-AA-AA, which makes up about 0.6% of all multi-branch configurations) does not result in any sudden changes, but, depending on varying extrinsic input on PCs, the system will alternate between idle or excitation mode, producing harmonic oscillations of different frequencies. If the input to the PCs is noise of sufficiently high amplitude, the output will be a mixture of unfiltered noise and various frequencies generated by the different LCs. This may be the basis for a model of M/EEG spectra

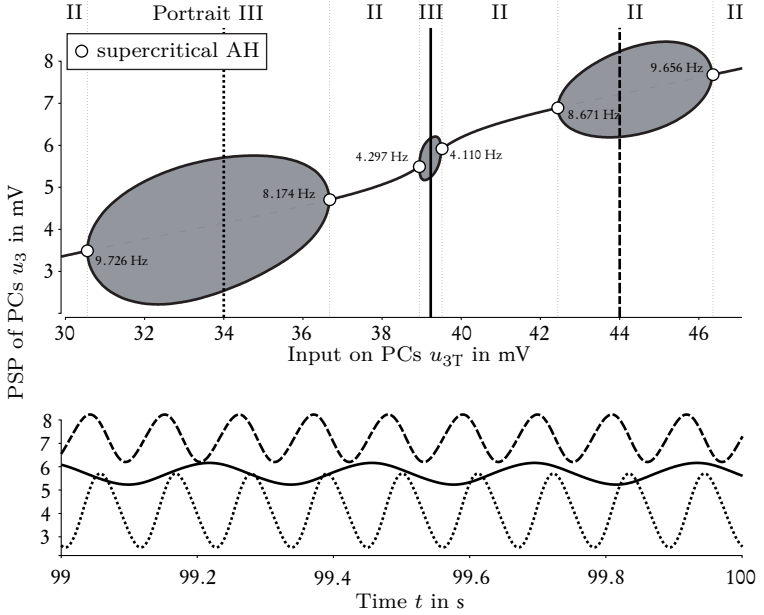


Fig. 5.11. Existence of several stable LC-branches (II-AA) across the extrinsic input on PCs (configuration: $u_{1T} = -4$ mV, $u_{2T} = -u_{1T}$, $\beta = 7/9$ with $\tau = 14$ ms and $u_c = 1.786$ mV; see also Fig. 5.1). The time series belong to different input levels.

featuring several distinct frequency peaks, for example, in the theta and alpha ranges as in this case.

Finally, as a fourth example, the configuration of Jansen and Rit itself (see Fig. 5.1) demonstrates the coexistence of two branches of LCs of type I-B and II-AA, giving rise to spike-like and sinusoidal activity respectively. This configuration allows, by virtue of the changed input to the PCs, an abrupt transition from the I-B-cycle (anharmonic oscillations) to the II-AA-cycle (harmonic oscillations), but not the reverse transition. Fig. 5.12 shows how the gradual increase of extrinsic input to the IIN changes the bifurcation diagram and causes the system

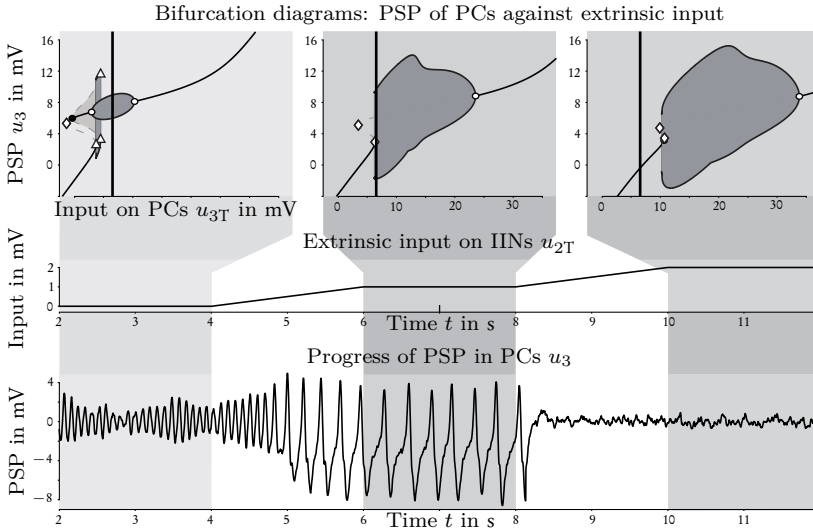


Fig. 5.12. Extrinsic inputs on IINs change the system behavior (configuration: $\beta = 1/2$ with $\tau = 10\text{ms}$ and $u_c = 1.786\text{mV}$). By exciting IINs the system switches from producing waxing and waning alpha activity in the first state to epileptic spike-like activity in the second state, and to noise-driven activity in the last state of excitation. The first extrinsic input state on IINs corresponds to Jansen's configuration (i.e., only extrinsic input on PCs). For the second input state the input on IINs is constantly 1mV and doubles for the third input state. The extrinsic input on the PCs is Gaussian (with an expectation value of $E[u_{3T}] = 6.5\text{mV}$ and a standard deviation of $D[u_{3T}] = 1.3\text{mV}$) and zero for the EINs during all states. For each state, the bifurcation diagram (of the PSP against the extrinsic input on PCs) is shown in the top row. The input on IINs and the PSPs of the PCs is shown in the middle and bottom row. Regarding the bifurcation diagrams, circles are subcritical (black) and supercritical (white) AH-bifurcations, diamonds are saddle-saddle and triangles are saddle-node bifurcations. The gray vertical lines represent global bifurcations. The black bordered gray areas are the branches of LCs. Using the classification of LC-branches (see Fig. 5.3), the first input state was identified as a combination of type I-B and II-AA, the second and third input state of type I-A. The black vertical lines indicate the expectation value of the Gaussian input on the PCs. Thus, the alpha activity is caused by harmonic cycles due to AH-bifurcations in the first state and the epileptic spiking-like activity of the second state is caused by homoclinic cycles due to a saddle-node Sil'nikov bifurcation. In the last state, the system is out of reach of any LC and attracted to the equilibrium disturbed by the extrinsic Gaussian input on PCs.

to go through different distinct oscillatory regimes. The system is exposed to Gaussian input to the PCs (expectation value $E[x_{3T}] = 3.64$ or $E[u_{3T}] = 6.5 \times 10^{-3} \text{ V}$ and standard deviation $D[x_{3T}] = 0.728$ or $D[u_{3T}] = 1.3 \times 10^{-3} \text{ V}$) and there is no extrinsic input to the EINs in this example. With no input to the IINs, this configuration is identical to that of Jansen and Rit and produces waxing and waning harmonic oscillations in the alpha range. If the input to the IIN is increased, the system's behavior, and thus the bifurcation diagram, changes and the system starts to produce large amplitude spike-like anharmonic oscillations of varying frequency. A further increase in the IIN's input moves the system into a state where it generates constant output with overlaid noise (see Fig. 5.12). This demonstrates that changes in the system behavior reflect not only bifurcations due to the extrinsic inputs on PCs but also along with the bifurcations due to the other codimensions (i. e., extrinsic inputs on both types of interneurons, EINs and IINs). Although codimension five bifurcations were not analyzed, the diagrams in Figs. 5.4 to Fig. 5.7 give an insight into the system's behavior for the whole parameter space (based on the classification scheme).

5.2 Periodically Forced Model

As demonstrated in the previous Section, 5.1, even in the absence of any time-variant input, the NMM is intrinsically capable of reproducing a variety of biologically relevant behavior, especially rhythms. The system was investigated under the assumption of constant extrinsic input levels, thereby allowing the system to settle into a stable state (e.g., fixed point or LC). In the brain, however, such local neuronal circuits are embedded in larger networks and are likely to experience high amplitude time-varying input from other parts of the brain. Because neuronal ensembles tend to oscillate intrinsically, such input is very often periodic, as evidenced by the widespread occurrence of rhythms in both extracranial and intracranial recordings [81] and the conclusion of

the previous Section 5.1. These intrinsic rhythms can be experimentally influenced by stimulations such as visual flicker (e.g., [82]).

Consequently, in this section, the case of periodic stimulation is considered. For this purpose, the parameter set proposed in the work of Jansen and Rit [54] is used, where the system performs harmonic oscillations in the alpha frequency band [51, 189]. Instead of a constant input at the PCs a periodic input on INs is applied, consisting of brief pulses akin to that used by Jansen and Rit for eliciting visual evoked potentials [53, 54], or used in dynamic causal modeling (e.g., [50, 67]).

The results indicate that a relatively simple generative model of a local neuronal circuit is capable of producing surprisingly complex and diverse phenomena, which are observable in brain data and relevant for the explanation of brain function.

5.2.1 Parameter Space

In this section of the chapter, the dynamics of a periodically forced modified Zetterberg-Jansen model of a single cortical area is explored as a function of amplitude and frequency of the stimulus. What immediately follows is a justification of the model and the constraints.

Dimension Reduction

In the modified form of the Zetterberg-Jansen model described by the differential Eqs. (4.1) to (4.7), the system has 20 parameters^g. In line with the dimension reduction for analyzing the constantly forced Zetterberg-Jansen model in Section 5.1.1 only excitatory and inhibitory kernels $\bar{h}_e(\kappa)$ and $\bar{h}_i(\kappa)$ are distinguished with the dendritic time constant τ_e and τ_i , so that $\beta_{13} = \beta_{23} = \beta_{31} = 1$ and $\beta_{32} = \beta$ with $\beta = \tau_e/\tau_i$. Furthermore, the sigmoid parameter γ_b are the same for all NMs $\gamma_b = \gamma$,

^gThese are: the coupling factors α_{ba} , the intrinsic temporal ratios β_{ba} , with $ab = \{13, 23, 31, 32\}$; the parameters γ_b of the sigmoid function S_b (3.16); the extrinsic input levels to the three neural ensembles $z_{bT}(\kappa)$; the extrinsic temporal ratios β_{bT} and the coupling factors α_{bT} with $b = \{1, 2, 3\}$.

so that $S_b(x_b) = S(x_b)$ with $b = \{1, 2, 3\}$ (see Section 3.2.4 in Chapter 3). In this way, Eqs. (4.1) and (4.2) only differ by the coupling factors α_{13} and α_{23} , both equations can be merged to one excitatory projection x_{03} of the PCs to both types of interneurons. The other two intrinsic projections EINs to PCs (4.3) and IINs to PCs (4.4) incorporate x_{03} weighted by the coupling factors α_{13} and α_{23} . Hence, the dimension of the states is reduced by two. Here, the extrinsically caused PSPs $x_{bT}(\kappa)$ are directly considered instead of the incoming firing rates $z_{bT}(\kappa)$ neglecting the specific projections and thus Eqs. (4.5) to (4.7). In general, a constant input is unaffected, that is, linearly scaled by dendritic kinetics and a time-variant input is linearly low-pass filtered by dendrites depending on the dendritic time constant τ_{bT} .

PCs (3) to EINs (1) and IINs (2), combined to (0)

$$\begin{aligned}\dot{x}_{03}(\kappa) &= y_{03}(\kappa) \\ \dot{y}_{03}(\kappa) &= -2y_{03}(\kappa) - x_{03}(\kappa) + S(x_{31}(\kappa) + x_{32}(\kappa) + x_{3T}(\kappa))\end{aligned}\tag{5.3}$$

EINs (1) to PCs (3)

$$\begin{aligned}\dot{x}_{31}(\kappa) &= y_{31}(\kappa) \\ \dot{y}_{31}(\kappa) &= -2y_{31}(\kappa) - x_{31}(\kappa) + \alpha_{31} S(\alpha_{13} x_{03}(\kappa) + x_{1T}(\kappa))\end{aligned}\tag{5.4}$$

IINs (2) to PCs (3)

$$\begin{aligned}\dot{x}_{32}(\kappa) &= y_{32}(\kappa) \\ \dot{y}_{32}(\kappa) &= -2\beta y_{32}(\kappa) - \beta^2 x_{32}(\kappa) + \alpha_{32}\beta^2 S(\alpha_{23} x_{03}(\kappa) + x_{2T}(\kappa))\end{aligned}\tag{5.5}$$

where the state vector $\phi = (x_{03}, x_{31}, x_{32}, y_{03}, y_{31}, y_{32})^T$ contains the normalized mean PSPs x_{ba} and currents y_{ba} at NM b caused by NM a . The extrinsic afferents T projected to NM b are denoted by x_{bT} .

Parameter Ranges

The parameter space to be investigated is here specified. The system described by Eqs. (5.3) to (5.5) has nine parameters, namely coupling factors α_{ba} with $ba = \{13, 23, 31, 32\}$, intrinsic temporal ratio β , sigmoid parameter γ , and extrinsic inputs x_{bT} with $b = \{1, 2, 3\}$.

Following Jansen and Rit [54], the coupling factors $\alpha_{13} = 12.285$, $\alpha_{23} = \alpha_{13}/4$, $\alpha_{31} = 4\alpha_{23}/5$, and $\alpha_{32} = -11\alpha_{23}/13$, the kinetic ratio $\beta = 1/2$ and the sigmoid parameter $\gamma = 28.7892$ are used. The extrinsic inputs on the three NMs are taken to be constant for EINs $x_{1T} = 0$ and PCs $x_{3T} = 3.36$ (6×10^{-3} V), and time-variant for IINs in the form of periodic pulses $x_{2T}(\kappa) = \zeta \exp(-2\sigma \cos^2(\omega))$, with the angle ω

$$\dot{\omega} = \pi \eta, \quad (5.6)$$

is specified by stimulus amplitude ζ and stimulus frequency η (σ controls the shape and is set to $\sigma = 110$). Interestingly, a very similar waveform can be generated using a NMM of the thalamus, as proposed by Robinson et al. [168]. In this model, a strong inhibitory influence of the reticular nucleus to the thalamic relay cells during the relaying of external sensory stimulation, such as an on/off waveform of flickering lights, sharpens the cortical input to render it pulse-like. Such time-variant input onto the IINs may represent thalamic feed-forward input. This type of disynaptic *feed-forward inhibition* has been described as crucial for bottom-up processing in the somatosensory (e.g., [250, 251]), auditory (e.g., [252]), and visual (e.g., [253]) systems of rodents. Also, model analysis of the Jansen and Rit circuit suggests the importance of input on IINs for controlling cortical behaviors [51].

In the absence of stimulation (i.e., $x_{2T} = 0$), the system intrinsically performs LC-oscillations arising from AH-bifurcations, appearing as harmonic oscillations with a frequency of $\eta_{\text{intr.}} = 10.8 \times 10^{-2}$ (see bifurcation diagram and phase portraits, Fig. 5.1 and Fig. 5.2).

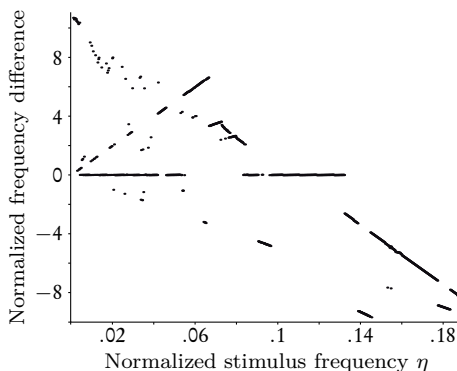


Fig. 5.13. Frequency entrainment effects in a periodically forced modified Zetterberg-Jansen model. A frequency-detuning curve refers to the difference between response and stimulus frequency plotted against the stimulus frequency for constant amplitude of 1.5 (which equals 2.679 mV for $u_c = 1.79$ mV). The largest peak in the power spectrum for each stimulus frequency defines the response frequency. A large entrainment range, meaning zero detuning, occurs around the intrinsic frequency $\eta_{\text{intr.}} = 0.108$ (which equals 10.8 Hz for the characteristic time constant $\tau = 10 \times 10^{-3}$ s) and around half that value.

Applying the characteristic dendritic time constant $\tau_e = 10 \times 10^{-3}$ s as specified by Jansen and Rit [54], this corresponds to an actual oscillation frequency of $f = 10.8$ Hz and can be used to describe alpha rhythms in brain signals. Note that varying the characteristic time constant τ (that is chosen to be the excitatory time constant $\tau = \tau_e$, see Section 5.2.1) only scales the neuronal states $\phi(\kappa) = (\mathbf{x}, \mathbf{y})^T$ in time $t = \tau\kappa$, and thus the frequency $f = \eta/\tau$, while the states $\phi(\kappa)$, the underlying mechanisms, such as bifurcations, and the form of time signals remain unaffected. Hence, the frequency depends on the choice of the characteristic time constant τ and thus the normalization embraces all cases of τ . In order to study the system with periodic stimulation around the intrinsic frequency ($\eta_{\text{intr.}} = 10.8 \times 10^{-2}$), the stimulus frequency η is taken to range from 0 to 0.19. The stimulus frequency is

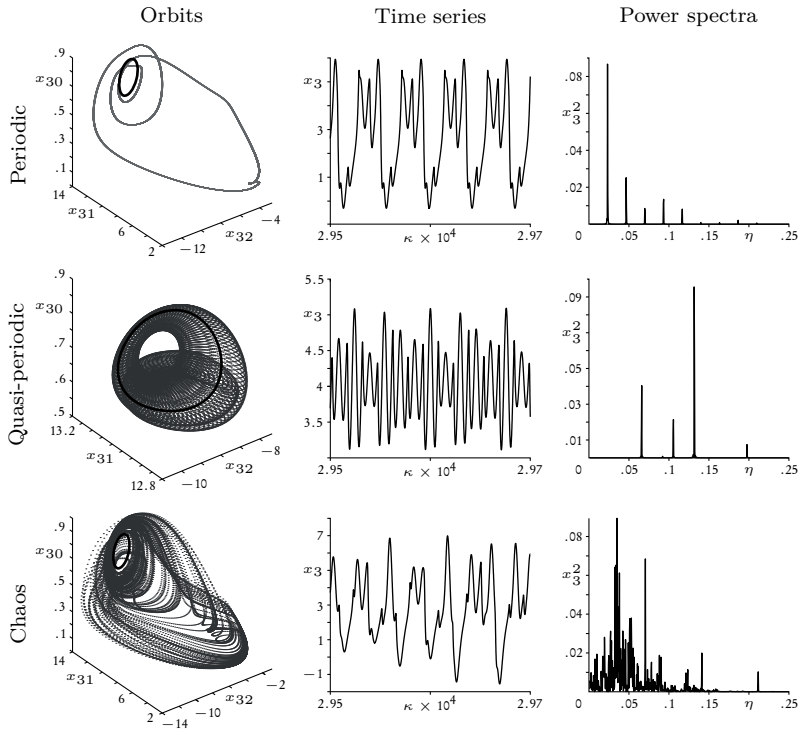


Fig. 5.14. Complex behavior occurring in the periodically forced modified Zetterberg-Jansen model. Orbits, time series, and power spectra (columns) are shown for three configurations (rows) displaying (from top to bottom) periodic (normalized input amplitude; normalized input frequency: 3.6301 ; 9.33×10^{-2}), quasi-periodic (1.5 ; 7.59×10^{-2}) and chaotic behavior (3.6301 ; 7.05×10^{-2}). The orbits are in the state space of normalized PSPs (of PCs) attributable to the EINs and IINs (x_{30}) as well as those at the two INs, caused by PCs (x_{31} and x_{32}). The black circles represent the stable LCs arising from AH-bifurcations in the unperturbed system. The time series and the power spectra are shown for the PSPs of PCs (which are related to M/EEG). Periodic behavior is characterized by a closed orbit (LC) and discrete power spectra with peaks at commensurable frequencies. Quasi-periodic behavior is characterized by trajectories forming an invariant n -dimensional torus and discrete power spectra with peaks at incommensurable frequencies. Chaotic behavior is indicated by a strange attractor, that is, a bounded attracting set in which all trajectories are unstable and nearby trajectories locally diverge from each other exponentially, and broadband power spectrum. Note that one obtains the physical values by applying characteristic constants (see, for example, Table 3.3).

nonlinearly sampled ensuring $1/(\eta \Delta \kappa) \in \mathbb{N}$ with the interval $\Delta \kappa$, so that the pulses are well sampled. The stimulus amplitude ζ is linearly sampled from 0 to 4.1 to cover the effective range of excitatory inputs on IINs within the LC exists for constant extrinsic input (see Fig. 5.7).

In summary, for analysis, a system of seven first-order ordinary differential equations (Eqs. (5.3) to (5.5)) is considered, describing the neuronal states $\phi(\kappa) = (x_{03}, x_{31}, x_{32}, y_{03}, y_{31}, y_{32}, \omega)^T$ specified by two parameters $\theta = (\zeta, \eta)^T$.

5.2.2 Stimulus Dependent State Space Analysis

The dynamical system (Eqs. (5.3) to (5.5)) whos studies numerically using the fourth-fifth order Runge-Kutta method over $\kappa = 30 \times 10^3$ in time (which equals 5 min for $\tau_e = 10 \times 10^{-3}$ s, according to Jansen and Rit [54]) with a relative tolerance of 10^{-11} , and then for further analysis linearly sampled with an interval $\Delta \kappa = 10^{-2}$. From the last 6×10^3 samples (i. e., from the final minute if $\tau_e = 10 \times 10^{-3}$ s), the histograms of each state were computed using the optimal number of bins [254]. Using the state equations, the *characteristic mean frequency* of each attractor was also computed [255]. The characteristic mean frequency is the time average of a trajectory over the angle velocity at points along an n -dimensional curvature forming an attractor in state space (see Appendix A.5 for more details). To study the complex behavior, the power density spectra of the time series (last 6×10^3 samples) was computed using the fast Fourier transform, especially for the time series of the mean PSPs of the PCs $x_3(\kappa) = x_{31}(\kappa) + x_{32}(\kappa) + x_{3T}(\kappa)$, which are reflected in M/EEG.

The characteristic Lyapunov spectra, that is, all six Lyapunov exponents $\lambda_1 > \lambda_2 \dots > \lambda_6$ were also computed directly from the differential Eqs. (5.3) to (5.5) (see Section 3.3.3). The time interval is sufficiently long to stably estimate the characteristic Lyapunov spectra

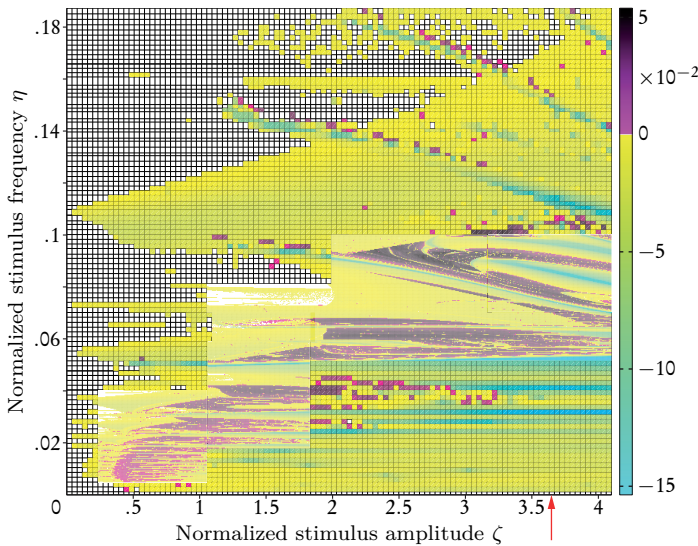


Fig. 5.15. Largest Lyapunov exponent in the parameter space of stimulus amplitude and frequency. Positive exponents (magenta to black) reflect diverging trajectories irrespective of how close they are, and thus chaos in the system. Zero exponents (white) indicate neutral stability, and negative exponents (cyan to yellow) reflect frequency locking. The red arrow indicates the amplitude for which the experimental data fits best (see Fig. 6.1 and Section 6.3 in the Chapter 6). Several parameter regions are zoomed at a finer resolution of stimulus amplitude and frequency. By applying characteristic constants (see Table 3.3) one obtains the physical values.

(error $< 10^{-6}$). The Lyapunov spectrum gives a quantitative measure of the sensitivity of the states of the system to the initial conditions; more precisely, it gives the average rate of divergence or convergence of two neighboring trajectories in the state space. Furthermore, the whole Lyapunov spectrum enables a statement on the presence of hyperchaos, which applies if there are more than one positive Lyapunov exponents and if the Kaplan-Yorke dimension is larger than two. Due to the computational effort required, only the largest exponent or a few of the largest ones have been calculated in most of the existing literature. Knowing of the whole spectrum enables to derive the Ka-

plan-Yorke dimension (see Section 3.3.4). This gives an estimate of the upper bound for the information dimension of the system, which quantifies the complexity of the geometry of the attractor. The state space is divided by classifying the behavior of the system qualitatively. To that end, a Poincaré map P is specified (see Section 3.3.5). The resulting discrete series of intersection points allows for the possibility that the dynamics may be near-periodic. The last investigation here was that of the relationship between system perturbation and system response in terms of synchronization and frequency entrainment, for which the frequency-detuning curves [256] were computed, that is, the difference between the response frequency (characteristic frequency or largest peak in the spectrum) and the stimulus frequency, plotted against the stimulus frequency.

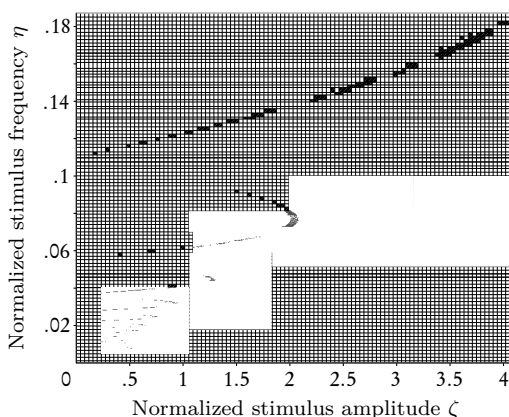


Fig. 5.16. Occurrence of quasi-periodic-behavior forming a two-torus surface in state space. Two-dimensional tori are indicated by two zero Lyapunov exponents (shown in black dots) in the parameter space of stimulus amplitude and frequency. Several parameter regions are shown at a finer resolution of stimulus amplitude and frequency. Note that one obtains the physical values by applying characteristic constants (see, for example, Table 3.3).

5.2.3 Results

For constant input a self-sustained oscillation was found due to a stable LC with a certain intrinsic frequency. Forcing such a LC with periodic input to the NMM accelerates or decelerates the oscillation (dependent on timing) and entrainment effects occur if the sum of impacts is non-zero. Indeed, frequency entrainment is observed, that is, the cortical area responds with the stimulus frequency instead of the intrinsic frequency, thus forming a plateau in the frequency-detuning curves (see Fig. 5.13). The frequency entrainment effect spreads over broader stimulus frequencies for higher stimulus intensities, while away from the entrainment ranges complex behavior, including periodic, quasi-periodic, and chaotic dynamics arise (see Fig. 5.14). The latter behavior, in particular, provides continuous spectra that are commonly observed in M/EEG or LFP data.

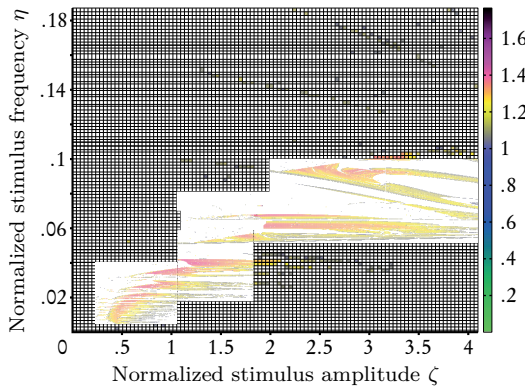


Fig. 5.17. Kaplan-Yorke dimension of the periodically forced Zetterberg-Jansen model in the parameter space. The Kaplan-Yorke dimension given by Eq. (3.29) never goes above 1.7, thus hyperchaos does not exist. Hyperchaos means that the system has more than one positive Lyapunov exponent. Several parameter regions are shown at a finer parameter resolution. Physical units for the parameters can be obtained by applying the characteristic constants (e.g., Table 3.3).

Table 5.2. Dynamic regimes occurring for stimulus amplitude $\zeta = 3.6301$ (which equals 6.48 mV for the characteristic potential according to Jansen and Rit [54]; see Table 3.3). A LC appearing as periodic oscillations is a closed orbit in state space. An invariant torus indicates quasi-periodic oscillations that manifest themselves in the power spectra with peaks at incommensurate frequencies. A strange attractor is a bounded attracting set in which all trajectories are unstable and nearby trajectories locally diverge from each other exponentially, as evidenced by a positive Lyapunov exponent, as well as a broadband power spectrum.

Orbit	Range of normalized stimulus frequency $\times 10^{-2}$
Limit cycle	0 to 18.72
Two-torus	17.72 to 18.72
Strange attractor	5.34 to 6.23; 7 to 7.18; 7.52 to 8.04; 8.92 to 9.29; 10.33 to 11; 11.96 to 17.21

In the cases of periodic and quasi-periodic behavior, power spectra are discrete, where frequencies η_i are commensurable^h in the former and incommensurableⁱ in the latter case.

Chaotic behavior is indicated by non-closed bounded trajectories in state space, broadband continuous spectra and positive Lyapunov exponents (see Fig. 5.15). Here, chaotic regimes arise by traversing a homoclinic Shil'nikov bifurcation (see Fig. 5.12) for non-rational ratios between the frequencies of the stimulation and the intrinsic model kinetics. This route to chaos [80] has also been identified in more theoretical neural models (e. g., [257, 258]). The Lyapunov spectra reveals configurations where the system has two zero Lyapunov exponents and evolves on a two-dimensional invariant torus, indicating quasi- and bi-periodicity (see Fig. 5.16). In general, the model is dissipative (i. e., the sum of Lyapunov exponents is negative) and does not exhibit hyperchaos, as seen from the observation that the second largest Lyapunov exponent is non-positive and the Kaplan-Yorke dimension never goes above

^hi. e., $\sum_i k_i \eta_i = 0$ for some non-zero integers k_i .

ⁱi. e., $\sum_i k_i \eta_i \neq 0$ for any set of non-zero integers k_i .

1.7 (see Fig. 5.17). The periodic forcing seems to work mostly in the direction of entrainment, and although there are occasional islands of chaotic regimes, the regular forcing does not let the dynamics become exceedingly chaotic.

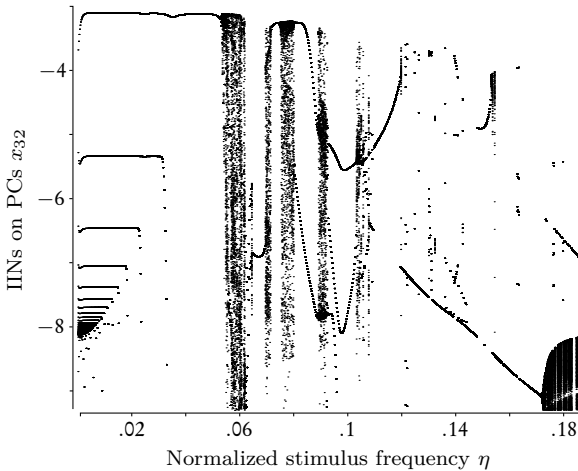


Fig. 5.18. Bifurcation diagram for stimulus amplitude $\zeta = 3.6301$. The vertical axis is the effect of inhibitory interneurons on pyramidal cells x_{32} that is the coordinate of the intersection points (black dots) of trajectories with the Poincaré hyperplane after discarding initial transients. The horizontal axis is the stimulus frequency. Periodic regimes exist, for instance, for frequencies ranging from 0 to 5.34×10^{-2} . Chaotic and quasi-periodic regimes occur, for example for frequencies ranging from 5.3×10^{-2} to 6.23×10^{-2} (scattered dots) and between 17.21 and 18.72. The classification can be taken from Table 5.2. Note that one obtains the physical values by applying characteristic constants (see, for example, Table 3.3).

6 Resonance Phenomena

*Think of the wonderful circles in which our whole being moves
and from which we cannot escape no matter how we try.
The circler circles in these circles.*

E.T.A. Hoffmann, 1776–1822

Electrophysiological measurements such as M/EEG, LFP or single unit recordings contain rich information, which may be related to specific cognitive processes, to general brain states, or to certain pathological conditions. For example, it is known that stimulation by repetitive light flashes entrains the alpha EEG rhythm (i.e., frequency entrainment). Neurons in the human visual cortex synchronize their firing to the frequency of flickering light, causing the EEG alpha frequency to change toward the stimulation frequency [83–85]. Clinically, this resonance effect is called photic driving. The occurrence of such an effect is an indicator of functional flexibility of the cortex and thus a sign of healthiness. Photic driving is widely used as an activation method in clinical practice, for instance, for diagnosis of epilepsy, migraine, schizophrenia, or depression [86–88].

In order to gain further insight into mechanisms underlying such brain resonance effects and their relevance to brain function and pathology, as well as to make predictions concerning the stimulation parameters, generative models can be used. In this chapter, the model used is a

modified Zetterberg-Jansen version, and the part of the brain modeled is a cortical area. The aim is to describe the frequency entrainment effect of a photic driving experiment very similar to the standard experiment in clinical practice.

In the photic driving experiment one has to consider rhythmic input. The model's response to such input is also of great importance in many other contexts, since, in the brain, such local neuronal circuits are embedded in global brain networks and may experience high amplitude time-varying input from other parts of the brain. Because neuronal ensembles tend to oscillate intrinsically, such input is very often periodic, as evidenced by the widespread occurrence of rhythmic activity in both extracranial and intracranial recordings [81].

In the present instance, the output of the periodically forced NMM (see Section 5.2) was fitted to data from a photic driving experiment, in each case in terms of the largest Lyapunov exponent, which measures the exponential separation or convergence of nearby trajectories, and in terms of frequency detuning. In this way, the NMM proved to be a suitable model for the dynamics of brain resonance phenomena and it was demonstrated that useful predictions concerning the parameter choice of entrainment experiments can be derived from the model.

6.1 Experimental Data

The experimental data used has been obtained by performing a photic driving experiment that was adapted to the individual alpha frequencies of the ten subjects (mean age 28.8 ± 5.81 years, five men; five women). The data has been published by Schwab and colleagues [82], whose aim was the quantification of the frequency entrainment in the alpha rhythm that was most effective at frequencies around individual alpha and half alpha. The measured individual alpha frequency ranged from 9.5 Hz to 11.8 Hz. For each proband, one EEG channel located in the occipital region (electrode O1 in the 10-20 system) was examined.

From the time series, the calculated 15 largest Lyapunov exponents initially turned out to be all positive due to the noise characteristics of the experimental data, unlike those that were calculated from the model. This problem was obviated by a suitable transformation of the exponents, as described in the section below.

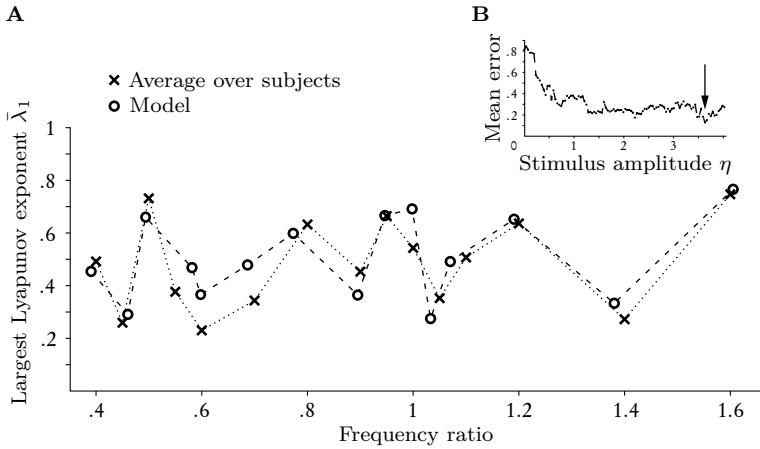


Fig. 6.1. Comparison of model and data from the photic driving experiment. Jansen's characteristic mean membrane potential u_c is applied for the model (see Table 3.3). The largest Lyapunov exponents calculated from the model show very good agreement with those obtained from experimental time series. **A** Lyapunov exponents of the model (nearest neighbors), normalized between zero and one, and the data (average over subjects) plotted against the frequency ratio (i.e., flicker frequency/intrinsic frequency), for the stimulus amplitude ζ that fits best ($\zeta = 3.6301$). The comparison based on the mean differences between (normalized) largest Lyapunov exponents of model and data, averaged over frequencies as function of stimulus amplitude of the model as shown in **B**, where the amplitude that fits best is indicated by the arrow (see also Fig. 5.15). For more details, see Section 6.3. The best fitting amplitude is consistent over subjects as shown in Table 6.1.

6.2 Periodically Forced Model

To model the frequency entrainment phenomenon in photic driving experiments the system used was the periodically forced NMM (of a cortical area) presented in Section 5.2. The periodic input is a continuous time function approximating a periodic train of pulses. In this continuous function each single pulse is similar (but not equal) to the single event used by Jansen and Rit for eliciting visual evoked potentials [53, 54], or used in dynamic causal modeling (e. g., [50, 66]). Both amplitude and frequency of the stimulation were systematically varied within the effective ranges (see Section 4.2).

6.3 Comparison

To establish the level of agreement between model and experimental data, the largest Lyapunov exponents λ_1 was compared, normalized between zero and one by the transformation $a + b \lambda_1$. The scaling of the Lyapunov exponents λ_1 by b entails a temporal scaling and hence a scaling of the stimulus frequency, since λ_1 is a rate. The offset of the Lyapunov exponents a can be regarded as a multiplicative process P of divergence $V_1(\kappa)$, because $|V_1(\kappa)| \approx P_1 \exp(b \kappa \lambda_1)$ with $P_1 = \exp(a)$. Background activities and more general unspecified processes may be included in P . Since the sampling ratio (on the frequency axis) is 4.6 between the model (69 samples) and the experimental data (15 samples), an experimental data point was compared with the four nearest neighbors in the model. The minimum of the four Euclidean distances divided by the maximum possible distance was computed, the result was averaged over stimulus frequency (mean error), and the minimum of the mean distances across the stimulus amplitudes was determined. In contrast to the experimental design, the model uses the stimulus amplitude as a parameter in addition to the stimulus frequency. The amplitude for which the model best fits the data was identified.

Table 6.1. Single subject comparisons fit the model at stimulus amplitude around of approximately 3.6 with errors around 0.2. For the median and mean of largest Lyapunov exponents across subjects, the model fits at stimulus amplitude of 3.63 with an error of 0.13. The calculation is described in Section 6.3.

Subject	Normalized amplitude	Mean error in %
1	3.67	19
2	3.67	22
3	2.89	30
4	3.67	17
5	3.67	16
6	3.47	22
7	2.34	26
8	3.67	23
9	3.67	20
10	3.67	22

6.4 Results

The model is indeed able to explain frequency entrainment that is observable during the photic driving (see also [82–84]). Comparing the model outcome with the experimental data (see Section 6.2 and Fig. 3.2 for experimental paradigm), a particular amplitude of the stimulus for the model (uncontrolled by the experimental design) was found, where, for all subjects, the Lyapunov exponents were consistently in close agreement between the experiment and the model (Fig. 6.1 and Table 6.1). A flat region occurs in Fig. 6.1 (B) due to the relatively constant pattern of the model’s largest Lyapunov exponents for amplitudes between 1.5 and 3 (see Fig. 5.15). However, there is a clear minimum for stimulus amplitudes around 3.6, also consistent over subjects (see Fig. 6.1 and Table 6.1). For the corresponding model configuration, a compact representation in Fig. 5.18 is shown where the system states is described qualitatively in Table 5.2.

7 Discussion and Conclusion

*A point of view can be a dangerous luxury
when substituted for insight and understanding.*

Marshall McLuhan, 1911–1980

The approximations inherent in the Zetterberg-Jansen model are briefly discussed in Section 7.1. The regimes of the modified Zetterberg-Jansen model (see Chapter 4) in response to constant extrinsic input levels on all neural masses (NMs) and intrinsic temporal ratios are discussed in Section 7.2. The identified underlying mechanisms of the system states, the classification of limit cycle branches (LC-branches) thereof and the description of ordered sequences are discussed with respect to phenomena observable with magnetoencephalography and electroencephalography (MEG and EEG) in normal and diseased brain. The complex dynamics like chaotic behavior of the periodically forced modified Zetterberg-Jansen model as function of stimulus amplitude and frequency are discussed in Section 7.3. The occurrence of complex behavior is discussed, and particularly the chaotic behavior is interpreted with respect to the characteristics of electrophysiological measurements. Finally, the successful application of the periodically forced modified Zetterberg-Jansen model to EEG data from a clinically relevant photic driving experiment is discussed in Section 7.4.1 in terms of the comparison and the resulting predictions.

7.1 Zetterberg-Jansen Model

In this piece of work the Zetterberg-Jansen model was modified and analyzed that is widely used for explaining such electrophysiological measurements as EEG and MEG. This neural mass model (NMM) represents a mean field model describing the mean activity of a neural ensemble (e.g., a cortical area). Particularly, it describes the mean firing rates and the mean postsynaptic potentials (PSPs) instead of membrane potentials or such single events as action potentials that can be described by single neuron models such as the Hodgkin-Huxley model [60] or the Izhikevich's simple spiking neuron model [259]. In contrast to ensemble density models where neuronal states are generally expressed by probability densities [129, 130, 134], in a mean-field model, simply the potential-to-rate conversion (e.g., sigmoid function) incorporates variability within a neural ensemble [140, 141]. Furthermore, the Zetterberg-Jansen model used here consists of point-like NMs, meaning without any spatial information as used, for instance, in neural field models (e.g., [57, 126, 142, 154, 157]). Thus, in this work, a single source was described by an elementary circuit of three interacting NMs of pyramidal cells (PCs), excitatory and inhibitory interneurons (EINs and IINs) according to Zetterberg and colleagues [58] and Jansen and colleagues [53, 54]. More complex structures are conceivable, for example, as used in the Haeusler-Maass model [260] or based on the work of Thomson and Bannister [145], which could be reduced to the simple structure of a positive and a negative feedback loop as used here. However, the major advantage of the Zetterberg-Jansen NMM is that the model is parsimonious by means of parameters, thus mathematically tractable and still plausible for the description of such electrophysiological measurements as M/EEG. For this reason, the modified Zetterberg-Jansen model and networks thereof are suitable for parameter studies and for system inversions (e.g., such Bayesian techniques as 'dynamic causal modeling') of given data like that of M/EEG [50, 67, 74].

7.2 Constantly Forced Model

The bifurcation study is a detailed analysis of the dynamic properties of a NMM for a single cortical area. The model is based on the well-known proposal of Zetterberg and colleagues [58] and Jansen and colleagues [53, 54] and has been extended by incorporating extrinsic inputs from other cortical and subcortical areas on the INs. By means of bifurcation diagrams, the system's behavior was investigated as a function of its key parameters, which are the extrinsic input levels to all three NMs and the dendritic time constants for excitatory as well as inhibitory synaptic contacts. Finite effective ranges were determined for these parameters (Table 4.1). It can be argued that variations of the extrinsic input levels are equivalent to variations of the firing thresholds and, under certain conditions (see Section 5.1.1), to variations of the intrinsic connection strengths between the NMs, and that therefore the analysis also accounts for the influence of these parameters. Consequently, the analysis can be considered complete.

7.2.1 States and the Underlying Mechanisms

One aim of the model analysis was to describe the rich dynamics observed in a systematic way. At the lowest level, three principal types of steady state behavior were identified with respect to the PC's PSPs. First, stable foci and nodes produce constant output, which, under small perturbation (e. g., noisy input to the PCs), changes into filtered noise with oscillatory components in the case of foci, or without such components. Second, supercritical Andronov-Hopf bifurcations (AH-bifurcations) give rise to stable limit cycles (LCs). They appear gradually upon passage of the bifurcation. For the standard Jansen and Rit parameters [54] (also see Table 3.3) their frequency is relatively insensitive with respect to the level of extrinsic input, and ranges between 0 Hz and 80 Hz, depending on the applied intrinsic temporal ratio (as justified in Section 5.1.1), or the dendritic time constants (see Fig. 5.8). For noisy

input, this results in waxing and waning harmonic oscillations of relatively stable frequency. This pattern is compatible with typical brain rhythms, such as the alpha rhythm or sleep spindles. Third, global bifurcations, for example of Shil'nikov type, give rise to homoclinic LCs appearing suddenly at high amplitude and low frequency. They are generally not harmonic, but have a spike-like appearance (anharmonic oscillation). Their frequency depends a great deal on the input levels. Hence, if the PCs receive fluctuating input, the intervals between the wave peaks (or spikes) are variable. These phenomena are compatible with the hallmark of epileptic seizures (i.e., suddenly occurring, irregular spiking patterns (see, for example, [64, 65, 76–78])). It should be noted that Shil'nikov's bifurcations were also related to "spike-wave" behavior in more theoretical models on MEG and EEG (e.g., [258]). Indeed, this relationship has been also identified in others experimental analysis of using embedding methods (e.g., [261]).

7.2.2 Classification of LC-Branches

The topology of the bifurcation diagrams is used to characterize the occurrence of the various neuronal states and the transitions between them as a function of extrinsic inputs. This means that one can read these transitions directly from the bifurcation diagrams. Numerous branches of LCs were found, which are potentially of biological interest and which admit a sudden entry into orbit or smooth transition between different LC-regimes by virtue of small variations in extrinsic inputs (Fig. 5.1 and Figs. 5.9 to 5.12). These effects were either reversible or irreversible, depending on the parameters and the initial state of the system. As the parameters moved through the effective parameter space, two quantitative changes were observed, that is, in the precise location of the bifurcations and LCs as well as qualitative changes of the entire topology of the bifurcation diagram (e.g., bifurcations appearing or disappearing).

Consequently, at another level of description, a classification was

introduced, observing principal types of system topology made up of globally stable LC-branches (see Fig. 5.3). By using this classification scheme, the complexity of the dynamic behavior was reduced to a few basic phenomena existing in isolation or in combination. This allowed to map these topologies to the parameter space and draw a number of global conclusions about the frequency of occurrence and conditions for the existence of these topologies (see Fig. 5.4 and Fig. 5.5) and of the associated oscillatory regimes (see Fig. 5.6 and Fig. 5.7).

The systematic analysis revealed that the dynamic behavior (I-B and II-AA topology) of the specific parameter configuration proposed by Jansen and Rit [54], as reported by the analysis of Grimbert and Faugeras [189], is an exception rather than the rule with respect to the effective parameter space of the extended model (see Fig. 5.4 and Fig. 5.5). Hence, the general validity of any analysis based on that configuration would depend on the assumption that the parameter set put forward by Jansen and Rit [54] is adequate within quite narrow bounds (see Fig. 5.4 and Fig. 5.5, branch type AA-B). Furthermore, a bifurcation was found which was not reported by Grimbert and Faugeras [189].

There were several general findings concerning the dynamics of the system. First, harmonic oscillations arising from two AH-bifurcations (II-AA type) are by far the most common oscillatory behavior over the entire parameter space (Figs. 5.4 and 5.5 and 5.8). This finding is compatible with the widespread presence of relatively frequency-stable rhythms in brain signals (delta, alpha, beta, and gamma frequency band). Anharmonic oscillatory regimes (e.g., in branch type I-B and II-BB, see Fig. 5.2 for classification, or the examples in Fig. 5.1 and Figs. 5.9 to 5.11) are thus special and exceptional, but nonetheless very interesting cases for modeling, for example, pathological states (e.g., epilepsy, Figs. 5.4 to 5.7).

Second, the analysis revealed that the intrinsic temporal ratio β between the inhibitory and excitatory dendritic time constants τ_i and τ_e (not their absolute values) determines whether no oscillations, only one

type of oscillation (harmonic or anharmonic) or both types are possible (Fig. 5.4; this confirms the findings of David and Friston [48]). Regarding the system Eqs. (4.1) to (4.7), it is obvious that the dendritic time constants are related to each other by their scaling or respectively the intrinsic temporal ratio $\beta = \tau_c/\tau_i$. Hence, the system behavior qualitatively depends only on the intrinsic temporal ratio β and on the extrinsic inputs on both types of interneurons (i.e., EINs and IINs). More specifically, this analysis revealed that for maintaining an oscillatory regime, it is essential to keep the ratio $\beta \leq 5$ (see Fig. 5.6).

Third, the analysis showed that the system is more sensitive to extrinsic inputs to IINs than to extrinsic inputs to EINs. Since oscillations in local neuronal circuits depend fundamentally on effective inhibitory feedback loops, extrinsically inhibited IINs prevent the system from oscillating, while moderate extrinsic excitation of IINs causes local neuronal circuits to oscillate. Extrinsic inputs to EINs predominantly influence the spiking behavior of the system (see Fig. 5.7).

7.2.3 Ordered Sequences

Besides the two aspects already discussed, another aim of this study was to demonstrate that it is possible, using bifurcation diagrams, to describe ordered sequences of qualitatively different regimes by NMMs. Generally, such sequences arise when the parameter space is slowly traversed, as compared to the time constants of the oscillations involved. Such slow parameter changes could be associated with numerous neurobiological phenomena, such as changes in attention and vigilance, progression of disease, effects of medication or changes in sleep stage.

For example, the rapid transition between non-REM and REM sleep^a accompanied by both drastic changes in rhythmic EEG patterns and numerous functional phenomena has been modeled as phase transition of a NMM very similar to ours, caused by slow parametric changes due

^aREM sleep is a sleep phase of rapid eye movements (REM).

to biochemical processes (i. e., changing acetylcholine and adenosine levels) [79]. Another prominent example, where modelers have exploited slow transitions across a bifurcation, is an epileptic seizure. Such a seizure is characterized by the transition from normal EEG dominated by harmonic alpha or beta oscillations to high amplitude irregular spike or spike-wave oscillations [65, 76–78]. A further example is the EEG observed over the motor cortex during brisk finger movements, where the brain dynamics change from dominant alpha to increased gamma oscillations during the preparation phase and then to increased beta oscillations shortly after the movement itself. Finally, after a few seconds, the system relapses into its normal state [262].

The topologies of LC-branches in bifurcation diagrams may be used to describe the formation of such sequences. For instance, Fig. 5.12 (see Section 5.1.3 for a detailed description) shows how a gradual increase in extrinsic inhibition by means of excitatory input to the IINs can suddenly move the system from normal M/EEG featuring alpha waves to high amplitude irregular spiking.

A number of topologies were found where the system is constrained to undergo a specific ordered sequence of dynamic states in order to recover its initial state after having been perturbed by a transient change of a system parameter. For instance, in Fig. 5.10, the system first jumps to a state where it produces anharmonic oscillations after a transient increase in the extrinsic input to the PCs. Interestingly, the system will remain in this state even after the input has returned to its original level. The system will only return to its initial state when a transient decrease of sufficient amplitude occurs in the extrinsic input to the PCs. This could be a model, for example, for the elicitation of epileptic seizures by sudden, unexpected stimuli (startle epilepsy). In other configurations, a return to the initial state is impossible (irreversible processes). For instance, Fig. 5.9 shows the topology of encapsulated II-AA branches. When the normal state (inside the unstable AH-LCs) is perturbed slightly (i. e., below threshold), the system produces damped

oscillations, but after passing the threshold (i. e., the unstable AH-LCs) the system is unable to return to its initial state.

These examples (see Section 5.1.3 for further details) demonstrate that a multitude of biologically interesting dynamic phenomena in brain signals can be modeled by a rather simple NMM of a single cortical area in conjunction with appropriate input trajectories. The systematic analysis details the parameter configurations and input trajectories that can be used to model specific changes between different dynamic states.

7.2.4 Transitions Between Regimes

As argued here, bifurcation theory is a powerful tool for modeling M/EEG data. However, they can also be a nuisance when the aim is the modelling of a single dynamic regime. For example, if one wants to model stable oscillations, the parameterization should be placed distant from a bifurcation to avoid a transition under slightly varied parameters. The identification of *safe placements* in parameter space is another use of the bifurcation analysis. As shown, some dynamic regimes exist which seem to be quite narrow islands in parameter space (see, for example, Fig. 5.4 for branch type combinations: e. g., AA-AB which is restricted to narrow bands of intrinsic temporal ratios β of either about 0.76 to 0.78, corresponding to the example in Fig. 5.9, or about 0.16 to 0.18, corresponding to the example in Fig. 5.10). Such configurations in the parameter space may be exploited for transitions between dynamic regimes but should, in contrast, be avoided for modeling dynamics which are meant to be robust against slight perturbations.

7.2.5 Modeling

The analysis dealt solely with a local model for a single cortical area. The question arises, whether and under what conditions the results can be generalized to the case of several interacting local neuronal circuits. The results directly predict the behavior of networks consisting of local

units under the assumption of weak and/or slowly varying extrinsic inputs (relative to the dendritic time constants of the local neuronal circuit). If this is not the case, for example, if several cortical areas have relatively strong bidirectional coupling, more complex state spaces would have to be explored. However, given the effective ranges of the inputs to a single cortical area, one can also determine the ranges for the connection strengths between cortical areas. This means that the local neuronal circuits greatly limit the behavior of the entire network. In order to keep a large network in an operating state, connections between interacting brain areas must not exceed these effective ranges. This implies the presence of regulatory mechanisms such as neurotransmitter receptor adaption [197, 214], synaptic plasticity [48, 197, 214] or back-propagating action potentials into the dendritic tree [214].

The results enable the efficient definition of prior distributions of parameters in Bayesian model inversion, as used in dynamic causal modeling [50, 67]. To model specific phenomena using dynamic causal modeling, the researcher would first select specific regimes of parameters, informed by the present bifurcation analysis. By using appropriate prior distribution centered on the selected parameter configuration, the researcher can then constrain the effective ranges for the extrinsic input levels and inter-area connection strengths. Additionally, the initial value problem of the gradient-ascent estimation scheme used by dynamic causal modeling can be addressed by providing the inversion scheme with information on qualitatively different dynamic regimes. In principle, this would enable users of the dynamic causal modeling approach to identify more effectively global maxima of the objective function by starting the inversion process repeatedly in qualitatively different dynamic regimes.

7.2.6 Links to Neuroscience

NMM dynamics account for coherent activity of large numbers of neurons, which is exactly the kind of phenomenon that gives is susceptible

of EEG and MEG. The signals recorded by these methods are known to reflect important aspects of brain function. In particular, it has been shown that oscillatory activity observed using M/EEG bears a strong relationship to brain function in both health and disease. Widespread brain oscillations reflect the cortical arousal state, as they seem to be associated with the alpha-rhythm (8 Hz to 12 Hz) in the visual cortex (see, for example, [263], the mu-rhythm (≈ 10 Hz and ≈ 20 Hz) in the somatomotor cortex [264–266], and the tau-rhythm (8 Hz to 12 Hz) in the auditory cortex [267]. Such rhythms are selectively suppressed by primary sensory or motor activity [262]. Other brain rhythms are directly related to active processes. For example, frontal beta-rhythms (≈ 20 Hz) are associated with motor activity [262, 267, 268], hippocampal theta-rhythms (4 Hz to 8 Hz) in various parts of the brain play an important role for memory functions as do gamma-rhythms (30 Hz to 80 Hz) [263, 269–273, 273–276], and gamma-rhythms appear to reflect processes of perceptual binding in the visual [277–280] and auditory domains [281–283]. Pathological brain function is strongly correlated with typical brain oscillations, for example in epilepsy during seizures [284] and in Parkinson’s disease [285–287]. This relevance of oscillatory M/EEG phenomena for brain function corroborates the view that modeling neural mass action is important for the understanding of brain function and the organization of behavior [4, 49, 114]. It is worth mentioning that with realistic choices of the system parameters, the present modified Zetteberg-Jansen model of a single cortical area (Eqs. (4.1) to (4.7)) generates a range of frequencies covering most of the reported functionally relevant M/EEG rhythms.

Moreover, as discussed above, many functional processes in the brain can be described as a succession of distinct functional states, mirrored by specific oscillatory regimes observed in experimental M/EEG data. Often, this succession of states seems to be caused by a gradual evolution of certain system parameters. For example, during sleep, slowly decreasing levels of adenosine and other somnogens cause a steady down-

ward shift in resting potential (equivalent to shift in extrinsic input level, see Section 5.1.1), while acetylcholine levels, raising the excitability of excitatory neurons and decreasing the gain of excitatory synapses, perform slow (≈ 90 min) cycles. These slow biochemical trajectories are believed to be responsible for the repetitive transition between slow wave and REM sleep phases [79, 288]. It was shown that bifurcation analysis provides a generative model for exactly this type of phenomenon: gradually changing parameters lead to a sequence of distinct dynamic regimes with relatively rapid transitions between them.

7.3 Periodically Forced Model

In Section 5.2 the behavior of the periodically forced modified Zetterberg-Jansen model [53, 54, 58] are analyzed as a function of amplitude and frequency of a periodic stimulus within biologically plausible ranges. The investigated system exhibits interesting and complex dynamics, including chaos.

7.3.1 Complex Behavior

In simulations, the dynamics of the periodically forced modified Zetterberg-Jansen model feature a rich mosaic of complex behaviors (see Fig. 5.14). From the parameter space analysis presented in Fig. 5.15, it can be seen that both flicker intensity and frequency are critical parameters. As expected on theoretical grounds [256, 289], the state space analysis reveals that the system is entrained by the stimulus frequency (see Fig. 5.13), where the entrainment regions (i. e., plateaus in the frequency-detuning curve) around the intrinsic frequency become wider with increasing stimulus intensity (results not shown). In regions of the parameter space without entrainment, complicated interaction between stimulus and intrinsic kinetics leads to periodic, quasi-periodic, and chaotic behavior, as, for example, indicated by largest Lyapunov

exponents and the Kaplan-Yorke dimension. Areas with different dynamic behavior form fractal structures in parameter space (Figs. 5.15 to 5.17), so that rhythmic and chaotic brain states are found virtually next to each other and even small parameter changes can give rise to a switch from one to another.

7.3.2 Chaos in the Brain?

The Zetterberg-Jansen model investigated here describes complex, partially chaotic, dynamics at the mesoscopic spatial scale, which captures mass action of neural ensembles [4]. Chaotic dynamical regimes have been shown before in mesoscopic models of the cortex [290, 291] and of the olfactory bulb (e. g., [123]). Concerning the brain, there is evidence for chaotic behavior at different hierarchical levels, from single neurons to entire neural ensembles [104]. A suitable means to access neural activity experimentally at the mesoscopic level is provided by M/EEG, which records the summed activity of 10^5 to 10^9 , mainly cortical, neurons [12, 13]. M/EEG data describe high-dimensional, noisy, nonlinear, and non-autonomous processes [292], which render it difficult to distinguish between stochastic and complex deterministic processes like deterministic chaos. Accordingly, although there is some evidence for chaos in such data (e. g., in epilepsy), the issue remains controversial (for a discussion see [293] and the references cited therein). However, irrespective of whether the complexity of M/EEG fulfils the exact mathematical criteria of deterministic chaos, the parsimonious NMM, as shown here, helps to better describe the dynamics of such data and the underlying brain processes.

Apart from brain rhythms in characteristic frequency bands (e. g., the alpha rhythm), complex behavior with noise-like characteristics causes the continuous spectral components in these data. This can be interpreted as filtered noise (e. g., stochastic sensory input) or described by nonlinear deterministic processes. It was shown that periodically driven NMMs may explain the continuous spectral components of M/EEG

without having to consider noisy input processes. Other NMM studies often apply a stochastic input process with the effect that the spectra are more realistically widened around an intrinsic frequency of interest (e.g., alpha band) (e.g., [48, 54, 65, 69]). It is, however, an advantage if these continuous spectral components can be modeled and controlled as intrinsic phenomena of neuronal circuits, because there is evidence that broad spectral components, also, are modulated by cognitive processes and that their generative processes thus play a role in information processing (e.g., [294–296]). This is corroborated by the postulated prominent role of chaos in information processing (e.g., [104, 123]).

7.3.3 Ordered Sequences

The complex behavior could be used to explain multi-stability and ordered sequences in M/EEG data, which can be observed, for example, in perception (e.g., mono- and binocular rivalry [297], Necker-cube illusion), stages of sleep [298, 299], changes in attention or vigilance, learning and training such as odor recognition [300, 301], progression of disease such as epilepsy [302–305], and effects of medication. State transitions or multi-stabilities appear since the brain is subjected to multiple high-dimensional stimuli from both exogenous (e.g., visual or haptic) and endogenous processes (e.g., endocrine or circulatory system), and is sensitively dependent on the current individual state (that of vigilance, for instance – sleep or attention). For example, one can interpret the quasi-periodic behavior in Fig. 5.14 as multi-stability. However, the orbits are sensitive to noise, in terms of fine structure and the associated sequences, rather than the overall structure. One way to achieve ordered sequences of dynamic regimes that are sufficiently robust against noise is to adequately change the state space through parameter changes that are slower than the state dynamics, so as to produce a temporal hierarchy [51]. Parameter dynamics could be described, for instance, by metabolic processes (which are usually slow) and/or more artificially by stable heteroclinic channels (e.g., [306, 307]).

Complex behavior like entrainment, chaos, periodic and quasi-periodic motion were found in a periodically forced modified Zetterberg-Jansen model of a single cortical area, for plausible parameter ranges without regard to noise processes. Such dynamics are observable in brain data and are relevant for the explanation of brain function.

7.4 Brain Resonance Phenomena

It is an important result of this piece of work that, the periodically forced modified Zetterberg-Jansen model of a cortical area (see Section 5.2) is able to account for the dynamics of a photic driving experiment (see Section 6). Photic driving probes the resonance behavior of the brain and is of great importance for the assessment of epilepsy, migraine, schizophrenia or depression in clinical practice [86–88]. In this paradigm, the dominant brain rhythm during rest (alpha: ≈ 10 Hz), is entrained by the periodic stimulus (see Sections 3.4 and 6).

7.4.1 Periodically Forced Oscillator

The concept of a periodically forced oscillator to the modeling of brain resonance effects was applied. In the brain, such periodic input might be that for rhythmic stimulation of the brain, such as in the photic driving paradigm, or of the output from other oscillating brain areas. Such coupling between (oscillating) processes inside and outside the brain has been discussed as important for the processing of information (e.g., [105, 286, 308–310]). The dominant intrinsic brain rhythm was described by performing a self-sustained oscillation with the NMM, generated by an AH-bifurcation (see Section 5.1 or [51]). Applying periodic input to an oscillating system will generally accelerate or decelerate its intrinsic rhythm, provided the sum of impacts (acceleration and deceleration) is non-zero over time [289]. The more intense the periodic stimulus is, the more it takes over the states of the system (i.e., the states follow the stimulus with a constant phase shift) and, finally,

the largest Lyapunov exponent approaches zero, meaning the intrinsic oscillation has been eliminated. In this limiting and potentially pathological case, the neuronal circuit is regarded as passive filter, that is, a conservative system. At the other extreme, that is, where stimulus intensity approaches zero, what is found is an autonomous system with respect to the outside world. These two cases are not treated here because they are not physiologically relevant. In the model, both cases are avoided due to the nonlinearity (i.e., sigmoidal potential-to-rate conversion) that saturates the impact of extrinsic inputs for stimulus intensities at the edge and outside of the specific effective ranges (see Table 4.1). Resonance phenomena like frequency entrainment in photic driving experiments are explicable in these terms. It is reasonable to expect that the dynamics of the system depend on timing (the ratio between stimulus and intrinsic frequencies) and intensity of stimulation.

7.4.2 Comparison

Strikingly, the characteristic patterns of unpredictability generated by the modified Zetterberg-Jansen model here presented (see Section 7.3.1 for a discussion) were also to be found in the experimental data at a reasonable level of accuracy (see Fig. 6.1). A particular stimulus amplitude was identified, where, for all subjects, the Lyapunov exponents are in close agreement between experiment and model (Fig. 6.1 and Table 6.1). The intensity that best fits the experimental data is located in the upper portion of the effective range for exciting IINs.

7.4.3 Predictions

Consequently, it is envisaged that a decrease of stimulus intensity in photic driving experiments would shrink the ranges of frequency entrainment (i.e., the plateaus in the frequency-detuning curve) and an increase would broaden them. The model also predicts that saturation effects start to become important at approximately 1.3 times the cur-

rently applied stimulus intensity and for intensities close to zero. A stimulus increase between 1 and 1.3 times the current intensity could be expected to lead to an improved entrainment effect (i.e., broadened range). As a consequence, photic driving experiments focusing on brain resonances should be extended by varying the stimulus intensities in general, in order to assess brain flexibility more precisely. Thus, challenges for future experimenters will involve estimation and systematic manipulation of the stimulus intensity.

7.5 Future Directions

The mean-field model, namely the Zetterberg-Jansen model that is modified and studied in this work, could be applied to other experimental data using periodic stimuli such as auditory stimuli (e.g., [89]). One could also use it to describe and distinguish the effects of stimulus habituation (e.g., [311, 312]) and synchronization (for instance, applying it to such experimental data as that in [286]). The concept of coupled oscillators leads to the conclusion that the process of habituation is independent of stimulus timing and that the synchronization process is sensitive to stimulus timing. For the purpose of distinguishing between these two effects, the transients after stimulus onset should be considered rather than the long-term (stable) states reached after several periods of stimulation.

In order to accommodate to the single-trials of such experiments one could modify the Bayesian inference scheme of dynamic causal modeling that is widely used in association with NMMs. For this purpose it would be possible to use the results of this research, especially the bifurcation diagrams (e.g., Fig. 5.1 and Figs. 5.9 to 5.11) and the state classifications (Figs. 5.5 to 5.7) to specify a-priori parameter distributions, for a single cortical area model, at least.

One could specify a network to study by using such measurements as those in functional magnetic resonance imaging (functional MRI). In

addition to its applicability to EEG and MEG, the Zetterberg-Jansen model is capable of explaining functional MRI data by applying a more complex observer model system (see Section 2.2) than those currently need for M/EEG such as the familiar balloon model [313].

From a hierarchical perspective of information processing in terms of bottom-up, top-down and lateral processes (e.g., [308,314,315]) the modified Zetterberg-Jansen model describes sensory processing at a higher level. In order to deal directly with the external stimulus instead of cortical input the active bottom-up processing (e.g., filtering or relaying) of sensory stimuli (e.g., periodic auditory or visual stimulus) should be considered. One way is to incorporate subcortical instances of primary sensory processing like the thalamus into the modeling framework in addition to the Zetterberg-Jansen circuit.

To restrict the complexity of such a system, one could incorporate a mean-field model, for example, of the thalamus as developed by Lopes da Silva [55] or Robinson [162], achieving parsimonious forced network of two reciprocally connected oscillators representing a KIII set using Freeman's terminology (see Section 2.4.2). Thalamus and cortex are able to auto-oscillate and the thalamocortical circuit is itself also able to oscillate through the thalamocortical projections, forming a loop.

However, this work with its model of a single area model reveals that a network composed of modified Zetterberg-Jansen models may contain redundancy, particularly when a single Zetterberg-Jansen node is forced (by stimuli or notes from the same or from other networks) at the edge of or beyond the effective extrinsic input ranges (see Table 4.1). Here, redundancy means that saturated nodes do not participate in processing information within the network. The Zetterberg-Jansen model is self-sustained in terms of the intrinsic dynamics (e.g., rhythms) but relatively stiff as a means of processing information within a network.

This problem of redundancy through saturation can be tackled by incorporating plasticity mechanisms into the NMM (e.g., [214]). These mechanisms could be, for example, variation of synaptic scaling factors

or a changing transfer function depending on the previous action of the NM (e. g., by applying Hebb's rule [316]).

The basic assumption behind such an approach is that a neural ensemble tends to operate in a mode of information processing. Saturations or the related redundancies are balanced over time to some extent by reconnecting and disconnecting or degeneration of nodes. Such plasticity effects have been well studied at the microscopic level of molecules: synapses up to neurons (e. g., [109, 317]). However, they still present an open question for ensembles at the mesoscopic level or large-scale networks at the macroscopic level. There are certain mean-field models which address this issue (e. g., [126, 211, 214]). One of the cruxes is the inverse problem at these levels of observation, because the measured processes are usually hidden and diverse [4, 27].

7.6 Conclusion

In this work, it has been shown that the Zetterberg-Jansen model is capable of producing biologically relevant kinetics, especially rhythms, under constant as well as periodic extrinsic input forces. The present work presents a complete account of the dynamics of the constantly forced NMM, of which, so far, only one special parameter set had been investigated [189]. It is shown as a consequence in a clinically relevant photic driving experiment that a periodically forced modified Zetterberg-Jansen model can explain complex phenomena.

The model is systematically analyzed as a function of constant extrinsic input and intrinsic temporal ratio and as a function of amplitude and frequency of periodic extrinsic input. The mechanisms underlying certain dynamics (rhythms for instance) are identified. The author goes on to describe the dynamic richness of the system using a relatively small set of prototypical system topologies and from this draws general conclusions about the phenomena of particular interest and their conditions of existence. Moreover, biologically relevant configurations are

identified that demonstrate how reversible and irreversible transitions between different oscillatory regimes, which can be observed in M/EEG, can be explained by smooth changes in the extrinsic inputs. Generative models for ordered sequences of dynamic phenomena are obtained which may be used as models of transitions between qualitatively different brain states, caused by slow changes in parameters.

It was possible with a modified Zetterberg-Jansen model to reproduce the phenomena or, more precisely, the frequency entrainment effect in a photic driving experiment, and to match the largest Lyapunov characteristic exponents. Predictions are made using the model as to the outcome in situations with patients and probands if they are subjected to periodic stimulation in similar resonance experiments.

A Appendix

*Le savant n'étudie pas la nature parce que cela est utile;
il l'étudie parce qu'il y prend plaisir,
et il y prend plaisir parce qu'elle est belle.*

Henri Poincaré, 1854–1912

A.1 Characteristics of the Sigmoid

The sigmoid function (3.16) is steadily differentiable, increasing asymptotically towards unity (i.e., $\lim_{x_j \rightarrow +\infty} S_j(x_j) = 1$) and decreasing asymptotically towards zero (i.e., $\lim_{x_j \rightarrow -\infty} S_j(x_j) = 0$). Hence, the function has at least one point of inflection. The slope at the inflection point can be derived from the properties of the function. The first three derivatives of the sigmoid function $S_j(x_j) = (1 + \gamma_j \exp(-x_j))^{-1}$ with respect to the PSP x_j are given here:

$$\frac{\partial}{\partial x_j} S_j(x_j) = S_j(x_j) (1 - S_j(x_j)) \quad (\text{A.1})$$

$$\frac{\partial^2}{\partial x_j^2} S_j(x_j) = S_j(x_j) (1 - S_j(x_j)) (1 - 2S_j(x_j)) \quad (\text{A.2})$$

$$\begin{aligned} \frac{\partial^3}{\partial x_j^3} S_j(x_j) &= S_j(x_j) \left(1 - S_j(x_j)\right) \\ &\times \left(1 - 6S_j(x_j) \left(1 - S_j(x_j)\right)\right). \end{aligned} \quad (\text{A.3})$$

Please note that the derivatives are also valid for a case in which the sigmoid function is shifted, for instance, by $-1/(1 - \gamma_j)$ as used in several studies to obtain $S_j(0) = 0$ (as discussed in Section 3.2). The x_j value of the inflection point (x_I, z_I) is found by setting the second derivative (A.2) to zero and solving this equation for x_j . In doing so a single solution $x_I(\gamma_j) = \log(\gamma_j)$ is found that is an inflection point because the third derivative satisfies a non-zero number with respect to x_I (i.e., $-1/8$). This means that only one inflection point exists where the slope is at the maximum. The corresponding z_j -value of the inflection point can be found by plugging x_I in the sigmoid function $S_j(x_j = x_I)$, which gives $z_I = 1/2$. The first derivative (A.1) describes the slope of the function. By plugging x_I in the first derivative one obtains the maximum slope $\bar{s}_{\max} = 1/4$, that is at the inflection point (x_I, z_I), normalized with respect to the characteristic mean firing rate m_c and mean membrane potential u_c . Since the normalized slope of the sigmoid function do not depend on the sigmoid parameter γ_j the shape of the sigmoid function is constant. However, for physical values, a change of the ratio between the characteristic mean firing rate and the mean membrane potential m_c/u_c scales the corresponding axes and can be interpreted as a slope change of the transfer function (3.16)

$$\frac{\partial}{\partial x_j} S_j(x_j) = \frac{m_c}{u_c} \frac{\partial}{\partial u_j} S_j(u_j/u_c). \quad (\text{A.4})$$

The physical value of the maximum slope (i.e., at the inflection point), for example, is $700 \text{ s}^{-1} \text{ V}^{-1}$ by applying the characteristic constants proposed by Jansen and Rit [54] presented in Table 3.3.

Because the sigmoid function (3.16) increases and decreases asymptotically with increasing and decreasing PSP towards a mean firing rate

of zero and unity, an effective range $x_{j, \text{eff}}$ can be determined for the incoming PSPs. Because the sigmoid function is rotationally symmetrical at its inflection the effective range is symmetrical at this point. In order to specify the range the slope of the function (A.1) is used that drops to μ -times the maximum slope $\mu \bar{s}_{\text{max}}$, with $\mu : 0 < \mu \leq 1$ and the maximum slope $\bar{s}_{\text{max}} = 1/4$. Typically values for μ are 5×10^{-2} and 1×10^{-2} corresponding to 5% and 1% of the maximum slope \bar{s}_{max} . Now, by setting the first derivative of the sigmoid function (A.1) to $\mu \bar{s}_{\text{max}}$. Solving the equation $\mu(1 + \gamma_j \exp(-x_j))^2 = 4\gamma_j \exp(-x_j)$ with respect to $x_j = x_{j, \text{eff}}(\mu)$ yields

$$x_{j, \text{eff}}(\mu, \gamma_j) = \log(\gamma_j) \pm 2 \tanh^{-1}(\sqrt{1 - \mu}) \quad (\text{A.5})$$

where the first term is the PSP of the inflection point $x_1 = \log(\gamma_j)$ and the second term is the half-width of the effective spectrum $x_{j, s/2}(\mu) = 2 \tanh^{-1}(\sqrt{1 - \mu})$ so that $x_{j, \text{eff}}(\mu, \gamma_j) = x_1 \pm x_{j, s/2}(\mu)$. Thus, the full-width effective spectrum of the sigmoid (3.16) is $x_{j, s}(\mu) = 2 x_{j, s/2}(\mu)$.

A.2 Temporal Differential Operator

This part of the appendix describes the derivation of the differential operator using the rate-to-potential conversion. The literature also has examples of the use of a biexponential function to fit the dendritic impulse-response function from experimental data (e. g., [49,219]). This function can be approximated by the alpha function (3.18) for the case that the area under both kernels is normalized to unity

$$\bar{h}_j = \begin{cases} \frac{\xi_j \beta_j}{\xi_j - 1} (\exp(-\beta_j \kappa) - \exp(-\xi_j \beta_j \kappa)) & \text{if } \kappa \geq 0, \xi_j \neq 1 \\ \beta_j^2 \kappa \exp(-\beta_j \kappa) & \text{if } \kappa \geq 0, \xi_j = 1 \\ 0 & \text{if } \kappa = 0 \end{cases} \quad (\text{A.6})$$

with the normalized time $\kappa = t/\tau$ (where τ is some characteristic time scale), the ratio $\beta_j = \tau/\tau_j$ of a characteristic time τ to the dendritic time constant τ_j of a neural ensemble j , and the ratio ξ_j of characteristic decay to rise time. Letting $\xi_j \rightarrow 1$ in the biexponential function which is the first case in (A.6) yields the well-studied alpha function (3.18) which is the second case in (A.6)

$$\lim_{\xi_j \rightarrow 1} \frac{\xi_j \beta_j}{\xi_j - 1} (\exp(-\beta_j \kappa) - \exp(-\xi_j \beta_j \kappa)) = \beta_j^2 \kappa \exp(-\beta_j \kappa). \quad (\text{A.7})$$

The fact that the first and second cases are identical under these conditions can also be proved by using Lambert's \mathscr{W} function (also referred to as Omega function or product logarithm) and inverting the exponential form $f(\lambda) = x \exp(\lambda)$ by $\mu = \mathscr{W}(\mu) \exp(\mathscr{W}(\mu))$, where z is a complex number $z \in \mathbb{C}$ (see appendix A of [126] for a similar problem). Neglecting the spatial distribution with $r_1 = r_2$ in Eqs. (3.1) and (3.3) and insert (3.3) in (3.1), one obtains the rate-to-potential conversion of the form

$$x_j(\kappa) = o_j \frac{m_c}{u_c} \int_{\kappa}^{\infty} ds \bar{h}_j(\kappa - s) z_j(s). \quad (\text{A.8})$$

Which describes a temporal convolution (i.e., with respect to the normalized time κ) of the normalized dendritic kernel $\bar{h}_j(\kappa)$ and the incoming normalized mean firing rate $z_j(\kappa)$ with $x_j(\kappa) = u_j(\tau\kappa)/u_c$, $z_j(\kappa) = m_j(\tau\kappa)/m_c$ and $\alpha_j = o_j m_c/u_c$. The same applies to the potential-to-rate conversion with regard to Eqs. (3.2) and (3.4). The kernels (A.6) and (3.18) can be recast as Green's function and from the convolution (A.8) comes a second-order ordinary differential equation if, for instance, one carries out Laplace transform \mathscr{L} into the 's' domain with respect to κ

$$X_j(s) = o_j \frac{m_c}{u_c} \bar{H}_j(s) Z_j(s), \quad (\text{A.9})$$

where $X_j(s) = \mathcal{L}\{x_j\}_\kappa$, $\bar{H}_j(s) = \mathcal{L}\{\bar{h}_j\}_\kappa$ and $Z_j(s) = \mathcal{L}\{z_j\}_\kappa$. From the recast kernel, the area under the functions is normalized to unity (A.6) and the following transform arises

$$\bar{H}_j^{(n)}(s) = \begin{cases} \frac{\beta_j (\xi_j - 1)}{(s + \beta_j)(s + \xi_j \beta_j)} & \text{if } \xi_j \neq 1 \\ \frac{\beta_j^2}{(s + \beta_j)^2} & \text{if } \xi_j = 1. \end{cases} \quad (\text{A.10})$$

The second-order ordinary differential equation is obtained by inserting the kernels (A.10) into the Laplace transformed conversion (A.9), multiplying the denominators with the result that

$$(s + \beta_j)(s + \xi_j \beta_j) X_j(s) = \alpha_j Z_j(s), \quad (\text{A.11})$$

and transforming (A.11) back \mathcal{L}^{-1} to the ' κ ' domain

$$\left(\frac{d^2}{d\kappa^2} + (1 + \xi_j) \beta_j \frac{d}{d\kappa} + \xi_j \beta_j^2 \right) x_j(\kappa) = \alpha_j \psi_j z_j(\kappa), \quad (\text{A.12})$$

with the factor $\alpha_j = o_j m_c / u_c$ and

$$\psi_j = \begin{cases} \beta_j (\xi_j - 1) & \text{if } \xi_j \neq 1 \\ \beta_j^{-2} & \text{if } \xi_j = 1. \end{cases} \quad (\text{A.13})$$

The left side of (A.13), and thus the corresponding second-order differential operator $\bar{L}(\lambda) = \lambda^2 + (1 + \xi_j) \beta_j \lambda + \xi_j \beta_j^2$ with time scale β_j is the same for all kernels (i.e., depending on ξ_j), namely the normalized biexponential and alpha function $\bar{h}_j^{(n)}(\kappa)$ (A.6). What differs is the coupling factor ξ_j on the right side of the Eq. (A.12) incorporating the normalization (A.13).

A.3 Effective Extrinsic Input on all Masses

In order to constrain the extrinsic inputs, the saturation effects of the sigmoidal transfer function can be evaluated. On the basis of the effective range for transferring PSPs to mean firing rates as defined in Appendix A.1, an optimal operating point on the sigmoid curve (Eq. (3.16)) can be specified. For this purpose, the incoming PSP x_b is differentiated in an offset $x_{b,D}$ with $\partial x_{b,D}/\partial \kappa = 0$ and a time-variant component $x_{b,A}(\kappa)$ so that $x_b(\kappa) = x_{b,D} + x_{b,A}(\kappa)$. Then, of the basis of the effective range that is symmetrical on the sigmoid function at its inflection point $(x_I, z_I) = (\log(\gamma_b), 1/2)$ (see Section 3.2.1 and Appendix A.1) the optimal operating point of a NM can be specified by the incoming PSP $\hat{x}_{b,D} \equiv z_I$ and $x_{b,A}(\kappa) \equiv [-x_{b,S/2}, x_{b,S/2}]$, where $x_{b,S/2}$ denotes the half-width of the effective spectrum of a NM of type b (see Eq. (A.5) in Appendix A.1). The PSP $x_b(\kappa)$ can be caused extrinsically (i. e., x_{bT}) and intrinsically (i. e., x_{ba}). In line with the decomposition of $x_b(\kappa)$, the extrinsic and intrinsic input can be defined as $x_{bT} = x_{bT,D} + x_{bT,A}(\kappa)$ and $x_{ba} = x_{ba,D} + x_{ba,A}(\kappa)$, so that $x_b = (x_{bT,D} + x_{ba,D}) + (x_{bT,A} + x_{ba,A})(\kappa)$. While the latter $x_{bT}(\kappa)$ is, in principle, unrestricted in range, the former $x_{ba}(\kappa)$ is restricted by the saturation effects of the sigmoidal potential-to-rate transfer function $S_b(x_b)$. The intrinsic mean firing rates are normalized between zero and one $z_{ba} = [0, 1]$ (see Appendix A.1), scaled by α_{ba} and low-pass filtered through the dendrites (see Eq. (A.8) in Appendix A.2). Since the area under the dendritic kernel $h_{ba}(\kappa)$ is normalized to unity (see Section 3.2.2 and Eq. (A.6) in Appendix A.2) the intrinsic mean firing rates cause PSPs $x_{ba} = [x_{ba,\min}, x_{ba,\max}]$ ranging between zero and α_{ba} (excitatory: $[0, \alpha_{ba}]$ or inhibitory: $[\alpha_{ba}, 0]$). For the definition of the effective range of an extrinsic input with respect to the maintenance the optimal operating point, two limiting cases have to be considered: (i) information exclusively transferred through intrinsic input and (ii) information exclusively transferred through extrinsic input.

In the first case, the extrinsic input is simply an offset component

$\hat{x}_{bT} = \hat{x}_{bT,D}$ and the intrinsic input range \hat{x}_{ba} is

$$\hat{x}_{ba}(\kappa) = [x_{b,S}, x_{ba,\max}], \quad (\text{A.14})$$

where the minimum input value $x_{b,S} = 2x_{b,S/2}$ ensures information transfer over the full-width of the effective spectrum of the sigmoid function $x_{b,S}$ (see Appendix A.1). Thus, the offset $\hat{x}_{ba,D}$ and the time-variant component $\hat{x}_{ba,A}(\kappa)$ of the intrinsic input is given by $\hat{x}_{ba,D} = \hat{x}_{ba}(\kappa) - x_{b,S/2}$ and $\hat{x}_{ba,A}(\kappa) = [-x_{b,S/2}, x_{b,S/2}]$. Since the optimal operating point is at the inflection of the sigmoid z_I the extrinsic input is $\hat{x}_{bT} = z_I - \hat{x}_{ba,D}$, so that $\hat{x}_{bT} = z_I + x_{b,S/2} - \hat{x}_{ba}(\kappa)$. By considering the range of the intrinsic input $\hat{x}_{ba}(\kappa)$ (A.14) the effective extrinsic input range is obtained where only the intrinsic information is transferred

$$\hat{x}_{bT} = [z_I + x_{b,S/2} - x_{ba,\max}, z_I - x_{b,S/2}]. \quad (\text{A.15})$$

In the second case, the intrinsic input $\hat{x}_{ba} = \hat{x}_{ba,D}$ is just a offset component with the range $x_{ba}(\kappa) = [x_{ba,\min}, x_{ba,\max}]$. In this case, only information through extrinsic input is transferred, where the offset and the time-varying component of the extrinsic input \hat{x}_{bT} is specified by $\hat{x}_{bT,D} = x_I - \hat{x}_{ba}$ and $\hat{x}_{bT,A}(\kappa) = [-x_{b,S/2}, x_{b,S/2}]$. The range of the intrinsic input $x_{ba}(\kappa)$ is considered in order to obtain the effective extrinsic input range

$$\hat{x}_{bT} = [z_I - x_{b,S/2} - x_{ba,\max}, z_I + x_{b,S/2} - x_{ba,\min}]. \quad (\text{A.16})$$

The maximum range is given by the second case, where the information is exclusively transferred from extrinsic input. Finally, the extrinsic PSP $x_{bT}(\kappa)$ has an effective range between $z_I - x_{b,S/2} - x_{ba,\max}$ and $z_I + x_{b,S/2} - x_{ba,\min}$ with $x_{ba}(\kappa) = [x_{ba,\min}, x_{ba,\max}]$ depending on the type of input, that is, excitatory: $x_{ba}(\kappa) = [0, \alpha_{ba}]$ or inhibitory: $x_{ba}(\kappa) = [\alpha_{ba}, 0]$.

A.4 Modes of a Single Neural Mass

The stability analysis is demonstrated exemplarily for a single NM as described with the two linear differential equations in Section 3.2.3 (Eqs. (3.20) and (3.21)), (disregarding the indices),

$$\dot{x}(\kappa) = y(\kappa) \tag{A.17}$$

$$\dot{y}(\kappa) = \alpha\beta^2 S(x_T(\kappa)) - 2\beta y(\kappa) - \beta^2 x, \tag{A.18}$$

where only extrinsic inputs have the NM as their target. Stabilities of the system involve studying it at its equilibria, by which is meant states where the variables do not change. For this purpose all derivatives in Eqs. (A.17) and (A.18) are constrained to be zero, which, by inserting Eq. (A.17) in Eq. (A.18), leads to a function of the equilibria

$$x_0 = \alpha S(x_T). \tag{A.19}$$

The fixed-point function is a continuously differentiable one-dimensional manifold in the two-dimensional system and has the same shape as the transfer function S , simply scaled with α . In the next step, one has to identify the stability of the fixed points x_0 , which can be done by studying the linearized system (Eqs. (A.17) and (A.18)) at the fixed points. For this purpose, the Jacobian matrix \mathcal{J} is set up containing all partial derivatives of the temporal kinetics \dot{x} and \dot{y} with respect to the variables x and y

$$\mathcal{J} = \begin{pmatrix} 0 & 1 \\ -\beta^2 & -2\beta \end{pmatrix} \tag{A.20}$$

which is, effectively, the structure

$$\mathcal{J} = \begin{pmatrix} \partial\dot{x}/\partial x & \partial\dot{x}/\partial y \\ \partial\dot{y}/\partial x & \partial\dot{y}/\partial y \end{pmatrix}. \tag{A.21}$$

For the stability of the system to be characterized, the Jacobian matrix is evaluated at the fixed points by calculating the two eigenvalues λ . In this case, however, the Jacobian matrix depends only on the intrinsic temporal ratio and not on the extrinsic input x_T . Consequently, the Jacobian matrix characterizes all fixed points without special evaluation (i. e., inserting the fixed-point curve (A.19)). This also means that no bifurcations occur in the system with respect to the extrinsic input x_T . The calculation of the eigenvalues (i. e., the determinant $0 = \det(\mathcal{J} - \lambda \mathbf{I}_2)$, where \mathbf{I}_2 is a two-dimensional identity matrix) of the Jacobian matrix (A.20) yields

$$\lambda_{1,2} = -\beta. \quad (\text{A.22})$$

Generally, if an eigenvalue is negative $\lambda < 0$, if it is positive $\lambda > 0$ or if it is zero $\lambda = 0$, the system is stable, unstable or critical respectively. If there is a critical eigenvalue, $\lambda = 0$, the bifurcations of the system must be studied. However, since the intrinsic temporal ratio β is always positive $\beta : \beta \in \mathbb{R}^+$ both eigenvalues $\lambda_{1,2}$ are always negative and thus the system (Eqs. (A.17) and (A.18)) is stable.

Another exemplary case would be the system (Eqs. (A.17) and (A.18)) if the NM fed the PSP $x(\kappa)$ back (auto-feedback)

$$\dot{x}(\kappa) = y(\kappa) \quad (\text{A.23})$$

$$\dot{y}(\kappa) = \beta^2 S(\alpha x(\kappa) + x_T(\kappa)) - 2\beta y(\kappa) - \beta^2 x(\kappa). \quad (\text{A.24})$$

For this auto-feedback system the function of the fixed points $x_{T,0}$ is more complicated

$$x_{T,0} = \log\left(\frac{\gamma x_0}{1 - x_0}\right) - \alpha x_0, \quad (\text{A.25})$$

where γ denotes the sigmoid parameter. Eq. (A.25) will clearly not solve for the variable x_0 . Furthermore, the Jacobian matrix \mathcal{J} of this

auto-feedback system is given as follows

$$\mathcal{J} = \begin{pmatrix} 0 & 1 \\ \beta^2(S'(\alpha x + x_T) - 1) & -2\beta \end{pmatrix}, \quad (\text{A.26})$$

where $S'(x)$ denotes the partial derivative with respect to the PSP x with $S'(x) = \partial S(x)/\partial x$. The Jacobian matrix (A.26) of the auto-feedback system is a function of the intrinsic time ration β , the coupling factor α for the auto-feedback, the sigmoid parameter γ , the PSP x and the extrinsic input x_T . To investigate stabilities of the auto-feedback system one evaluates the Jacobian matrix \mathcal{J}_0 at the fixed point function $x_{T,0}$ (A.25)

$$\mathcal{J}_0 = \begin{pmatrix} 0 & 1 \\ \beta^2(\alpha(1 - x_0)x_0 - 1) & -2\beta \end{pmatrix}, \quad (\text{A.27})$$

and computes its eigenvalues λ

$$\frac{\lambda_{1,2}}{\beta} = -1 \pm \sqrt{\alpha(1 - x_0)x_0}. \quad (\text{A.28})$$

Since the intrinsic temporal ratio β is always positive $\beta : \beta \in \mathbb{R}^+$, the eigenvalues of the linearized system at the fixed points $\lambda_{1,2}$ are simply scaled with β . The auto-feedback system is critical $x_{\text{crit.}}$ in a state if at least one eigenvalue is zero. This means that the real part of the second term in Eq. (A.28) is either plus or minus unity $x_{\text{crit.}} : \text{Re}(\sqrt{\alpha(1 - x_{\text{crit.}})x_{\text{crit.}}}) = \pm 1$ with the critical states

$$x_{\text{crit.}} = \frac{1}{2} \pm \frac{\sqrt{\alpha - 4}\sqrt{\alpha}}{2\alpha}. \quad (\text{A.29})$$

The critical states $x_{\text{crit.}}$ can be translated into an extrinsic input by using Eq. (A.25) with $x_0 = x_{\text{crit.}}$. The corresponding eigenvalues $\lambda_{1,2}/\beta = -1 \pm 1$ characterize the critical values as a saddle-node bifurcation. Within the stable regimes the system qualitatively changes from a node

(i.e., $\lambda_{1,2} \in \mathbb{R}^-$) to a focus (i.e., $\lambda_{1,2} = -1 \pm i\mu$) with $\mu \in \mathbb{R}$) when the second term in Eq. (A.28) changes from real to complex value or vice versa for $\alpha = 0$, $x_0 = 0$ and $x_0 = 1$. For the complete bifurcation diagram see Fig. A.1.

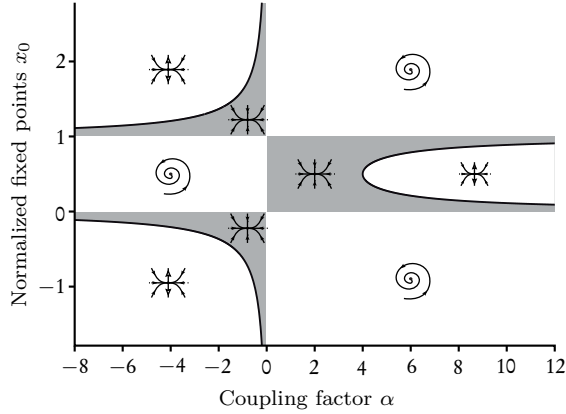


Fig. A.1. Bifurcation diagram of a single NM with auto-feedback. The diagram shows the equilibria of the normalized PSP x_0 against the coupling factor α of the auto-feedback. The three solid curves are the critical points x_{crit} . (see Eq. (A.29)). The phase portrait in each regime characterizes the state ϕ . The equilibria can be translated into an extrinsic input $x_{T,0}$ (see Eq. (A.25)).

A.5 Characteristic Mean Frequency

An estimation of the frequency of a LC that has its existence on a folded manifold with complex folding in the state space, for example by means of the Fourier transform of a state variable, could lead to imprecise or false values. For the sake of greater precision one can compute the so-called characteristic mean frequency [255] of an orbit by using the system state equations (e.g., Eqs. (5.3) to (5.5)). Generally, for any

n -dimensional curve ϕ the angular velocity v at each normalized time point κ is

$$v(\kappa) = \frac{d\phi}{d\kappa} \rho(\kappa), \quad (\text{A.30})$$

where $d\phi/d\kappa = \left\| \dot{\phi} \right\|$ is the speed along the curve and

$$\rho(\kappa) = \frac{\left\| \dot{\phi} \times \ddot{\phi} \right\|}{\left\| \dot{\phi} \right\|^3} \quad (\text{A.31})$$

is the radius of curvature. The characteristic mean frequency $\tilde{\eta}$ is defines as $\tilde{\eta} = \lim_{T \rightarrow \infty} \omega(T) - \omega(0)/T$ or as the time averaging of the angular velocity

$$\tilde{\eta} = \langle v \rangle, \quad (\text{A.32})$$

where $\langle \cdot \rangle$ denotes the averaging over the normalized time κ , T is the normalized observation time and ω the phase with

$$\omega = \int_T d\kappa v. \quad (\text{A.33})$$

For instance, for the six-dimensional system (see Eqs. (5.3) to (5.5) in Section 5.2.1) the angular velocity is defined by

$$v(\kappa) = \frac{1}{v_{03}^2 + v_{31}^2 + v_{32}^2} \left((\dot{v}_{31} v_{03} - \dot{v}_{03} v_{31})^2 + (\dot{v}_{03} v_{32} - \dot{v}_{32} v_{03})^2 + (\dot{v}_{32} v_{31} - \dot{v}_{31} v_{32})^2 \right)^{1/2}, \quad (\text{A.34})$$

with the derivative of states $\dot{\phi}(\kappa) = (y_{03} \ y_{31} \ y_{32} \ \dot{y}_{03} \ \dot{y}_{31} \ \dot{y}_{32})^T$. Finally, by applying Eq. (A.30) the characteristic mean frequency $\tilde{\eta}$ of the six-dimensional system is obtained.

A.6 Symbols and Abbreviations

In this work, in addition to standard abbreviations of English spelling, the International System of Units and the common mathematical symbols (ISO 31-11), special abbreviations and symbols are used. These specific abbreviations, mathematical variables, parameters, operators and subscripts are listed here.

Table A.1. Abbreviations

Abbreviation	Meaning
AH	Andronov-Hopf
AMPA	Type of Glutamate Receptors
EIN	Excitatory Interneuron
EEG	Electroencephalography
GABA	Gamma-Aminobutyric-Acid
IIN	Inhibitory Interneuron
LC	Limit Cycle
LFP	Local Field Potential
MEG	Magnetoencephalography
MRI	Magnetic Resonance Imaging
NM	Neural Mass
NMM	Neural Mass Model
PC	Pyramidal Cell
PSP	Postsynaptic Potential

Table A.2. Variables

Variable	Meaning	Unit
m	Mean Firing Rate	s^{-1}
p	Extrinsic Input	V
r	Location	m
t	Time	s
u	Mean Postsynaptic Potential	V
v	Propagation Velocity	$m s^{-1}$
x	Normalized Mean Postsynaptic Potential	1
y	Normalized Mean Current	1
z	Normalized Mean Firing Rate	1
ϵ	Noise Process	V, s^{-1}
κ	Normalized Time	1
ϕ	Neural State	V, s^{-1}
χ	Measurement (e. g., EEG and MEG)	V, T
ψ	Perturbation	V, s^{-1}
ω	Angle	rad

Table A.3. Parameters

Parameter	Meaning	Unit
o	Linear Scaling Factor	1
α	Coupling Factor	1
β	Intrinsic Temporal Ratio, $\beta = \tau/\tau_{ba}$	1
γ	Normalized Sigmoid Parameter	1
ζ	Normalized Stimulus Amplitude	1
η	Normalized Stimulus Frequency	1
θ	Parameter Vector	
τ	Characteristic Time Constant	s
J	Set of Neural Masses or Connections	1
Γ	Velocity Domain	$m s^{-1}$
Ω	Spatial Domain	m

Table A.4. Operators

Operator	Meaning
f	Dendritic Spatial Distribution
g	Axonal Spatial Distribution
h	Dendritic Impulse Response Function
k	Axonal Impulse Response Function
l	Velocity Distribution
C	Dendritic Differential Operator
D	Axonal Differential Operator
L	General Differential Operator
S	Potential-to-Rate Transfer Function
\mathcal{O}	Potential-to-Rate Operator
\mathcal{P}_ϕ	State System
\mathcal{P}_χ	Observer System
\mathcal{Q}	Rate-to-Potential Operator
δ	Dirac Delta Function
Δ	Distance

Table A.5. Subscripts

Subscript	Meaning
a	Starting Neural Mass $a : a \in J$
b	Targeting Neural Mass $b : b \in J$
c	Characteristic Constant
e	Excitatory Projection
i	Inhibitory Projection
j	Type of Neural Mass $j : j \in J$ or of Connection $j : j = ba$
I	Point of Inflection
T	Extrinsic Input

Bibliography

1. S. Finger, *Origins of neuroscience: A history of explorations into brain functions*. Oxford Univ. Press, 2001.
2. G. M. Shepherd, *Foundations of the neuron doctrine*. History of neuroscience, Oxford Univ. Press, 1991.
3. S. L. Bressler and J. A. Kelso, "Cortical coordination dynamics and cognition," *Trends Cogn Sci*, vol. 5, pp. 26–36, Jan 2001.
4. G. Deco, V. K. Jirsa, P. A. Robinson, M. Breakspear, and K. Friston, "The dynamic brain: From spiking neurons to neural masses and cortical fields," *PLoS Comput Biol*, vol. 4, p. e1000092, Aug 2008.
5. A. R. McIntosh, "Towards a network theory of cognition," *Neural Networks*, vol. 13, pp. 861–70, Oct-Nov 2000.
6. V. K. Jirsa, "Connectivity and dynamics of neural information processing," *Neuroinformatics*, vol. 2, no. 2, pp. 183–204, 2004.
7. V. B. Mountcastle, *Perceptual neuroscience: The cerebral cortex*. Cambridge, London: Harvard Univ. Press, 1998.
8. A. R. Luria, *Higher cortical functions in mans*. New York: Basic Books, 2 ed., 1980.
9. E. Basar, A. Gonder, C. Ozesmi, and P. Ungan, "Dynamics of brain rhythmic and evoked potentials. iii. studies in the auditory pathway, reticular formation, and hippocampus during sleep," *Biol Cybern*, vol. 20, pp. 161–9, Nov 1975.
10. E. Basar, A. Gonder, C. Ozesmi, and P. Ungan, "Dynamics of brain rhythmic and evoked potentials. ii. studies in the auditory pathway, reticular formation, and hippocampus during the waking stage," *Biol Cybern*, vol. 20, pp. 145–60, Nov 1975.

11. M. M. Mesulam, "Large-scale neurocognitive networks and distributed processing for attention, language, and memory," *Ann Neurol*, vol. 28, pp. 597–613, Nov 1990.
12. M. N. Livanov, *Spatial organization of cerebral processes*. New York: Wiley, 1977.
13. P. L. Nunez, "Toward a quantitative description of large-scale neocortical dynamic function and eeg," *Behav Brain Sci*, vol. 23, pp. 371–98; 399–437, Jun 2000.
14. E. R. John, "A field theory of consciousness," *Conscious Cogn*, vol. 10, pp. 184–213, Jun 2001.
15. R. S. Menon and S. G. Kim, "Spatial and temporal limits in cognitive neuroimaging with fmri," *Trends Cogn Sci*, vol. 3, pp. 207–16, Jun 1999.
16. A. T. Lee, G. H. Glover, and C. H. Meyer, "Discrimination of large venous vessels in time-course spiral blood-oxygen-level-dependent magnetic-resonance functional neuroimaging," *Magn Reson Med*, vol. 33, pp. 745–54, Jun 1995.
17. H. L. Liu, J. C. Huang, J. J. Wang, Y. L. Wan, and Y. Y. Wai, "The effects of single-trial averaging on the temporal resolution of functional mri," *Magn Reson Imaging*, vol. 24, pp. 597–602, Jun 2006.
18. K. J. Friston, A. P. Holmes, J. B. Poline, P. J. Grasby, S. C. Williams, R. S. Frackowiak, and R. Turner, "Analysis of fmri time-series revisited," *Neuroimage*, vol. 2, pp. 45–53, Mar 1995.
19. S. G. Kim, W. Richter, and K. Ugurbil, "Limitations of temporal resolution in functional mri," *Magn Reson Med*, vol. 37, pp. 631–6, Apr 1997.
20. M. D. Robson, J. L. Dorosz, and J. C. Gore, "Measurements of the temporal fmri response of the human auditory cortex to trains of tones," *Neuroimage*, vol. 7, pp. 185–98, Apr 1998.
21. K. Müller, T. Mildner, G. Lohmann, and D. Y. von Cramon, "Investigating the stimulus-dependent temporal dynamics of the bold signal using spectral methods," *J Magn Reson Imaging*, vol. 17, pp. 375–82, Mar 2003.
22. J. Neumann, G. Lohmann, S. Zysset, and D. Y. von Cramon, "Within-subject variability of bold response dynamics," *Neuroimage*, vol. 19, pp. 784–96, Jul 2003.
23. P. L. Nunez, *Electric fields of the brain*. Oxford Univ. Press, Jul 1981.
24. M. Hämmäläinen, R. Hari, R. J. Ilmoniemi, J. Knuutila, and O. V. Lounasmaa, "Magnetoencephalography—theory, instrumentation, and applications to noninvasive studies of the working human brain," *RMP*, vol. 65, pp. 413–97, Apr 1993.

-
25. E. Niedermayer and F. Lopes da Silva, *Electroencephalography*. Lippincott Williams & Wilkins, 2005.
 26. W. Andrä and H. Nowak, *Magnetism in medicine: A handbook*. Wiley-VCH, 2 ed., 2006.
 27. F. Lopes da Silva and A. van Rotterdam, “Biophysical aspects of eeg and magnetoencephalogram generation,” in *Electroencephalography: Basic principles, clinical applications and related fields* (E. Niedermayer and F. Lopes da Silva, eds.), pp. 93–109, Baltimore: Williams & Wilkins, 4 ed., 1999.
 28. D. Sparks, L.-F. Lue, T. A. Martin, and J. Rogers, “Neural tract tracing using di-i: A review and a new method to make fast di-i faster in human brain,” *J Neurosci Methods*, vol. 103, no. 1, pp. 3–10, 2000.
 29. F. Babiloni, C. Babiloni, F. Carducci, G. L. Romani, P. M. Rossini, L. M. Angelone, and F. Cincotti, “Multimodal integration of high-resolution eeg and functional magnetic resonance imaging data: A simulation study,” *Neuroimage*, vol. 19, pp. 1–15, May 2003.
 30. Y. Iturria-Medina, R. C. Sotero, E. J. Canales-Rodríguez, Y. Alemán-Gómez, and L. Melie-García, “Studying the human brain anatomical network via diffusion-weighted mri and graph theory,” *Neuroimage*, vol. 40, no. 3, pp. 1064–76, 2008.
 31. G. Gong, Y. He, L. Concha, C. Lebel, D. W. Gross, A. C. Evans, and C. Beaulieu, “Mapping anatomical connectivity patterns of human cerebral cortex using in vivo diffusion tensor imaging tractography,” *Cereb Cortex*, vol. 19, no. 3, pp. 524–36, 2009.
 32. M. Axer, K. Amunts, D. Grässel, C. Palm, J. Dammers, H. Axer, U. Pietrzyk, and K. Zilles, “A novel approach to the human connectome: Ultra-high resolution mapping of fiber tracts in the brain,” *Neuroimage*, vol. 54, no. 2, pp. 1091–101, 2011.
 33. F. H. Lopes da Silva, “Functional localization of brain sources using eeg and/or meg data: Volume conductor and source models,” *Magn Reson Imaging*, vol. 22, pp. 1533–8, 2004.
 34. N. J. Trujillo-Barreto, E. Aubert-Vázquez, and W. D. Penny, “Bayesian m/eeg source reconstruction with spatio-temporal priors,” *Neuroimage*, vol. 39, no. 1, pp. 318–35, 2008.
 35. P. A. Valdés-Sosa, M. Vega-Hernández, J. M. Sánchez-Bornot, E. Martínez-Montes, and M. A. Bobes, “Eeg source imaging with spatio-temporal tomographic nonnegative independent component analysis,” *Hum Brain Mapp*, vol. 30, no. 6, pp. 1898–910, 2009.

36. A. Schlögl and G. Supp, "Analyzing event-related eeg data with multivariate autoregressive parameters," in *Event-related dynamics of brain oscillations* (C. Neuper and W. Klimesch, eds.), vol. 159 of *Prog Brain Res*, pp. 137–52, Elsevier, 2006.
37. J. J. Wright, R. R. Kydd, and A. A. Sergejew, "Autoregression models of eeg. results compared with expectations for a multilinear near-equilibrium biophysical process," *Biol Cybern*, vol. 62, no. 3, pp. 201–10, 1990.
38. T. Milde, L. Leistritz, L. Astolfi, W. H. Miltner, T. Weiss, F. Babiloni, and H. Witte, "A new kalman filter approach for the estimation of high-dimensional time-variant multivariate ar models and its application in analysis of laser-evoked brain potentials," *Neuroimage*, vol. 50, pp. 960–9, Apr 2010.
39. C. Lamus, C. J. Long, M. S. Hamalainen, E. N. Brown, and P. L. Purdon, "Parameter estimation and dynamic source localization for the magnetoencephalography (meg) inverse problems," *Proceedings ISBI*, vol. 2007, pp. 1092–5, May 2007.
40. L. Astolfi, F. Cincotti, D. Mattia, M. Lai, F. de Vico Fallani, L. Baccala, M. Ursino, M. Zavaglia, and F. Babiloni, "Causality estimates among brain cortical areas by partial directed coherence: simulations and application to real data," *IJBEM*, vol. 7, no. 1, pp. 62–5, 2005.
41. F. Babiloni, F. Cincotti, C. Babiloni, F. Carducci, D. Mattia, L. Astolfi, A. Basilisco, P. M. Rossini, L. Ding, Y. Ni, J. Cheng, K. Christine, J. Sweeney, and B. He, "Estimation of the cortical functional connectivity with the multimodal integration of high-resolution eeg and fmri data by directed transfer function," *Neuroimage*, vol. 24, pp. 118–31, Jan 2005.
42. C. Granger, "Investigating causal relations by econometric methods and cross-spectral methods," *Econometrica*, vol. 37, no. 3, pp. 424–38, 1969.
43. L. A. Baccala and K. Sameshima, "Partial directed coherence: A new concept in neural structure determination," *Biol Cybern*, vol. 84, pp. 463–74, Jun 2001.
44. L. A. Baccala and K. Sameshima, "Comments on 'is partial coherence a viable technique for identifying generators of neural oscillators?'," *Biol Cybern*, vol. 95, pp. 135–141, Aug 2006.
45. K. J. Blinowska, R. Kus, and M. Kaminski, "Granger causality and information flow in multivariate processes," *Phys Rev E Stat Nonlin Soft Matter Phys*, vol. 70, p. 050902, Nov 2004.
46. M. Kaminski, M. Ding, W. A. Truccolo, and S. L. Bressler, "Evaluating causal relations in neural systems: Granger causality, directed transfer func-

- tion and statistical assessment of significance,” *Biol Cybern*, vol. 85, pp. 145–157, Aug 2001.
47. L. Sommerlade, M. Eichler, M. Jachan, K. Henschel, J. Timmer, and B. Schelter, “Estimating causal dependencies in networks of nonlinear stochastic dynamical systems,” *Phys Rev E Stat Nonlin Soft Matter Phys*, vol. 80, p. 051128, Nov 2009.
 48. O. David and K. J. Friston, “A neural mass model for meg/eeg: Coupling and neuronal dynamics,” *Neuroimage*, vol. 20, pp. 1743–55, Nov 2003.
 49. W. J. Freeman, *Mass action in the nervous system: Examination of the neurophysiological basis of adaptive behavior through the EEGs*. New York: Academic Press, 1975.
 50. S. J. Kiebel, M. I. Garrido, R. Moran, C. C. Chen, and K. J. Friston, “Dynamic causal modeling for eeg and meg,” *Hum Brain Mapp*, vol. 30, no. 6, pp. 1866–76, 2009.
 51. A. Spiegler, S. J. Kiebel, F. M. Atay, and T. R. Knösche, “Bifurcation analysis of neural mass models: Impact of extrinsic inputs and dendritic time constants,” *Neuroimage*, vol. 52, no. 3, pp. 1041–58, 2010.
 52. W. Freeman, “Models of the dynamics of neural populations,” *Electroencephalogr Clin Neurophysiol*, vol. 34, pp. 9–18, 1978.
 53. B. H. Jansen, G. Zouridakis, and M. E. Brandt, “A neurophysiologically-based mathematical model of flash visual evoked potentials,” *Biol Cybern*, vol. 68, no. 3, pp. 275–83, 1993.
 54. B. H. Jansen and V. G. Rit, “Electroencephalogram and visual evoked potential generation in a mathematical model of coupled columns,” *Biol Cybern*, vol. 73, pp. 357–66, Sep 1995.
 55. F. H. Lopes da Silva, A. Hoeks, H. Smits, and L. H. Zetterberg, “Model of brain rhythmic activity. the alpha-rhythm of the thalamus,” *Kybernetik*, vol. 15, pp. 27–37, May 1974.
 56. F. H. Lopes da Silva, A. van Rotterdam, P. Barts, E. van Heusden, and W. Burr, “Models of neuronal populations: the basic mechanisms of rhythmicity,” *Prog Brain Res*, vol. 45, pp. 281–308, 1976.
 57. P. Nunez, “The brain wave equation: A model for the eegs,” *Math Biosci*, vol. 21, pp. 279–97, 1974.
 58. L. H. Zetterberg, L. Kristiansson, and K. Mossberg, “Performance of a model for a local neuron population,” *Biol Cybern*, vol. 31, pp. 15–26, Nov 1978.

59. L. F. Abbott, "Lapicque's introduction of the integrate-and-fire model neuron (1907)," *Brain Res Bull*, vol. 50, pp. 303–4, Nov-Dec 1999.
60. A. L. Hodgkin and A. F. Huxley, "A quantitative description of membrane current and its application to conduction and excitation in nerve," *J Physiol (Lond)*, vol. 117, pp. 500–44, 1952.
61. R. FitzHugh, "Mathematical models of threshold phenomena in the nerve membrane," *Bull Math Biophys*, vol. 17, pp. 257–78, 1955.
62. J. Nagumo, S. Arimoto, and S. Yoshizawa, "An active pulse transmission line simulating nerve axon," *Proceedings IRE*, vol. 50, pp. 2061–70, 1962.
63. J. L. Hindmarsh and R. M. Rose, "A model of neuronal bursting using three coupled first order differential equations," *Phil Trans R Soc B*, vol. 221, pp. 87–102, 1984.
64. F. Wendling, J. J. Bellanger, F. Bartolomei, and P. Chauvel, "Relevance of nonlinear lumped-parameter models in the analysis of depth-eeg epileptic signals," *Biol Cybern*, vol. 83, pp. 367–78, Oct 2000.
65. F. Wendling, F. Bartolomei, J. J. Bellanger, and P. Chauvel, "Epileptic fast activity can be explained by a model of impaired gabaergic dendritic inhibition," *Eur J Neurosci*, vol. 15, pp. 1499–1508, May 2002.
66. O. David, L. Harrison, and K. J. Friston, "Modelling event-related responses in the brain," *Neuroimage*, vol. 25, no. 3, pp. 756–70, 2005.
67. O. David, K. J. M., and K. J. Friston, "Mechanisms of evoked and induced responses in meg/eeg," *Neuroimage*, vol. 31, pp. 1480–91, Jul 2006.
68. O. David, S. J. Kiebel, L. M. Harrison, J. Mattout, J. M. Kilner, and K. J. Friston, "Dynamic causal modeling of evoked responses in eeg and meg," *Neuroimage*, vol. 30, pp. 1255–72, May 2006.
69. R. C. Sotero, N. J. Trujillo-Barreto, Y. Iturria-Medina, F. Carbonell, and J. C. Jimenez, "Realistically coupled neural mass models can generate eeg rhythms," *Neural Comput*, vol. 19, no. 2, pp. 478–512, 2007.
70. S. J. Kiebel, O. David, and K. J. Friston, "Dynamic causal modelling of evoked responses in eeg/meg with lead field parameterization," *Neuroimage*, vol. 30, no. 4, pp. 1273–84, 2006.
71. S. J. Kiebel, M. I. Garrido, and K. J. Friston, "Dynamic causal modelling of evoked responses: The role of intrinsic connections," *Neuroimage*, vol. 36, no. 2, pp. 332–45, 2007.
72. R. J. Moran, K. E. Stephan, T. Seidenbecher, H. C. Pape, R. J. Dolan, and K. J. Friston, "Dynamic causal models of steady-state responses," *Neuroimage*, vol. 44, no. 3, pp. 796–811, 2009.

-
73. M. I. Garrido, J. M. Kilner, S. J. Kiebel, and K. J. Friston, "Evoked brain responses are generated by feedback loops," *Proc Natl Acad Sci USA*, vol. 104, pp. 20961–6, Dec 2007.
 74. M. I. Garrido, J. M. Kilner, S. J. Kiebel, and K. J. Friston, "Dynamic causal modeling of the response to frequency deviants," *J Neurophysiol*, vol. 101, pp. 2620–31, May 2009.
 75. T. M. Schofield, P. Iverson, S. J. Kiebel, K. E. Stephan, J. M. Kilner, K. J. Friston, J. T. Crinion, C. J. Price, and A. P. Leff, "Changing meaning causes coupling changes within higher levels of the cortical hierarchy," *Proc Natl Acad Sci USA*, vol. 106, pp. 11765–70, Jul 2009.
 76. F. Marten, S. Rodrigues, O. Benjamin, M. P. Richardson, and J. R. Terry, "Onset of polyspike complexes in a mean-field model of human electroencephalography and its application to absence epilepsy," *Phil Trans R Soc A*, vol. 367, pp. 1145–61, Mar 2009.
 77. S. Rodrigues, D. Barton, R. Szalai, O. Benjamin, M. P. Richardson, and J. R. Terry, "Transitions to spike-wave oscillations and epileptic dynamics in a human cortico-thalamic mean-field model," *J Comput Neurosci*, vol. 27, pp. 507–26, Dec 2009.
 78. P. Suffczynski, F. Lopes da Silva, J. Parra, D. Velis, and S. Kalitzin, "Epileptic transitions: Model predictions and experimental validation," *J Clin Neurophysiol*, vol. 22, pp. 288–99, Oct 2005.
 79. D. A. Steyn-Ross, M. L. Steyn-Ross, J. W. Sleigh, M. T. Wilson, I. P. Gillies, and J. J. Wright, "The sleep cycle modelled as a cortical phase transition," *J Biol Phys*, vol. 31, pp. 547–69, Dec 2005.
 80. L. P. Shil'nikov, "On a new type of bifurcation of multidimensional dynamic systems," *Dokl Akad Nauk SSSR*, vol. 189, no. 1, pp. 1368–71, 1969.
 81. G. Buzsáki, *Rhythms of the brain*. Oxford Univ. Press, 2006.
 82. K. Schwab, C. Ligges, T. Jungmann, B. Hilgenfeld, J. Haueisen, and H. Witte, "Alpha entrainment in human electroencephalogram and magnetoencephalogram recordings," *Neuroreport*, vol. 17, pp. 1829–33, Nov 2006.
 83. G. L. Gebber, S. Zhong, C. Lewis, and S. M. Barman, "Human brain alpha rhythm: Nonlinear oscillation or filtered noise?," *Brain Res*, vol. 818, no. 2, pp. 556–60, 1999.
 84. C. S. Herrmann, "Human eeg responses to 1-100 hz flicker: Resonance phenomena in visual cortex and their potential correlation to cognitive phenomena," *Exp Brain Res*, vol. 137, pp. 346–53, 2001.

85. R. B. Silberstein, "Steady-state visually evoked potentials, brain resonances, and cognitive processes," in *Neocortical dynamics and human EEG rhythms* (P. L. Nunez, ed.), pp. 272–303, Oxford Univ. Press, 1995.
86. Y. Jin, S. G. Potkin, C. A. Sandman, and W. E. Bunney, "Electroencephalographic photic driving in patients with schizophrenia and depression," *Biol Psychiatry*, vol. 41, pp. 496–9, Feb 1997.
87. V. Lazarev, D. Simpson, B. Schubsky, and L. deAzevedo, "Photic driving in the electroencephalogram of children and adolescents: harmonic structure and relation to the resting state," *Braz J Med Biol Res*, vol. 34, pp. 1573–84, Dec 2001.
88. T. Takahashi, H. Matsuoka, and T. Okuma, "High amplitude photic driving evoked by flickering-pattern in neuropsychiatric patients—with special reference to epileptics," *Psychiatry Clin Neurosci*, vol. 33, no. 3, pp. 305–6, 1979.
89. G. Stefanics, B. Hangya, I. Hernádi, I. Winkler, P. Lakatos, and I. Ulbert, "Phase entrainment of human delta oscillations can mediate the effects of expectation on reaction speeds," *J Neurosci*, vol. 30, no. 41, pp. 13578–85, 2010.
90. T. Trappenberg, *Fundamentals of computational neuroscience*. Oxford Univ. Press, 2 ed., Jan 2010.
91. P. S. Churchland, C. Koch, and T. J. Sejnowski, *What is computational neuroscience?*, pp. 46–55. Cambridge, MA, USA: MIT Press, 1993.
92. N. Wiener, *Cybernetics, second edition: Or the control and communication in the animal and the machine*. MIT Press, 1965.
93. F. Heylighen and C. Joslyn, "Cybernetics and second-order cybernetics," in *Encyclopedia of physical science & technology*, Academic Press, 2001.
94. S. J. Russell and P. Norvig, *Artificial intelligence: A modern approach*. Pearson Education, 2 ed., 2003.
95. S. Legg and M. Hutter, "Universal intelligence: A definition of machine intelligence," *Minds & Machines*, vol. 17, pp. 391–444, Dec 2007.
96. G. B. Ermentrout and D. H. Terman, *Mathematical foundations of neuroscience*. Springer, 1 ed., Jul 2010.
97. H. Haken, *Synergetics: An introduction: Nonequilibrium phase transitions and self-organization in physics, chemistry, and biology*. Springer, 1978.
98. P. H. Schimpf, C. Ramon, and J. Haueisen, "Dipole models for the eeg and meg," *IEEE T Bio-Med Eng*, vol. 49, pp. 409–18, May 2002.

-
99. J. Haueisen, C. Ramon, M. Eiselt, H. Brauer, and H. Nowak, "Influence of tissue resistivities on neuromagnetic fields and electric potentials studied with a finite element model of the head," *IEEE T Bio-Med Eng*, vol. 44, pp. 727–35, Aug 1997.
 100. J. Haueisen, D. S. Tuch, C. Ramon, P. H. Schimpf, V. J. Wedeen, J. S. George, and J. W. Belliveau, "The influence of brain tissue anisotropy on human eeg and meg," *Neuroimage*, vol. 15, pp. 159–66, Jan 2002.
 101. M. Hämäläinen, R. Hari, R. J. Ilmoniemi, J. Knuutila, and O. V. Lounasmaa, "Magnetoencephalography—theory, instrumentation, and applications to noninvasive studies of the working human brain," *RMP*, vol. 65, pp. 413–97, Apr 1993.
 102. H. Markram, M. Toledo-Rodriguez, Y. Wang, A. Gupta, G. Silberberg, and C. Wu, "Interneurons of the neocortical inhibitory system," *Nat Rev Neurosci*, vol. 5, pp. 793–807, Oct 2004.
 103. J. DeFelipe and I. Fariñas, "The pyramidal neuron of the cerebral cortex: Morphological and chemical characteristics of the synaptic inputs," *Prog Neurobiol*, vol. 39, no. 6, pp. 563–607, 1992.
 104. W. Freeman, "Tutorial in neurobiology: From single neurons to brain chaos," *IJBC*, vol. 2, pp. 451–82, 1992.
 105. F. Varela, J. P. Lachaux, E. Rodriguez, and J. Martinerie, "The brainweb: Phase synchronization and large-scale integration," *Nat Rev Neurosci*, vol. 2, pp. 229–39, Apr 2001.
 106. A. Hayer and U. S. Bhalla, "Molecular switches at the synapse emerge from receptor and kinase traffic," *PLoS Comput Biol*, vol. 1, p. e20, Jul 2005.
 107. W. Rall, "Theory of physiological properties of dendrites," *Ann N Y Acad Sci*, vol. 96, pp. 1071–92, Mar 1962.
 108. W. Rall, "Theoretical significance of dendritic trees for neuronal input-output relations," in *Neural Theory and Modeling* (R. Reiss, ed.), Stanford Univ. Press, 1964.
 109. W. Gerstner and W. M. Kistler, *Spiking neuron models: Single neurons, populations, plasticity*. Cambridge, New York: Cambridge Univ. Press, 2002.
 110. A. V. Herz, T. Gollisch, C. K. Machens, and D. Jaeger, "Modeling single-neuron dynamics and computations: A balance of detail and abstraction," *Science*, vol. 314, pp. 80–5, Oct 2006.
 111. J. Feng, "Is the integrate-and-fire model good enough?—a review," *Neural Networks*, vol. 14, no. 6-7, pp. 955–75, 2001.

112. E. M. Izhikevich, "Which model to use for cortical spiking neurons?," *IEEE T Neural Networ*, vol. 15, pp. 1063–70, Sep 2004.
113. C. Koch, *Biophysics of computation: Information processing in single neurons*. Computational Neuroscience Series, New York: Oxford Univ. Press, 2004.
114. W. J. Freeman and L. J. Rogers, "Fine temporal resolution of analytic phase reveals episodic synchronization by state transitions in gamma eegs," *J Neurophysiol*, vol. 87, pp. 937–45, Feb 2002.
115. A. A. Fingelkurts and A. A. Fingelkurts, "Making complexity simpler: Multivariability and metastability in the brain," *Int J Neurosci*, vol. 114, pp. 843–62, Jul 2004.
116. H. Markram, "The blue brain project," *Nat Rev Neurosci*, vol. 7, pp. 153–60, Feb 2006.
117. V. B. Mountcastle, "Modality and topographic properties of single neurons of cats somatic sensory cortex," *J Neurophysiol*, vol. 20, no. 4, pp. 408–34, 1957.
118. D. H. Hubel and T. N. Wiesel, "Receptive fields, binocular interaction and functional architecture in the cat's visual cortex," *J Physiol*, vol. 160, pp. 106–54, Jan 1962.
119. D. H. Hubel and T. N. Wiesel, "Receptive fields and functional architecture of monkey striate cortex," *J Physiol*, vol. 195, no. 1, pp. 215–43, 1968.
120. J. C. Horton and D. L. Adams, "The cortical column: A structure without a function," *Phil Trans R Soc B*, vol. 360, pp. 837–62, Apr 2005.
121. C. von der Malsburg, "The what and why of binding: The modeler's perspective," *Neuron*, vol. 24, pp. 95–104; 111–25, Sep 1999.
122. M. Arbib, P. Érdi, and J. Szentágothai, *Neural organization: Structure, function, and dynamics*. MIT Press, 1998.
123. W. J. Freeman, "Simulation of chaotic eeg patterns with a dynamic model of the olfactory system," *Biol Cybern*, vol. 56, no. 2-3, pp. 139–50, 1987.
124. A. Schüz and R. Miller, *Cortical areas: Unity and diversity*. Conceptual advances in brain research, London: Taylor & Francis, 2002.
125. A. A. Fingelkurts, A. A. Fingelkurts, and S. Kahkonen, "Functional connectivity in the brain—is it an elusive concept?," *Neurosci Biobehav Rev*, vol. 28, pp. 827–36, Jan 2005.
126. D. T. J. Liley, P. J. Cadusch, and M. P. Dafilis, "A spatially continuous mean field theory of electrocortical activity," *Network*, vol. 13, no. 1, pp. 67–113, 2002.

-
127. M. Oppen and D. Saad, *Advanced mean field methods: Theory and practice*. Neural information processing series, Cambridge, London: MIT Press, 2001.
 128. M. Breakspear and S. Knock, "Kinetic models of brain activity," *Brain Imag Behav*, vol. 2, pp. 270–88, Dec 2008.
 129. T. D. Frank, A. Daffertshofer, and P. J. Beek, "Multivariate ornstein-uhlenbeck processes with mean-field dependent coefficients: Application to postural sway," *Phys Rev E Stat Nonlin Soft Matter Phys*, vol. 63, p. 011905, Jan 2001.
 130. L. M. Harrison, O. David, and K. J. Friston, "Stochastic models of neuronal dynamics," *Phil Trans R Soc B*, vol. 360, pp. 1075–91, May 2005.
 131. E. Haskell, D. Q. Nykamp, and D. Tranchina, "Population density methods for large-scale modelling of neuronal networks with realistic synaptic kinetics: Cutting the dimension down to size," *Network*, vol. 12, pp. 141–74, May 2001.
 132. B. W. Knight, "Dynamics of encoding in a population of neurons," *J Gen Physiol*, vol. 59, pp. 734–66, Jun 1972.
 133. B. W. Knight, "The relationship between the firing rate of a single neuron and the level of activity in a population of neurons. experimental evidence for resonant enhancement in the population responses," *J Gen Physiol*, vol. 59, pp. 767–78, Jun 1972.
 134. B. W. Knight, "Dynamics of encoding in neuron populations: Some general mathematical features," *Neural Comput*, vol. 12, pp. 473–518, Mar 2000.
 135. D. Q. Nykamp and D. Tranchina, "A population density approach that facilitates large-scale modeling of neural networks: Analysis and an application to orientation tuning," *J Comput Neurosci*, vol. 8, pp. 19–50, Jan-Feb 2000.
 136. D. Q. Nykamp and D. Tranchina, "A population density approach that facilitates large-scale modeling of neural networks: Extension to slow inhibitory synapses," *Neural Comput*, vol. 13, pp. 511–46, Mar 2001.
 137. A. Omurtag, B. W. Knight, and L. Sirovich, "On the simulation of large populations of neurons," *J Comput Neurosci*, vol. 8, pp. 51–63, Jan-Feb 2000.
 138. L. Sirovich, "Dynamics of neuronal populations: Eigenfunction theory; some solvable cases," *Network*, vol. 14, pp. 249–72, May 2003.
 139. H. Risken, *The Fokker-Planck equation: Methods of solutions and applications*. Springer Series in Synergetics, Springer, 2 ed., Sep 1996.
 140. A. C. Marreiros, J. Daunizeau, S. J. Kiebel, and K. J. Friston, "Population dynamics: Variance and the sigmoid activation function," *Neuroimage*, vol. 42, pp. 147–57, Aug 2008.

141. H. R. Wilson and J. D. Cowan, "Excitatory and inhibitory interactions in localized populations of model neurons," *Biophys J*, vol. 12, pp. 1–24, Jan 1972.
142. H. R. Wilson and J. D. Cowan, "A mathematical theory of the functional dynamics of cortical and thalamic nervous tissue," *Kybernetik*, vol. 13, pp. 55–80, Sep 1973.
143. P. L. Nunez and R. Srinivasan, *Electric fields of the brain: The neurophysics of EEG*. Oxford Univ. Press, 2006.
144. K. Brodmann, *Vergleichende Lokalisationslehre der Grosshirnrinde in ihren Prinzipien dargestellt auf Grund des Zellenbaues*. Leipzig: Barth, 1909.
145. A. M. Thomson and A. P. Bannister, "Interlaminar connections in the neo-cortex," *Cereb Cortex*, vol. 13, pp. 5–14, Jan 2003.
146. L. Luo, E. M. Callaway, and K. Svoboda, "Genetic dissection of neural circuits," *Neuron*, vol. 57, pp. 634–60, Mar 2008.
147. V. Braitenberg and A. Schüz, *Anatomy of the cortex: Statistics and geometry*. Berlin, New York: Springer, 1991.
148. R. L. Beurle, "Properties of a mass of cells capable of regenerating pulses," *Phil Trans R Soc B*, vol. 240, no. 669, pp. 55–94, 1956.
149. J. S. Griffith, "A field theory of neural nets: I. derivation of field equations," *Bull Math Biophys*, vol. 25, pp. 111–20, Mar 1963.
150. J. S. Griffith, "A field theory of neural nets. ii. properties of the field equations," *Bull Math Biophys*, vol. 27, pp. 187–95, Jun 1965.
151. S. Amari, "Homogeneous nets of neuron-like elements," *Biol Cybern*, vol. 17, no. 4, pp. 211–20, 1975.
152. S. Amari, "Dynamics of pattern formation in lateral-inhibition type neural fields," *Biol Cybern*, vol. 27, pp. 77–87, Aug 1977.
153. V. K. Jirsa and H. Haken, "Field theory of electromagnetic brain activity," *Phys Rev Lett*, vol. 77, pp. 960–3, Jul 1996.
154. V. Jirsa and H. Haken, "A derivation of a macroscopic field theory of the brain from the quasi-microscopic neural dynamics," *Physica D*, vol. 99, pp. 503–26, Jan 1997.
155. F. M. Atay, "Distributed delays facilitate amplitude death of coupled oscillators," *Phys Rev Lett*, vol. 91, p. 094101, Aug 2003.
156. H. Zhao, "Global stability of neural networks with distributed delays," *Phys Rev E Stat Nonlin Soft Matter Phys*, vol. 68, p. 051909, Nov 2003.

-
157. F. M. Atay and A. Hutt, "Stability and bifurcations in neural fields with finite propagation speed and general connectivity," *SIAM J Appl Math*, vol. 65, no. 2, pp. 644–66, 2005.
 158. F. M. Atay and A. Hutt, "Neural fields with distributed transmission speeds and long-range feedback delays," *SIAM J Appl Dynam Syst*, vol. 5, no. 4, pp. 670–98, 2006.
 159. A. Hutt and F. M. Atay, "Spontaneous and evoked activity in extended neural populations with gamma-distributed spatial interactions and transmission delay," *Chaos Soliton Fract*, vol. 32, no. 2, pp. 547–60, 2007.
 160. A. Hutt and F. M. Atay, "Analysis of nonlocal neural fields for both general and gamma-distributed connectivities," *Physica D*, vol. 203, no. 1-2, pp. 30–54, 2005.
 161. J. J. Wright and D. T. J. Liley, "Dynamics of the brain at global and microscopic scales: Neural networks and the eeg," *Behav Brain Sci*, vol. 19, no. 2, pp. 285–95, 1996.
 162. P. A. Robinson, P. N. Loxley, S. C. O'Connor, and C. J. Rennie, "Modal analysis of corticothalamic dynamics, electroencephalographic spectra, and evoked potentials," *Phys Rev E Stat Nonlin Soft Matter Phys*, vol. 63, p. 041909, Mar 2001.
 163. C. J. Rennie, P. A. Robinson, and J. J. Wright, "Unified neurophysical model of eeg spectra and evoked potentials," *Biol Cybern*, vol. 86, pp. 457–71, Jun 2002.
 164. M. L. Steyn-Ross, D. A. Steyn-Ross, J. W. Sleight, and D. T. Liley, "Theoretical electroencephalogram stationary spectrum for a white-noise-driven cortex: Evidence for a general anesthetic-induced phase transitions," *Phys Rev E Stat Nonlin Soft Matter Phys*, vol. 60, pp. 7299–311, Dec 1999.
 165. I. Bojak and D. T. Liley, "Modeling the effects of anesthesia on the electroencephalogram," *Phys Rev E Stat Nonlin Soft Matter Phys*, vol. 71, p. 041902, Apr 2005.
 166. D. T. J. Liley and I. Bojak, "Understanding the transition to seizure by modeling the epileptiform activity of general anesthetic agents," *J Clin Neurophysiol*, vol. 22, pp. 300–13, Oct 2005.
 167. P. A. Robinson, C. J. Rennie, and J. J. Wright, "Propagation and stability of waves of electrical activity in the cerebral cortex," *Phys Rev E Stat Nonlin Soft Matter Phys*, vol. 56, pp. 826–40, Jul 1997.
 168. P. A. Robinson, C. J. Rennie, and D. L. Rowe, "Dynamics of large-scale brain activity in normal arousal states and epileptic seizures," *Phys Rev E Stat Nonlin Soft Matter Phys*, vol. 65, p. 041924, Apr 2002.

169. M. Breakspear, J. A. Roberts, J. R. Terry, S. Rodrigues, N. Mahant, and P. A. Robinson, "A unifying explanation of primary generalized seizures through nonlinear brain modeling and bifurcation analysis," *Cereb Cortex*, vol. 16, pp. 1296–313, Sep 2006.
170. B. Ermentrout, "Neural networks as spatio-temporal pattern-forming systems," *Rep Prog Phys*, vol. 61, no. 4, pp. 353–430, 1998.
171. O. Sporns, "The human connectome: A complex network," *Ann N Y Acad Sci*, vol. 1224, no. 1, pp. 109–25, 2011.
172. P. Hagmann, O. Sporns, N. Madan, L. Cammoun, R. Pienaar, V. J. Wedeen, R. Meuli, J.-P. Thiran, and E. Grant, "White matter maturation reshapes structural connectivity in the late developing human brain," *Proc Natl Acad Sci USA*, vol. 107, no. 44, pp. 19067–72, 2010.
173. F. Aboitiz, A. B. Scheibel, R. S. Fisher, and E. Zaidel, "Fiber composition of the human corpus callosum," *Brain Res*, vol. 598, no. 1-2, pp. 143–53, 1992.
174. J. Riise and B. Pakkenberg, "Stereological estimation of the total number of myelinated callosal fibers in human subjects," *J Anat*, vol. 218, no. 3, pp. 277–84, 2011.
175. K.-A. Nave, "Myelination and support of axonal integrity by glia," *Nature*, vol. 468, no. 7321, pp. 244–52, 2010.
176. I. A. Boyd and K. U. Kalu, "Scaling factor relating conduction velocity and diameter for myelinated afferent nerve fibres in the cat hind limb," *J Physiol*, vol. 289, no. 1, pp. 277–97, 1979.
177. J. M. Ritchie, "Physiology of axons," in *The axon: Structure, function and pathophysiology* (S. G. Waxman, J. D. Kocsis, and P. K. Stys, eds.), pp. 68–96, Oxford Univ. Press, 1995.
178. Y. Yamazaki, Y. Hozumi, K. Kaneko, S. Fujii, K. Goto, and H. Kato, "Oligodendrocytes: Facilitating axonal conduction by more than myelination," *The Neuroscientist*, vol. 16, no. 1, pp. 11–8, 2010.
179. J. DeFelipe, "From the connectome to the synaptome: An epic love story," *Science*, vol. 330, no. 6008, pp. 1198–201, 2010.
180. U. Türe, M. G. Yasargil, A. H. Friedman, and O. Al-Mefty, "Fiber dissection technique: Lateral aspect of the brain," *Neurosurgery*, vol. 47, no. 2, pp. 417–27, 2000.
181. J. Klingler, "Erleichterung der makroskopischen präparation des gehirns durch den gefrierprozeß," *Schweiz Arch Neurol Psychiatr*, vol. 36, pp. 247–56, 1935.

-
182. J. Lanciego and F. Wouterlood, "Neuroanatomical tract-tracing methods beyond 2000: What's now and next," *J Neurosci Methods*, vol. 103, no. 1, pp. 1–2, 2000.
 183. V. K. Jirsa, "Neural field dynamics with local and global connectivity and time delay," *Phil Trans R Soc A*, vol. 367, pp. 1131–43, Mar 2009.
 184. O. Faugeras, R. Veltz, and F. Grimberty, "Persistent neural states: Stationary localized activity patterns in nonlinear continuous n-population, q-dimensional neural networks," *Neural Comput*, vol. 21, pp. 147–87, Jan 2009.
 185. A. van Rotterdam, F. H. Lopes da Silva, J. van den Ende, M. A. Viergever, and A. J. Hermans, "A model of the spatial-temporal characteristics of the alpha rhythm," *Bull Math Biol*, vol. 44, no. 2, pp. 283–305, 1982.
 186. C. J. Stam, J. P. Pijn, P. Suffczynski, and F. H. Lopes da Silva, "Dynamics of the human alpha rhythm: Evidence for non-linearity?," *Clin Neurophysiol*, vol. 110, pp. 1801–13, Oct 1999.
 187. P. A. Valdes, J. C. Jimenez, J. Riera, R. Biscay, and T. Ozaki, "Nonlinear eeg analysis based on a neural mass model," *Biol Cybern*, vol. 81, pp. 415–24, Nov 1999.
 188. P. Suffczynski, S. Kalitzin, G. Pfurtscheller, and F. H. Lopes da Silva, "Computational model of thalamo-cortical networks: Dynamical control of alpha rhythms in relation to focal attention," *Int J Psychophysiol*, vol. 43, pp. 25–40, Dec 2001.
 189. F. Grimberty and O. Faugeras, "Bifurcation analysis of jansen's neural mass model," *Neural Comput*, vol. 18, no. 12, pp. 3052–68, 2006.
 190. M. Zavaglia, L. Astolfi, F. Babiloni, and M. Ursino, "A neural mass model for the simulation of cortical activity estimated from high resolution eeg during cognitive or motor tasks," *J Neurosci Methods*, vol. 157, pp. 317–29, Oct 2006.
 191. A. Grabska-Barwinska and J. Zygiereicz, "A model of event-related eeg synchronization changes in beta and gamma frequency bands," *J Theor Biol*, vol. 238, pp. 901–13, Feb 2006.
 192. J. W. Kim and P. A. Robinson, "Compact dynamical model of brain activity," *Phys Rev E Stat Nonlin Soft Matter Phys*, vol. 75, p. 031907, Mar 2007.
 193. M. Ursino, M. Zavaglia, L. Astolfi, and F. Babiloni, "Use of a neural mass model for the analysis of effective connectivity among cortical regions based on high resolution eeg recordings," *Biol Cybern*, vol. 96, pp. 351–65, Mar 2007.

194. C. Zhou, L. Zemanová, G. Zamora-López, C. C. Hilgetag, and J. Kurths, "Structure-function relationship in complex brain networks expressed by hierarchical synchronization," *New J Phys*, vol. 9, no. 6, p. 178, 2007.
195. R. C. Sotero and N. J. Trujillo-Barreto, "Biophysical model for integrating neuronal activity, eeg, fmri and metabolism," *Neuroimage*, vol. 39, pp. 290–309, Jan 2008.
196. M. Zavaglia, L. Astolfi, F. Babiloni, and M. Ursino, "The effect of connectivity on eeg rhythms, power spectral density and coherence among coupled neural populations: Analysis with a neural mass models," *IEEE T Bio-Med Eng*, vol. 55, pp. 69–77, Jan 2008.
197. R. J. Moran, S. J. Kiebel, K. E. Stephan, R. B. Reilly, J. Daunizeau, and K. J. Friston, "A neural mass model of spectral responses in electrophysiology," *Neuroimage*, vol. 37, pp. 706–20, Sep 2007.
198. O. David, D. Cosmelli, and K. J. Friston, "Evaluation of different measures of functional connectivity using a neural mass model," *Neuroimage*, vol. 21, pp. 659–73, Feb 2004.
199. K. J. Friston, A. J. T., S. J. Kiebel, T. E. Nichols, and W. D. Penny, *Statistical parametric mapping: The analysis of functional brain images*. Amsterdam, Boston: Academic Press, 1 ed., 2007.
200. H. Wu and P. A. Robinson, "Modeling and investigation of neural activity in the thalamus," *J Theor Biol*, vol. 244, pp. 1–14, Jan 2007.
201. W. Rall, "Electrophysiology of a dendritic neuron model," *Biophys J*, vol. 2, pp. 145–67, Mar 1962.
202. W. Rall, "Distinguishing theoretical synaptic potentials computed for different soma-dendritic distributions of synaptic inputs," *J Neurophysiol*, vol. 30, pp. 1138–68, Sep 1967.
203. W. Rall, "A statistical theory of monosynaptic input-output relations," *J Cell Comp Physiol*, vol. 46, pp. 373–411, Dec 1955.
204. W. Rall, "Experimental monosynaptic input-output relations in the mammalian spinal cord," *J Cell Comp Physiol*, vol. 46, pp. 413–37, Dec 1955.
205. W. Freeman, "Nonlinear gain mediating cortical stimulus-response relations," *Biol Cybern*, vol. 33, pp. 237–47, Aug 1979.
206. H. Agmon-Snir and I. Segev, "Signal delay and input synchronization in passive dendritic structures," *J Neurophysiol*, vol. 70, pp. 2066–85, Nov 1993.
207. A. T. Gullledge, B. M. Kampa, and G. J. Stuart, "Synaptic integration in dendritic trees," *J Neurobiol*, vol. 64, pp. 75–90, Jul 2005.

-
208. J. J. B. Jack, D. Noble, and R. Tsien, *Electric current flow in excitable cells*. Oxford: Clarendon Press, 1975.
209. N. Spruston, "Pyramidal neurons: Dendritic structure and synaptic integration," *Nat Rev Neurosci*, vol. 9, pp. 206–21, Mar 2008.
210. S. S. Goldstein and W. Rall, "Changes of action potential shape and velocity for changing core conductor geometry," *Biophys J*, vol. 14, pp. 731–57, Oct 1974.
211. C. J. Rennie, P. A. Robinson, and J. J. Wright, "Effects of local feedback on dispersion of electrical waves in the cerebral cortex," *Phys Rev E Stat Nonlin Soft Matter Phys*, vol. 59, pp. 3320–9, Mar 1999.
212. C. J. Rennie, J. J. Wright, Peter, and A. Robinson, "Mechanisms of cortical electrical activity and emergence of gamma rhythms," *J Theor Biol*, vol. 205, pp. 17–35, 2000.
213. J. J. Wright, P. A. Robinson, C. J. Rennie, E. Gordon, P. D. Bourke, C. L. Chapman, N. Hawthorn, G. J. Lees, and D. Alexander, "Toward an integrated continuum model of cerebral dynamics: The cerebral rhythms, synchronous oscillation and cortical stability," *Biosystems*, vol. 63, no. 1–3, pp. 71–88, 2001.
214. J. J. Wright, C. J. Rennie, G. J. Lees, P. A. Robinson, P. D. Bourke, C. L. Chapman, E. Gordon, and D. L. Rowe, "Simulated electrocortical activity at microscopic, mesoscopic, and global scales," *Neuropsychopharmacol*, vol. 28, pp. S80–93, Jul 2003.
215. P. A. Robinson, C. J. Rennie, R. D. L., S. C. O'Connor, J. J. Wright, and W. R. W. Gordon, E., "Neurophysical modeling of brain dynamics," *Neuropsychopharmacol*, vol. 28, pp. S74–9, 2003.
216. P. A. Robinson, C. J. Rennie, J. J. Wright, H. Bahramali, E. Gordon, and D. L. Rowe, "Prediction of electroencephalographic spectra from neurophysiology," *Phys Rev E Stat Nonlin Soft Matter Phys*, vol. 63, p. 021903, Jan 2001.
217. D. T. Liley, P. J. Cadusch, and J. J. Wright, "A continuum theory of electrocortical activity," *Neurocomputing*, vol. 26–27, pp. 795–800, 1999.
218. D. S. Bredt and R. A. Nicoll, "Ampa receptor trafficking at excitatory synapses," *Neuron*, vol. 40, pp. 361–79, Oct 2003.
219. L. H. Zetterberg, "Stochastic activity in a population of neurons—a system analysis approach," Tech. Rep. 1, Institute of Medical Physics TNO, Utrecht, 1973.
220. W. Freeman, *Neurodynamics: An exploration in mesoscopic brain dynamics*. Perspectives in Neural Computing, Springer, 1 ed., Mar 2000.

221. <http://www.mathworks.com/products/matlab/>.
222. Y. A. Kuznetsov, *Elements of applied bifurcation theory*. Applied Mathematical Sciences, Berlin: Springer, 2 ed., 1998.
223. J. Nelder and R. Mead, "A simplex method for function minimization," *Comp J*, vol. 7, no. 4, pp. 308–13, 1965.
224. A. Dhooge, W. Govaerts, and Y. A. Kuznetsov, "Matcont: A matlab package for numerical bifurcation analysis of odes," *ACM T Math Software*, vol. 29, pp. 141–64, Jun 2003.
225. <http://www.matcont.UGent.be/>.
226. <http://sourceforge.net/projects/matcont/>.
227. T. E. Hull, W. H. Enright, and K. R. Jackson, "User's guide for dverk—a subroutine for solving non-stiff ode's," Tech. Rep. 100, Department of Computer Sciences, Univ. of Toronto, 1976.
228. S. H. Strogatz, *Nonlinear dynamics and chaos: With applications to physics, biology, chemistry, and engineering*. Studies in nonlinearity, Westview Press, 1 ed., Jan 1994.
229. Z.-M. Chen, K. Djidjeli, and W. Price, "Computing lyapunov exponents based on the solution expression of the variational system," *Appl Math Comput*, vol. 174, no. 2, pp. 982–96, 2006.
230. A. Wolf, J. B. Swift, H. L. Swinney, and J. A. Vastano, "Determining lyapunov exponents from a time series," *Physica D*, vol. 16, no. 3, pp. 285–317, 1985.
231. H. Kantz and T. Schreiber, *Nonlinear time series analysis*. Cambridge Univ. Press, 2004.
232. M. Watanabe, K. Maemura, K. Kanbara, T. Tamayama, and H. Hayasaki, "Gaba and gaba receptors in the central nervous system and other organs," in *A Survey of Cell Biology* (K. W. Jeon, ed.), vol. 213 of *International Review of Cytology*, pp. 1–47, Academic Press, 2002.
233. K. Letinic, R. Zoncu, and P. Rakic, "Origin of gabaergic neurons in the human neocortex," *Nature*, vol. 417, no. 6889, pp. 645–9, 2002.
234. D. M. Treiman, "Gabaergic mechanisms in epilepsy," *Epilepsia*, vol. 42, pp. 8–12, 2001.
235. B. P. Blum and J. J. Mann, "The gabaergic system in schizophrenia," *Int J Neuropsychopharmacol*, vol. 5, no. 2, pp. 159–79, 2002.
236. M. M. Kohl and O. Paulsen, "The roles of gabab receptors in cortical network activity," in *GABABReceptor pharmacology—A tribute to Norman Bowery*

- (T. P. Blackburn, ed.), vol. 58 of *Advances in Pharmacology*, pp. 205–29, Academic Press, 2010.
237. K. Zilles, N. Palomero-Gallagher, and A. Schleicher, “Transmitter receptors and functional anatomy of the cerebral cortex,” *J Anat*, vol. 205, no. 6, pp. 417–32, 2004.
238. J. A. White, M. I. Banks, R. A. Pearce, and N. J. Kopell, “Networks of interneurons with fast and slow γ -aminobutyric acid type a (gaba_a) kinetics provide substrate for mixed gamma-theta rhythm,” *Proc Natl Acad Sci USA*, vol. 97, no. 14, pp. 8128–33, 2000.
239. M. Breakspear and V. K. Jirsa, “Neuronal dynamics and brain connectivity,” in *Handbook of brain connectivity* (V. K. Jirsa and A. R. McIntosh, eds.), pp. 3–64, Berlin, Heidelberg: Springer, 2007.
240. B. Ahmed, J. C. Anderson, K. A. Martin, and J. C. Nelson, “Map of the synapses onto layer 4 basket cells of the primary visual cortex of the cat,” *J Comp Neurol*, vol. 380, pp. 230–42, Apr 1997.
241. J. F. Staiger, I. Flaggmeyer, D. Schubert, K. Zilles, R. Kotter, and H. J. Luhmann, “Functional diversity of layer iv spiny neurons in rat somatosensory cortex: Quantitative morphology of electrophysiologically characterized and biocytin labeled cells,” *Cereb Cortex*, vol. 14, pp. 690–701, Jun 2004.
242. K. J. Stratford, K. Tarczy-Hornoch, K. A. Martin, N. J. Bannister, and J. J. Jack, “Excitatory synaptic inputs to spiny stellate cells in cat visual cortex,” *Nature*, vol. 382, pp. 258–61, Jul 1996.
243. D. J. Felleman and D. C. Van Essen, “Distributed hierarchical processing in the primate cerebral cortex,” *Cereb Cortex*, vol. 1, no. 1, pp. 1–47, 1991.
244. S. R. Williams and G. J. Stuart, “Role of dendritic synapse location in the control of action potential output,” *Trends Cogn Sci*, vol. 26, pp. 147–54, Mar 2003.
245. L. Perko, *Differential equations and dynamical systems*. Texts in applied mathematics, New York: Springer, 3 ed., 2001.
246. P. Glendinning and C. Sparrow, “Shilnikov’s saddle-node bifurcation,” *IJBC*, vol. 6, pp. 1153–60, Jun 1996.
247. D. Attwell and S. B. Laughlin, “An energy budget for signaling in the grey matter of the brain,” *JCBFM*, vol. 21, pp. 1133–45, Oct 2001.
248. M. P. Nawrot, C. Boucsein, V. Rodriguez-Molina, A. Aertsen, S. Grun, and S. Rotter, “Serial interval statistics of spontaneous activity in cortical neurons in vivo and in vitro,” *Neurocomputing*, vol. 70, pp. 1717–22, Jun 2007.

249. K. Shenoy, M. Churchland, G. Santhanam, B. Yu, and S. Ryu, "Influence of movement speed on plan activity in monkey pre-motor cortex and implications for high-performance neural prosthetic system design," in *IEEE EMBS 25th Annual Meeting*, (Cancun), pp. 1897–1900, 2003.
250. L. Gabernet, S. P. Jadhav, D. E. Feldman, M. Carandini, and M. Scanziani, "Somatosensory integration controlled by dynamic thalamocortical feed-forward inhibition," *Neuron*, vol. 48, pp. 315–27, Oct 2005.
251. F. Kimura, C. Itami, K. Ikezoe, H. Tamura, I. Fujita, Y. Yanagawa, K. Obata, and M. Ohshima, "Fast activation of feedforward inhibitory neurons from thalamic input and its relevance to the regulation of spike sequences in the barrel cortex," *J Physiol*, vol. 588, pp. 2769–87, 2010.
252. M. Wehr and A. M. Zador, "Balanced inhibition underlies tuning and sharpens spike timing in auditory cortex," *Nature*, vol. 426, pp. 442–6, Nov 2003.
253. N. J. Priebe and D. Ferster, "Inhibition, spike threshold, and stimulus selectivity in primary visual cortex," *Neuron*, vol. 57, pp. 482–97, Feb 2008.
254. R. K. Otnes and L. Enochson, *Digital time series analysis*. New York: Wiley, 1972.
255. G. V. Osipov, J. Kurths, and C. Zhou, *Synchronization in oscillatory networks*. Springer, 2007.
256. A. Pikovsky, M. Rosenblum, and J. Kurths, *Synchronization: A universal concept in nonlinear sciences*. Nonlinear Science Series, Cambridge Univ. Press, 1 ed., May 2003.
257. R. D. Beer, "On the dynamics of small continuous-time recurrent neural networks," *Adapt Behav*, vol. 3, pp. 469–509, Mar 1995.
258. L. van Veen and D. T. Liley, "Chaos via shilnikov's saddle-node bifurcation in a theory of the electroencephalograms," *Phys Rev Lett*, vol. 97, p. 208101, Nov 2006.
259. E. M. Izhikevich, "Simple model of spiking neurons," *IEEE T Neural Networ*, vol. 14, pp. 1569–72, Nov 2003.
260. S. Haeusler and W. Maass, "A statistical analysis of information-processing properties of lamina-specific cortical microcircuit models," *Cereb Cortex*, vol. 17, no. 1, pp. 149–62, 2007.
261. R. Friedrich and C. Uhl, "Spatio-temporal analysis of human electroencephalograms: Petit-mal epilepsy," *Physica D*, vol. 98, pp. 171–82, Nov 1996.
262. G. Pfurtscheller and F. H. Lopes da Silva, "Event-related eeg/meg synchronization and desynchronization: basic principles," *Clin Neurophysiol*, vol. 110, pp. 1842–57, Nov 1999.

-
263. W. Klimesch, "Eeg alpha and theta oscillations reflect cognitive and memory performance: A review and analysis," *Brain Research Reviews*, vol. 29, pp. 169–95, 1999.
264. G. Pfurtscheller, "Functional topography during sensorymotor activation studied with event-related desynchronization mapping," *J Clin Neurophysiol*, vol. 6, pp. 75–84, 1989.
265. R. Salmelin, N. Forss, J. Knuutila, and R. Hari, "Bilateral activation of the human somatomotor cortex by distal hand movements," *Electroencephalogr Clin Neurophysiol*, vol. 95, pp. 444–52, 1995.
266. R. Salmelin and R. Hari, "Spatiotemporal characteristics of sensorimotor neuromagnetic rhythms related to thumb movements," *Neurosci Lett*, vol. 60, pp. 537–50, 1994.
267. R. Hari and R. Salmelin, "Human cortical oscillations: A neuromagnetic view through the skull," *Trends Neurosci*, vol. 20, pp. 44–9, 1997.
268. A. Spiegler, B. Graimann, and G. Pfurtscheller, "Phase coupling between different motor areas during tongue-movement imagery," *Neurosci Lett*, vol. 369, pp. 50–4, Oct 2004.
269. A. Burgess and L. Ali, "Functional connectivity of gamma eeg activity is modulated at low frequency during conscious recollection," *Int J Psychophysiol*, vol. 46, pp. 91–100, 2002.
270. A. Burgess and J. Gruzelier, "Short duration synchronization of human theta rhythm during recognition memory," *Neuroreport*, vol. 8, pp. 1039–42, 1997.
271. C. Herrmann, M. Munk, and A. Engel, "Cognitive functions of gamma-band activity: Memory match and utilization," *Trends Cogn Sci*, vol. 8, pp. 347–55, 2004.
272. M. Kahana, R. Sekuler, J. Caplan, M. Kirschen, and J. Madsen, "Human theta oscillations exhibit task dependence during virtual maze navigation," *Nature*, vol. 399, pp. 781–4, 1999.
273. W. Klimesch, M. Doppelmayr, H. Russegger, and T. Pachinger, "Theta band power in the human scalp eeg and the encoding of new information," *Neuroreport*, vol. 7, pp. 1235–40, 1996.
274. W. Klimesch, M. Doppelmayr, H. Schimke, and B. Ripper, "Theta synchronization in a memory task," *Psychophysiology*, vol. 34, pp. 169–76, 1997.
275. J. Lisman and M. Idiart, "Storage of 7+/-2 short-term memories in oscillatory subcycles," *Science*, vol. 267, pp. 1512–5, 1995.

276. R. Llinás and U. Ribary, "Coherent 40-hz oscillation characterizes dream state in human," *Proc Natl Acad Sci USA*, vol. 90, pp. 2078–81, 1993.
277. C. Gray and W. Singer, "Stimulus-specific neuronal oscillations in orientation columns of cat visual cortex.," *Proc Natl Acad Sci USA*, vol. 86, pp. 1698–702, 1989.
278. C. Herrmann and A. Mecklinger, "Magnetoencephalographic responses to illusory figures: Early evoked gamma is affected by processing of stimulus features," *Int J Psychophysiol*, vol. 38, pp. 265–81, 2000.
279. C. Tallon-Baudry, O. Bertrand, C. Delpuech, and J. Pernier, "Oscillatory gamma-band (30–70 Hz) activity induced by a visual search task in humans," *J Neurosci*, vol. 17, pp. 722–34, 1997.
280. C. Tallon-Baudry, O. Bertrand, C. Delpuech, and J. Pernier, "Stimulus specificity of phase-locked and non-phase-locked 40 Hz visual responses in humans," *J Neurosci*, vol. 16, pp. 4240–9, 1996.
281. A. Knief, M. Schulte, O. Bertran, and C. Pantev, "The perception of coherent and non-coherent auditory objects: A signature in gamma frequency bands," *Hear Res*, vol. 145, pp. 161–8, 2000.
282. C. Pantev, T. Elbert, S. Makeig, S. Hampson, C. Eulitz, and M. Hoke, "Relationship of transient and steady-state auditory evoked fields," *Electroencephalogr Clin Neurophysiol*, vol. 88, pp. 389–96, 1993.
283. C. Pantev, S. Makeig, M. Hoke, R. Galambos, S. Hampson, and C. Gallen, "Human auditory evoked gamma-band magnetic fields," *Proc Natl Acad Sci USA*, vol. 88, pp. 8996–9000, 1991.
284. A. Destexhe and T. Sejnowski, *Thalamocortical assemblies: How ion channels, single neurons and large-scale networks organize sleep oscillations*. Oxford: Oxford Univ. Press, 1 ed., Dec 2001.
285. J. Gross, J. Kujala, M. Hamalainen, L. Timmermann, A. Schnitzler, and R. Salmelin, "Dynamic imaging of coherent sources: Studying neural interactions in the human brain," *Proc Natl Acad Sci USA*, vol. 98, pp. 694–9, Jan 2001.
286. A. Schnitzler and J. Gross, "Normal and pathological oscillatory communication in the brain," *Nat Rev Neurosci*, vol. 6, pp. 285–96, Apr 2005.
287. P. Tass, M. G. Rosenblum, J. Weule, J. Kurths, A. Pikovsky, J. Volkmann, A. Schnitzler, and H.-J. Freund, "Detection of n:m phase locking from noisy data: Application to magnetoencephalography," *Phys Rev Lett*, vol. 81, pp. 3291–4, Oct 1998.

-
288. M. E. Hasselmo, "Neuromodulation and cortical function: Modeling the physiological basis of behavior," *Behav Brain Res*, vol. 67, pp. 1–27, Feb 1995.
289. J. Buchli, L. Righetti, and A. Ijspeert, "Engineering entrainment and adaptation in limit cycle systems," *Biol Cybern*, vol. 95, pp. 645–64, 2006.
290. M. P. Dafilis, F. Frascoli, P. J. Cadusch, and D. T. Liley, "Chaos and generalised multistability in a mesoscopic model of the electroencephalogram," *Physica D*, vol. 238, no. 13, pp. 1056–60, 2009.
291. M. P. Dafilis, D. T. J. Liley, and P. J. Cadusch, "Robust chaos in a model of the electroencephalogram: Implications for brain dynamics," *Chaos*, vol. 11, no. 3, pp. 474–8, 2001.
292. W. J. Freeman, "Evidence from human scalp electroencephalograms of global chaotic itinerancy," *Chaos*, vol. 13, no. 3, pp. 1067–77, 2003.
293. H. Korn and P. Faure, "Is there chaos in the brain? ii. experimental evidence and related models," *C R Biol*, vol. 326, no. 9, pp. 787–840, 2003.
294. S. Makeig, "Auditory event-related dynamics of the eeg spectrum and effects of exposure to tones," *Electroencephalogr Clin Neurophysiol*, vol. 86, no. 4, pp. 283–93, 1993.
295. K. J. Miller, E. C. Leuthardt, G. Schalk, R. P. N. Rao, N. R. Anderson, D. W. Moran, J. W. Miller, and J. G. Ojemann, "Spectral changes in cortical surface potentials during motor movements," *J Neurosci*, vol. 27, no. 9, pp. 2424–32, 2007.
296. Y. Zhang, X. Wang, S. L. Bressler, Y. Chen, and M. Ding, "Prestimulus cortical activity is correlated with speed of visuomotor processing," *J Cogn Neurosci*, vol. 20, no. 10, pp. 1915–25, 2008.
297. S. M. Doesburg, K. Kitajo, and L. M. Ward, "Increased gamma-band synchrony precedes switching of conscious perceptual objects in binocular rivalry," *Neuroreport*, vol. 16, no. 11, pp. 1139–42, 2005.
298. A. Babloyantz, J. Salazar, and C. Nicolis, "Evidence of chaotic dynamics of brain activity during the sleep cycle," *Phys Lett A*, vol. 111, no. 3, pp. 152–6, 1985.
299. D. Gallez and A. Babloyantz, "Predictability of human eeg: A dynamical approach," *Biol Cybern*, vol. 64, pp. 381–91, 1991.
300. G. V. Di Prisco and W. J. Freeman, "Odor-related bulbar eeg spatial pattern analysis during appetitive conditioning in rabbits," *Behav Neurosci*, vol. 99, pp. 964–78, Oct 1985.

301. W. J. Freeman and G. V. Di Prisco, "Spatial patterns differences with discriminated odors manifest chaotic and limit cycles attractors in olfactory bulb of rabbits," in *Brain theory* (G. Palm and A. Aartsen, eds.), pp. 97–119, Springer, 1986.
302. A. Babloyantz and A. Destexhe, "Low-dimensional chaos in an instance of epilepsy," *Proc Natl Acad Sci USA*, vol. 83, pp. 3513–17, May 1986.
303. L. D. Iasemidis and J. C. Sackellares, "The evolution with time of the spatial distribution of the largest lyapunov exponent on the human epileptic cortex," in *Measuring chaos in the human brain* (D. Duke and W. Pritchard, eds.), pp. 49–82, World Scientific, 1991.
304. L. D. Iasemidis, J. Chris Sackellares, H. P. Zaveri, and W. J. Williams, "Phase space topography and the lyapunov exponent of electrocorticograms in partial seizures," *Brain Topogr*, vol. 2, pp. 187–201, 1990.
305. K. Lehnertz and C. E. Elger, "Can epileptic seizures be predicted? evidence from nonlinear time series analysis of brain electrical activity," *Phys Rev Lett*, vol. 80, pp. 5019–22, Jun 1998.
306. M. I. Rabinovich, R. Huerta, and G. Laurent, "Transient dynamics for neural processing," *Science*, vol. 321, pp. 48–50, Jul 2008.
307. M. I. Rabinovich, R. Huerta, P. Varona, and V. S. Afraimovich, "Transient cognitive dynamics, metastability, and decision making," *PLoS Comput Biol*, vol. 4, p. e1000072, May 2008.
308. A. K. Engel and W. Singer, "Temporal binding and the neural correlates of sensory awareness," *Trends Cogn Sci*, vol. 5, pp. 16–25, Jan 2001.
309. P. Fries, "A mechanism for cognitive dynamics: neuronal communication through neuronal coherence," *Trends Cogn Sci*, vol. 9, pp. 474–80, Oct 2005.
310. C. Tallon-Baudry, "Attention and awareness in synchrony," *Trends Cogn Sci*, vol. 8, pp. 523–5, 2004.
311. T. Rosburg, P. Trautner, O. A. Korzyukov, N. N. Boutros, C. Schaller, C. E. Elger, and M. Kurthen, "Short-term habituation of the intracranially recorded auditory evoked potentials p50 and n100," *Neurosci Lett*, vol. 372, no. 3, pp. 245–9, 2004.
312. T. Rosburg, P. Trautner, N. N. Boutros, O. A. Korzyukov, C. Schaller, C. E. Elger, and M. Kurthen, "Habituation of auditory evoked potentials in intracranial and extracranial recordings," *Psychophysiology*, vol. 43, no. 2, pp. 137–44, 2006.

- 313. K. J. Friston, A. Mechelli, R. Turner, and C. J. Price, “Nonlinear responses in fmri: The balloon model, volterra kernels, and other hemodynamics,” *Neuroimage*, vol. 12, no. 4, pp. 466–77, 2000.
- 314. S. Grossberg, “The link between brain learning, attention, and consciousness,” *Conscious Cogn*, vol. 8, no. 1, pp. 1–44, 1999.
- 315. D. C. V. Essen, “Corticocortical and thalamocortical information flow in the primate visual system,” in *Cortical function: A view from the thalamus* (R. G. V.A. Casagrande and S. Sherman, eds.), vol. 149 of *Prog Brain Res*, pp. 173–85, Elsevier, 2005.
- 316. D. O. Hebb, *The organization of behavior: A neuropsychological theory*. New York: Wiley, 1949.
- 317. L. F. Abbott and S. B. Nelson, “Synaptic plasticity: taming the beast,” *Nat Neurosci*, vol. 3, pp. 1178–83, Nov 2000.

List of Figures

3.1	The NM and its interconnections.	45
3.2	Photic driving experiment.	69
4.1	The Zetterberg-Jansen circuit and its modifications.	73
5.1	Bifurcation diagram of Jansen's configuration.	88
5.2	Phase portraits of system regimes.	90
5.3	Classification of LC-branches.	91
5.4	Branch types in the plane of the dendritic time constants.	95
5.5	(a) Type I-A to C and II-AA to BC against extrinsic inputs.	98
5.5	(b) Type II-CC and type II combinations against extrinsic inputs.	99
5.6	LC-mechanisms against dendritic time constants.	100
5.7	LC-mechanisms against extrinsic inputs	102
5.8	Frequency charts of LC-branches.	104
5.9	Encapsulated LC within another one.	105
5.10	Overlapping branches of LCs.	107
5.11	Sequence of stable LC-branches.	109
5.12	Ordered sequence by a trajectory of extrinsic inputs.	110
5.13	Frequency entrainment effects.	115
5.14	Examples of complex behavior.	116
5.15	Largest Lyapunov exponent in the parameter space.	118
5.16	Occurrence of quasi-periodic-behavior forming a two-torus surface.	119
5.17	Kaplan-Yorke dimension in the parameter space.	120
5.18	Bifurcation diagram for stimulus amplitude $\zeta = 3.6301$	122
6.1	Comparison of model and data from the photic driving experiment.	125
A.1	Bifurcation diagram of a single NM with auto-feedback.	159

List of Tables

3.1	Activity-based models.	51
3.2	Voltage-based models.	55
3.3	Jansen and Rit parameters.	62
4.1	Effective extrinsic input ranges.	77
5.1	Range of the varied system parameters.	81
5.2	Dynamic regimes for stimulus amplitude $\zeta = 3.6301$	121
6.1	Single subject comparison.	127
A.1	Abbreviations	161
A.2	Variables	162
A.3	Parameters	162
A.4	Operators	163
A.5	Subscripts	163